

Chapter 1

Introduction

If the Theory of making Telescopes could at length be fully brought into Practice, yet there would be certain Bounds beyond which Telescopes could not perform. For the Air through which we look upon the Stars, is in perpetual Tremor; as may be seen... by the twinkling of the fix'd Stars... Long Telescopes may cause an Object to appear brighter than short ones can do, but they cannot be so formed as to take away the confusion of the Rays which arises from the Tremors of the Atmosphere. The only Remedy is a most serene and quiet Air, such as may perhaps be found on the tops of the highest Mountains above the grosser clouds.

Isaac Newton, Opticks 1604.

All Earth-bound astronomy is subject to the limitations of atmospheric “seeing”, in which the Earth’s turbulent atmosphere refracts light from space, producing randomly fluctuating distortions in the images that we see. To the eye this seeing is manifest in the twinkling of stars and shimmering of the Moon, Sun and planets. In modern times we record images for analysis and publication, but because of seeing the camera records a blurred and distorted image regardless of the quality of the optical system.

Over the past few decades new techniques have emerged that allow the effects of seeing to be at least partly overcome. The problem and these solutions are outlined in chapter 2. These include high altitude and outer space observing sites, speckle

techniques and adaptive optics. Each of these methods is effective in the imaging regime for which it is designed, but each incurs great cost and complexity in computing, equipment or logistics.

This study investigated an innovative imaging process called “selective imaging”, also commonly called “lucky imaging”, that requires much simpler hardware and software than other methods. In its essence selective imaging involves the acquisition of hundreds to thousands of consecutive short exposure images of an object, the analysis of every frame for sharpness, and the selection of only those frames meeting some quality criteria for combination into a final image. The sharpest frames are those taken during the random moments of minimal atmospheric turbulence, the “serene and quiet Air” to which Newton referred. The technique is particularly suited to routine imaging of bright objects using small to moderate sized telescopes, to which astronomers have regular access. However, selective imaging can be expanded and adapted to many other imaging applications. Selective imaging is conceptually similar to speckle imaging, but it is computationally simpler because no prior knowledge of the object is required.

A number of studies and demonstrations of selective imaging have been conducted with remarkable results (see chapter 3). These have, however, all concentrated on particular applications, observing sites or instruments, and so have not explored the full range of selective imaging parameters. This study has covered a much wider range of parameter space including seeing, telescope aperture, colour band, frame exposure time and frame selection ratio. To do this we made use of an inexpensive monochrome video camera, which we dubbed the Macquarie University Selective Imaging Camera or *MUSIC*. This camera had a wide range of frame exposure times and adjustable gain. We observed with it on different telescopes at different sites. On each telescope we used various aperture masks and colour filters. The aims and hardware setup for the *MUSIC* study are discussed in chapter 4. We have also investigated the effect of the “shift and add” processing on sharpness across the field of view.

To assess the performance of selective imaging at negating the effects of atmospheric turbulence it is necessary to compare the results of frame selection with a known ideal image. Hence we extensively imaged a number of bright stars, binaries and clusters,

because for stars the ideal image pattern, or point spread function, is known. The choice of bright stars meant that the simplest possible quality measure, the brightest pixel value in an image, could be used in order to minimise the computational complexity. Frames were then co-aligned so that the peak pixel in each frame was coincident with that in the best frame. The quality of the resulting stellar images was measured using the Strehl ratio, because it compares the real image with the ideal one. The image processing software system is explained in chapter 5.

The general analysis of the frame selection technique with a simple camera and image metric was done to pave the way for a more comprehensive system. This will consist of a low noise electron multiplying CCD (EMCCD) camera, and be used primarily for planetary imaging at the University of New South Wales. We therefore also made experimental observations of lunar features and solar system planets. For the main analysis of planetary images we chose a metric that uses autocorrelation to measure frame sharpness. Shift-and-adding of the good frames was done by cross-correlation with the best frame. For comparison, some observations were also processed using a contrast operator to measure sharpness. These two metrics are suitable for extended objects rather than for point sources.

The results of the frame selection process are analysed for the stellar and planetary images in chapters 6 and 7 respectively.

I have conducted this research on a part-time basis for the Masters of Science degree in the Department of Physics and Astronomy at Macquarie University. The project is co-supervised by Dr Jeremy Bailey of the University of New South Wales, and by Dr's Mark Wardle and Alan Vaughan at Macquarie University.

Chapter 2

The Problem: “Seeing”

*Big whorls have little whorls,
That feed on their velocity;
And little whorls have lesser whorls,
And so on to viscosity.*

L. F. Richardson (1920)

2.1 Introduction

This chapter describes the problem of astronomical seeing that the frame selection method aims to remedy. First I will outline the effects of atmospheric turbulence and telescope diffraction on imaging, and define diffraction-limited and seeing-limited resolution. The effects on resolution of imaging parameters such as aperture and exposure time will be explained. Finally the methods of overcoming seeing are described. Although these methods are tremendously useful, their limitations will be highlighted, so that the usefulness of the frame selection method can be shown in chapter 3.

2.2 Description of Seeing

In order to learn about an astronomical object, and to share the new knowledge, it is necessary to record information that is acquired using some optical system. I will be

dealing with information in the form of images, but much of the discussion can also apply to spectroscopy.

When recording an image the goal is usually to maximise its resolution; that is, to be able to see the finest detail possible. The resolution of a telescope is usually defined by the Rayleigh criterion, which is the smallest angular separation between two point sources, such as stars, at which they can be resolved as separate (Smith 1995). This is limited firstly by the diffraction of light as it propagates through the telescope, which spreads the light away from the point in the image. The pattern of this spread is called the point spread function, or PSF. The image of a diffraction limited PSF has the appearance of a bright central spot called the Airy disc surrounded by narrow, successively fainter rings (see figure 2.1). The Rayleigh separation is the distance between two Airy discs where the peak of one is placed at the first minimum of the second. This is the same as the width of the PSF. Hence the formula for diffraction limited angular resolution for a circular aperture is given by the radius of the first zero of the first order Bessel function

$$\theta = \frac{1.22\lambda}{D} \text{ radians,} \quad (2.1)$$

where D is the telescope aperture and λ is the wavelength of light.

The second limitation on angular resolution is the effect of the atmosphere on the light propagating through it before it reaches the telescope. Wavefronts of light coming from astronomical distances are assumed to be planar when they reach our atmosphere. For purposes of wave propagation the atmosphere may be modeled as an array of turbulence cells, each with its own approximately constant refractive index, being swept along by local winds. As the waves pass through these moving cells they are perturbed in a random and fluctuating fashion. Wavefronts reaching a telescope will therefore be non-planar (anisoplanatic). The result is that an image will be distorted by variations in the phase of the wavefront across the field. When an image is recorded, these changing phase variations are integrated over the exposure time and produce a blurred and distorted picture.

Kolmogorov (1941a;b) (papers are contained in Tikhomirov (1985)) developed the first statistical analysis of atmospheric turbulence that has been widely used since. He modelled the way large or outer scale motions of size L_0 , such as weather fronts, break down into successively smaller turbulent eddies. This continues down through successively smaller scales until viscosity prevents the further breakdown of turbulence and any remaining energy is dissipated as heat (Roggemann and Welsh 1996). This smallest scale of turbulence has size l_0 of the order of a few millimetres. This phenomenon was poetically summarized by Richardson in the above quotation. Kolmogorov's statistical description provided a power spectrum for velocity fluctuations. Tatarski (1961) and Corrsin (1951) examined Kolmogorov's model in terms of wave propagation through turbulent media. The refractive index of the atmosphere can be modeled as the sum of the mean refractive index n_0 and a randomly fluctuating component $n_1(\mathbf{r}, t)$:

$$n(\mathbf{r}, t) = n_0 + n_1(\mathbf{r}, t), \quad (2.2)$$

where \mathbf{r} is a position vector, and t is time. The statistical distribution of the number and size of the turbulent eddies is expressed by the power spectral density (PSD) of $n_1(\mathbf{r})$. Assuming a Gaussian distribution for $n_1(\mathbf{r})$, the PSD, represented by Φ_n , is found by taking the Fourier transform of the covariance of $n_1(\mathbf{r})$. It is a function of the spatial wave vector \mathbf{k} which is related to the turbulence scale size l . For homogeneous and isotropic turbulence the PSD of refractive index fluctuations is a function of the scalar wavenumber $k = 2\pi/l$. For $2\pi/L_0 \leq k \leq 2\pi/l_0$ the Kolmogorov spectrum is given by (Tyson 1998)

$$\Phi_n(k) = 0.033C_n^2(s)k^{-11/3}, \quad (2.3)$$

where $C_n^2(s)$ is called the structure constant at position s along the optical path. It is a measure of the strength of the refractive index fluctuations. Several experiments that measure the value of $C_n^2(s)$ have been developed. These include balloon borne and laser propagation experiments, differential image motion monitors (DIMMs) which can be used with multi-aperture scintillation sensors (MASS) (Tokovinin and Kornilov 2007), scintillation detection and ranging (SCIDAR) (Avila et al. 2001), and microthermal

measurements (Turner et al. 2010).

Ishimaru (1978) presented an alternative form of equation 2.3, called the von Karman spectrum, that was useful for large finite outer scales,

$$\Phi_n(k) = \frac{0.033C_n^2(s)}{(k^2 + k_0^2)^{-11/6}} \exp\left(-\frac{k^2}{k_m^2}\right). \quad (2.4)$$

where $k_0 = 2\pi/L_0$, and $k_m = 5.95/l_0$.

The real atmosphere is complex and laminar, with each layer having its own wind speed and average turbulent cell size. Fried (1965) nevertheless defined a single parameter, r_0 , that characterises seeing. Commonly called the atmospheric coherence length or Fried parameter, r_0 is the average size of a turbulence cell integrated over the optical path through the atmosphere. That is, it is the size of the region in which the wavefront phase distortion is less than 1 rad^2 . Fried’s numerical expression for r_0 , for infinite plane waves, is

$$r_0 = (6.88/a)^{3/5} \quad (2.5)$$

where, for optical path s ,

$$a = 2.91 \left(\frac{2\pi}{\lambda}\right)^2 \int_{path} ds C_n^2(s). \quad (2.6)$$

Based on independent measurements of $C_n^2(s)$, (e.g. by Meinel (1963)), Fried and Mevers (1974) found that because of the randomly fluctuating nature of atmospheric turbulence, r_0 is a log-normally distributed variable. They estimated that, observing at night from a good sight, for $0.55\mu\text{m}$ light and zenith propagation, the median value of r_0 is 0.114 m. For other wavelengths and zenith angle z the median value can be approximated by

$$(r_0)_{median} = 0.114 \left(\frac{\lambda}{5.5 \times 10^{-7}}\right)^{3/5} (\sec z)^{-3/5}. \quad (2.7)$$

The instantaneous value of r_0 varies with location and weather, as well as diurnally, and must be measured. One method suggested for non-stellar sources is to obtain

a time series of images of an extended object and evaluate the ratio of the observed squared modulus of the average Fourier transform and the observed average power spectrum (von der L  he 1984). In recent times much work has been done to measure seeing in terms of r_0 , and it has become an integral part of observatory site testing.

The more turbulence at a given moment, the smaller is r_0 and the more turbulence cells are seen by a telescope. So the seeing-limited resolution of a telescopic image is determined by the parameter D/r_0 .

Turbulence in front of a telescope distorts the wavefront in three ways. The first is that the direction of the wavefront may change. This is a low order distortion called wavefront tilt, caused by turbulence on scales substantially larger than the telescope aperture ($l \gg D$). The effect is that the entire image is translated some distance in the image plane. Tilt does not distort the instantaneous appearance of the image, but over time the fluctuations of tilt, called jitter, will make the entire image dance randomly about a mean position in the image plane. In a long exposure image this is the most significant component of wavefront distortion (Fried 1965).

For moderately large scale turbulence ($l \geq D$) there may be uncorrelated displacement of different points in the image (Young 1974). This second effect has been described by Baumgardner et al. (2000) as “rubber sheeting”. It is apparent when observing an image over successive instants, measuring the changing vectors between objects or features.

The third imaging effect is that many small cells across the aperture ($l < D$) cause high spatial frequency (high order) distortions of the image. Images of small, localised objects such as stars are often broken up into small sub-images called speckles. The movement of the cells across the field over the image exposure time results in blur. In a star image, energy is taken away from the central peak of the Airy disc and spread out across the surrounding rings, resulting in an approximately Gaussian PSF called a seeing disc. Seeing is quantified as the full angular width at half the maximum value (FWHM) of the seeing PSF, and at good nighttime observing sights is usually in the range of 0.4-2.0 arcseconds.

One measure of the quality of a star image is the Strehl ratio, which is based on

sharpness criteria developed by Strehl (1895; 1902). It is defined as the peak intensity of the observed seeing PSF divided by the peak of the diffraction limited PSF for the same optical system (see figure 2.1). A diffraction limited PSF therefore has a Strehl ratio of 1. In a disrupted wavefront, energy will spread away from the centre, giving a lower Strehl ratio. Without prior knowledge of the ideal PSF, the Strehl ratio may be calculated in a number of ways (Roberts et al. 2004). For random Gaussian aberration, and where $D \gg r_0$, the Strehl ratio may be approximated by

$$S \approx \exp(-\sigma^2), \quad (2.8)$$

where σ^2 is the variance of the aperture averaged wavefront aberration (Roggemann and Welsh 1996).

According to equation 2.1, when D is small the diffraction pattern is wide, and if $D \ll r_0$ the atmospheric distortion is negligible and the image is diffraction limited, but with low resolution. Increasing D makes the Airy disc size smaller, thereby increasing diffraction resolution. However, there are now more cells across the aperture, enlarging the seeing disc and reducing resolution. Fried (1965) showed that “increasing the lens diameter beyond r_0 increases the phase deviation so rapidly that the achievable angular resolution is not improved beyond λ/r_0 ”. When $D \gg r_0$ the width of the seeing disc is always greater than that of the Airy disc, so the angular resolution of even large aperture telescopes is limited by seeing. This is illustrated by figure 2.2. In imaging terms, D/r_0 is approximately the ratio of the diameters of the seeing disc to the Airy disc. It is also roughly the number of speckles across a diameter of the seeing disc (Young 1974).

In discussing image quality, Fried (1966) defined resolution as the integral of the imaging system’s ensemble-average modular transfer function (MTF) over spatial frequencies f ,

$$\mathfrak{R} = \int \langle \tau(f) \rangle df. \quad (2.9)$$

The MTF, represented by $\langle \tau(f) \rangle$, is the normalized two-dimensional Fourier transform of the image.

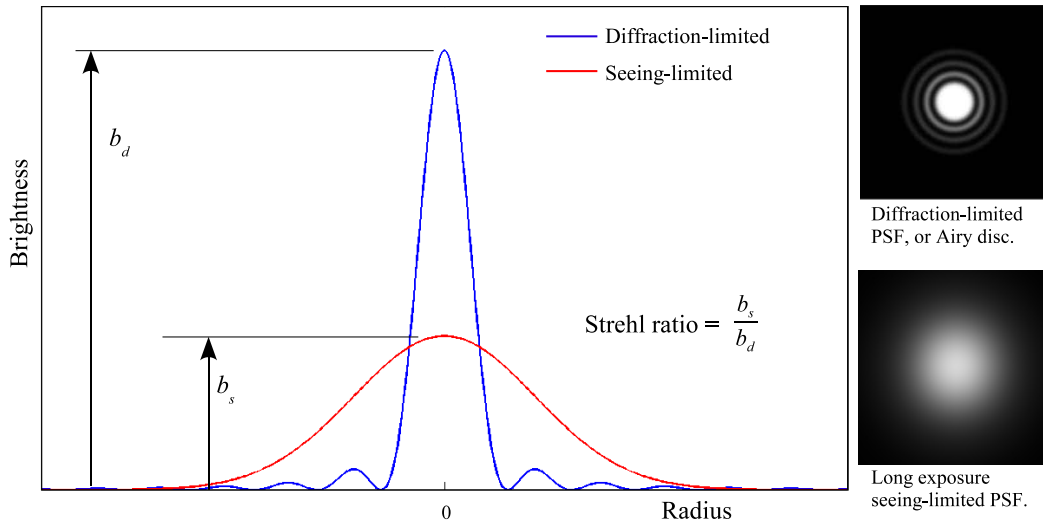


FIGURE 2.1: Graphs (left) and images (right) of diffraction-limited and seeing-limited point spread functions of a star image.

With increasing aperture the long exposure normalised image resolution $\mathfrak{R}/\mathfrak{R}_{max}$ reaches its maximum when $D \approx r_0$. So \mathfrak{R}_{max} is the resolution that would be achieved by an aperture r_0 in the absence of seeing. The seeing limited angular resolution for cases where $D \gg r_0$ is given by (Vernin and Munoz-Tunon 1995)

$$\theta = \frac{0.98\lambda}{r_0} \text{ radians.} \quad (2.10)$$

Here the resolution is no longer determined by the telescope diameter, only by the seeing. It is important to note, however, that large apertures are still needed for their light gathering abilities, which improves the SNR, particularly for observing faint objects. Because $r_0 \propto \lambda^{6/5}$ the resolution improves at longer wavelengths.

The angular area θ_0 over which wavefront distortions are well correlated, and hence the seeing PSF is reasonably constant, is called the isoplanatic patch. Its size is approximated by the equation (Roddier et al. 1982)

$$\theta_0 = r_0/h \sec z, \quad (2.11)$$

where h is the average height of atmospheric turbulence. Again, θ_0 constantly fluctuates

and its statistics must be measured.

Similarly, the time during which the seeing PSF is constant is called the coherence time, τ_0 . The temporal fluctuations of wavefronts are caused by the transport of turbulence cells across the pupil by local winds. There are various ways of defining τ_0 . The simplest definition is the time taken for the turbulence to be swept one coherence length (Kern et al. 2000),

$$\tau_0 = \frac{r_0}{V}. \quad (2.12)$$

where V is the constant bulk wind velocity. Fried (1978) stated that the coherence time over which the wavefront deviation will be less than $\frac{1}{2}\frac{\lambda}{D}$ is half of that defined by Kern et al. Buscher (1988) defined τ_0 as the time lag during which the temporal structure function of the phase at some point on the wavefront has a value of 1 rad^2 . He gives the temporal structure function as

$$D_\phi(t) \equiv |\phi(t') - \phi(t + t')|^2 = \left(\frac{t}{\tau_0}\right)^{5/3}. \quad (2.13)$$

This definition has been adopted by other researchers, particularly for optical interferometry (Davis and Tango 1996; Masciadri and Garfias 2001).

Measurements of coherence time at various sites have been conducted for $0.5 \mu\text{m}$. For example, at Mt Wilson, Buscher (1994) found between 1989-1991 a median value of $\tau_0 = 6 \text{ ms}$ with 2 ms year-to-year variation. At San Pedro Mártir, Masciadri and Garfias (2001) observed an average summer/winter variation of $\Delta\tau_0 = 3.96 \text{ ms}$, but Buscher found the night-to-night variation to be greater than the seasonal variability.

An image exposed for $t < \tau_0$ will have minimal blur, but retain instantaneous tilt, distortion and speckling. But since instantaneous tilt produces only displacement of an image, it is not a factor in reducing resolution. So a very short exposure image will have a resolution of around $\lambda/3.4r_0$. This improves the resolution over long exposure imaging by a factor of 3.4 (Fried 1965).

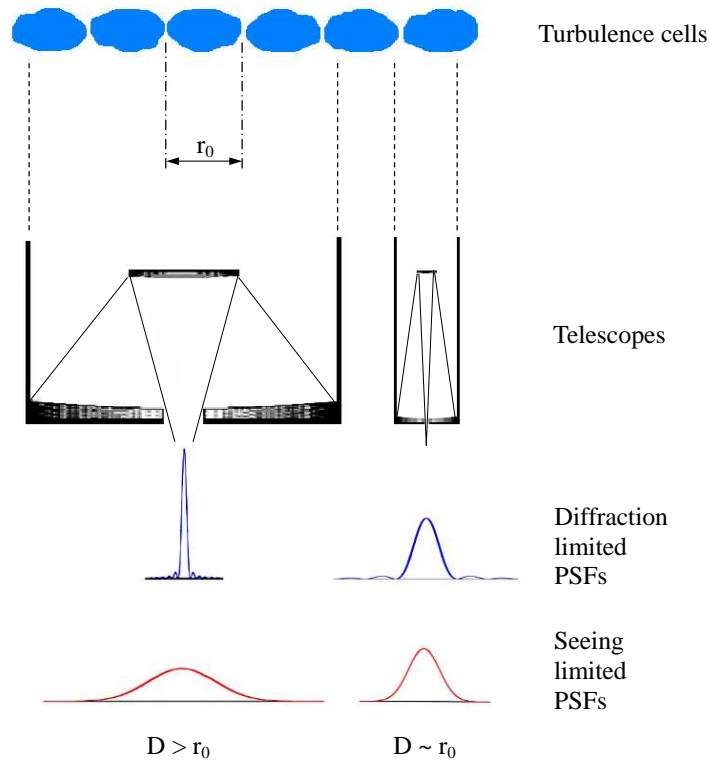


FIGURE 2.2: Diagram of the effect of aperture D on the ideal and seeing PSFs for given seeing. At right is a small telescope with $D/r_0 \sim 1$, for which the seeing PSF is only slightly wider than the ideal, and the Strehl ratio is almost equal to 1. At left is a larger telescope such that $D/r_0 > 1$. The ideal PSF is narrow, but the seeing disc is smeared out slightly wider than that for the small telescope, and the Strehl ratio is low.

2.3 Methods of Overcoming Seeing

It is useful to briefly review historical attempts at overcoming seeing. By doing so we can justify the use of selective imaging by acknowledging any limitations of other techniques, but also learn valuable lessons to apply to selective imaging.

The first way forward in tackling the seeing problem was to take Isaac Newton's advice, and build observatories on mountaintops. Hence today most of the world's great observatories are located on a handful of selected mountains, mainly in Hawaii, Chile and the Canary Islands. This raises the telescope above much of the troposphere, responsible for most seeing, and also above most moisture and cloud, increasing the available spectrum and the percentage of clear nights. Seeing is thus improved, but it is not eliminated. Also, such sites are remote from communities and industries, so

there is a great cost in building and staffing distant observatories. This, in turn, means there are far fewer instruments than astronomers wishing to use them, so there is a limit to how much science can be done.

In recent decades many space telescopes have been deployed, the most famous being the Hubble Space Telescope, and several new ones are being developed. There are also plans to build instruments on the Moon (Borra et al. 2007). All images produced by these instruments are limited only by the quality of the optics. However, the competition for observing time is more fierce, and the cost of building, maintaining and running such instruments are orders of magnitude greater than for high altitude sites.

The progressive advancement of optical and computing technologies has facilitated other means of improving resolution. These methods of reducing the effects of seeing fall into three broad categories: interferometric, speckle, and adaptive optical (AO) techniques.

2.3.1 Speckle Interferometry and Imaging

As early as the 1920s Michelson and Pease (1921) were using an optical interferometer to measure stellar angular sizes and stellar disc intensity distributions by analysing interference fringes rather than images. The measurements they made reached the diffraction limit for the Mt Wilson 100” telescope that was used.

For a long time the speckling of star images was seen as a curse. Labeyrie (1970), however, realised that each speckle contains high spatial frequency information on the object, which is lost in the blur of long exposure images. Each speckle is, in fact, a distorted sub-image caused by interference of rays from different isoplanatic patches. Labeyrie’s technique of speckle interferometry involved taking a series of short exposure frames through a mask with two or more sub-apertures to produce a time series of interference patterns. The spatial frequency information was found by obtaining the squared modulus of the Fourier transform (power spectrum) of each interference pattern, then finding the average squared modulus. Both Michelson’s and Labeyrie’s methods were used for astrometric measurements at the diffraction limit,

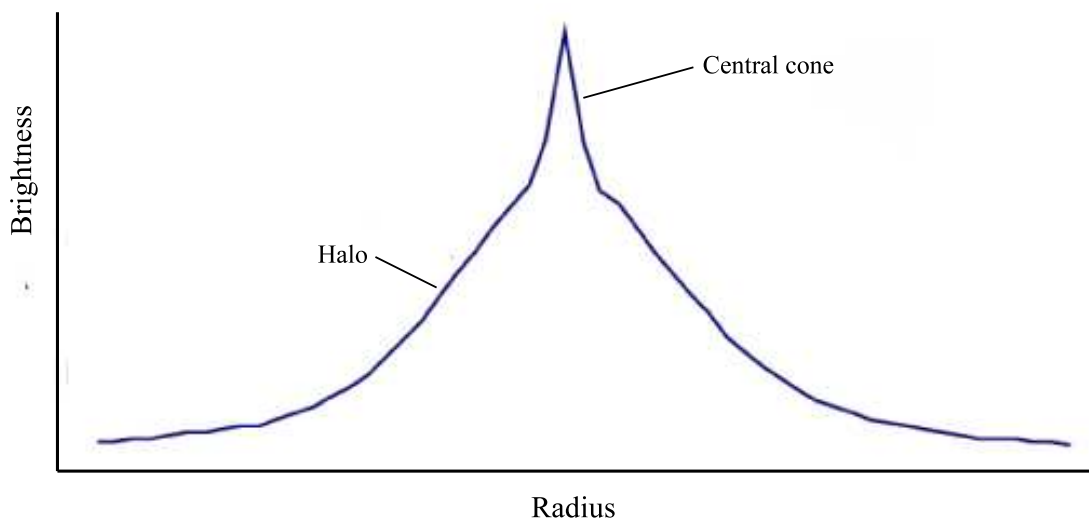


FIGURE 2.3: Point spread function of a star image with tilt removed.

but produced no object images.

The first speckle imaging was achieved by Lynds et al. (1976). Like Labeyrie, they took a series of short exposure specklegrams, but through a single aperture. In each specklegram they gave a weight factor to each speckle according to its intensity, and made an "impulse array" from the positions and weights. Each frame was shifted according to its impulse array, and then the frames were averaged. They obtained the first images of stellar discs such as α Orionis. This method was modified by Cady and Bates (1980) who made the simplifying assumption that the brightest speckle is a distorted sub-image of the brightest part of the image. Hence, in a time series of specklegrams, they located the brightest speckle in each frame by the peak pixel value, and translated the entire frame so that this speckle was centred. With all frames thus shifted they then averaged all the frames. Obviously this can only work for images in which there is one point source that is significantly brighter than the rest. For extended low-contrast objects or multiple stars of equal magnitude, some other method of alignment, such as locating the image centroid, must be used. The general method of aligning and averaging frames has become universally known as the "shift-and-add"

technique. The effect on the PSF of shift-and-add, or removing tilt, is to produce a bright central “cone” surrounded by a halo that diminishes with radius (see figure 2.3).

Labeyrie’s technique was eventually adapted to imaging. Here, the average squared modulus of a series of specklgrams, taken through only one aperture, is convolved with similar data from a reference star, called a guide star, imaged simultaneously. The guide star provides a point source with the same optical transfer function as the object, in order to obtain successive instantaneous PSFs. The image is recovered by taking the inverse Fourier transform of the convolution. A more advanced version passes the guide star signal to a device called a wavefront sensor. This measures the local wavefront tilt across the image, typically by passing the light through an array of small lenslets that focus onto spots on a CCD. The relative movements of the dancing spots, corresponding to changes in wavefront tilt, are measured. This information is then convolved with the image signal.

An essential requirement is for the guide star to be in the same isoplanatic patch as the target object. If the guide star were in a different patch, the convolution would produce a worse image. The need for short exposures imposes a minimum limiting magnitude on useful guide star. Speckle imaging is therefore limited to targets that are close to sufficiently bright guide stars.

In cases where there is no guide star, the instantaneous PSF is unknown. A range of speckle imaging techniques collectively called blind deconvolution have been developed for this situation (Ayers and Dainty 1988; Lane 1992; Jefferies and Christou 1993). The speckle frames are filtered to produce an estimate of the object, using certain assumptions about the true image. This estimate is then used in the deconvolution. The estimation is usually iterative. The object estimate is revised many times until some quality criteria are reached. Blind deconvolution imaging methods have also been developed for terrestrial surveillance, especially for police and military (Mohaammed and Burge 1988; Glick et al. 1991; Fishbain et al. 2007). For example, Glick et al composed their image by assigning each pixel its most common (mode) value from a series of short exposures, rather than the average.

2.3.2 Adaptive Optics

By the 1950s electro-mechanical means of wavefront compensation were being explored. These methods are collectively known as adaptive optics or AO. Just as in speckle methods, the incident light is split so that a guide star can be monitored. The image signal is then brought to a movable mirror. The guide star aberration information is used to control the movable mirror such that it corrects the wavefront distortions in the image beam in real time. The result is a long exposure with substantially reduced wavefront aberration.

The first type of AO was pioneered by Leighton (1956). He used a gimbal mounted flat mirror that was moved such that the image was kept centred, thereby removing tilt. This type of AO is called tip-tilt correction. It is analogous to the shift-and-add method, and leaves only high order distortions in the image. Because tilt is caused by large scale turbulence the isoplanatic patch is larger than for high spatial frequencies. This increases the number of possible science targets around a available guide stars.

At around the same time, Dewitt et al. (1957) used television apparatus for tip-tilt correction in planetary imaging. Again the image beam was split using a dichroic element. One half was passed through two orthogonal slits and the light through each was measured by photocells. The other half was imaged on a television. As the planet danced about, the light through the slits varied. The resulting photocell currents were fed to deflection coils around the television orthicon tube to keep the image centred.

Babcock (1953) proposed the first method for correcting high-order distortions. His compensating mirror was coated in an oil. The oil thickness was electrostatically controlled so that the refraction of the image would compensate for aberrations. In recent decades deformable mirrors controlled by electromechanical actuators are used. For effective correction, both in tilt and high order distortion, the response of the system must be faster than the Greenwood frequency, defined as $f_G = 1/\tau_0$ (Greenwood 1977).

AO systems have been retro-fitted to various older large telescopes, and are integrated into the design of newer telescopes. Many use both tip-tilt and high order correction. However, AO suffers from the same guide star limitations as speckle methods. Some AO systems therefore use lasers as artificial guide stars (LGS). A laser

is propagated up through the atmosphere, and the returning wavefront is monitored, providing information on high-order turbulence. However, a natural guide star (NGS) is usually still needed, only to obtain tip-tilt information. Natural guide stars used with LGS systems can be fainter and further from the target than for pure NGS systems. This increases the sky coverage of LGS AO systems (Davies et al. 2008; Clare et al. 2007). However, the laser wavelength must be chosen so that its atmospheric dispersion is visible. AO compensation will then be made at the wavelength of the laser, thus imposing a wavelength limitation on imaging. This situation is improving with the development of polychromatic LGS systems (Pique et al. 2006).

The Strehl ratio is the most commonly used measure of the quality of adaptive optics images, and as such is used to measure AO system performance. Various observers and observatories use different Strehl ratio measurement techniques, making it difficult to compare results from different papers (Roberts et al. 2004). However, when developing an imaging system, it is usually not the absolute Strehl ratio that is important, but the relative improvement in Strehl ratio. So any suitable measurement method may be selected, as long as it gives consistent results in all imaging conditions and parameters in a given experiment.

An AO image or system is considered well corrected if it produces a Strehl ratio ≥ 0.8 . This is called the Marechal criterion, and corresponds to a wavefront aberration of $\sigma \simeq \lambda/14$ (Graham 2003). Strehl ratios of this order have rarely been achieved in practice. One example was in the use of laser guide-star adaptive optics (LGSAO) on the 10 m Keck II telescope. Ghez et al. (2005) achieved Strehl ratios between 0.62 and 0.76 in their L' ($3.8 \mu\text{m}$) band observations of the galactic centre. A more unusual and extreme example was the use by Peters et al. (2008) of a $D=25.4 \text{ mm}$ aperture mask on an 8 inch refractive telescope at Steward Observatory in Arizona to achieve $D/r_0 \sim 0.5$. In this little explored and, for all practical purposes, diffraction limited regime they achieved Strehl ratios of 98-99% using a high-speed tip-tilt correcting mirror. In chapter 6 I will show that the use of frame selection can produce Strehl ratios that are competitive with those from AO, with a much smaller investment in hardware.

2.4 Summary

Astronomical images taken through earth-bound telescopes are blurred by atmospheric turbulence. The instantaneous PSF is a cluster of speckles, which is the interference pattern caused by the turbulence cells in the atmosphere. Over time the speckles blur so that a long exposure PSF has an approximately Gaussian profile.

Short exposures freeze the turbulence, thereby reducing blur, but do not eliminate the instantaneous distortions. Co-aligning short exposure frames effectively removes tilt, but leaves distortion and speckling. Speckle imaging is effective at improving resolution, but only if some knowledge of the object is available. One method of obtaining such knowledge is the use of wavefront sensors with guide stars. This increases the complexity and therefore the cost of imaging instrumentation, and limits potential targets to those within the same isoplanatic patch as a suitable guide star. Blind deconvolution speckle imaging increases the computational complexity of the image processing.

Adaptive optics is also very effective at removing the effects of turbulence, but has the same guide star limitations as speckle imaging. With the development of compact tip-tilt systems and deformable mirrors, AO is becoming more suitable for use on smaller telescopes, but is still complex and expensive.

All of the methods mentioned above are effective at overcoming turbulence induced image aberrations. In particular, AO is crucial in obtaining the diffraction limit of large aperture telescopes, which are necessary for faint objects and deep sky surveys. However, even AO has limitations, and gaps in its applicability. Frame selection can fill some of these niches. It can be used in conjunction with the other techniques, but on its own it is suitable for use on smaller, more common telescopes, for a fraction of the investment in equipment and software, and so is more accessible.

In the next chapter I describe the history and theory of the frame selection method, also known as lucky imaging. I will show that it can be used to overcome the limitations of speckle imaging and adaptive optics.

Chapter 3

Selective Imaging

3.1 Introduction

Selective imaging is the method suggested by Fried (1978) of obtaining many consecutive short exposure images, analyzing each frame for sharpness and selecting only those that satisfy the required quality criteria to combine into a final image. Short exposures restrict the blur due to image motion, and leave only instantaneous tilt displacement and high order distortions. The best frames will be those taken during the random moments of minimal atmospheric disturbance. As such, it is a variation of the “shift-and-add” method. Rejecting the poor frames reduces SNR, but this can be mitigated by recording many hundreds or thousands of frames. The gain is in the resolution of the final image.

This chapter describes the frame selection method. I will take a zig-zag path through the history in order to illustrate the important concepts. I then explain the available frame selection methods, particularly the sharpness metrics used for measuring and ranking the frames.

3.2 History

Platt (1957) noted that various observatories had attempted to obtain a few good snapshots by culling hundreds taken in series, demonstrating post-selection. This may

be seen as wasteful of the majority of photographs that were rejected. He proposed a system whereby a single high resolution image could be built up by exposing a photographic plate only during moments of good seeing, using a shutter controlled by a “time-selection” device. Since a long exposure is really an integration of many shorter moments, this method is equivalent to the modern idea of selective imaging described above. The device he suggested used photometry of a guide star for time selection.

A version of Platt’s experiment was built and tested by Anisimov et al. (1970). However, instead of one long exposure integrated over ideal moments he displayed the telescope image on a television screen, and recorded the screen image with a motion picture camera triggered by a seeing monitor. Trials were made through a 0.2 m aperture telescope. Anisimov compared the images made using the seeing quality monitor with those made by simply recording bursts of frames at regular intervals. Without seeing quality control they found that 0.16% of frames were satisfactory, and estimated that one good frame could be recorded in around 30 minutes. With quality control they achieved a yield of 1.15%, meaning a good frame could be found in about 10 minutes.

Fried (1978) provided the first analytic description of selective imaging probabilities. He found that the probability of any given short exposure frame having a wavefront distortion less than 1 rad^2 is

$$P \approx 5.6 \exp \left[-0.1557 \left(\frac{D}{r_0} \right)^2 \right] \quad (3.1)$$

for $D/r_0 \geq 3.5$. The main parameter is D/r_0 , which is the telescope aperture normalised for the seeing conditions, or the aperture expressed in units of r_0 . On solving this equation, it can be seen that even for a moderate sized telescope where $D/r_0 \sim 10$, the number of acceptable frames will be less than 1 in 10^6 , and so many millions of frames will be required to maintain an acceptable SNR. This will severely stretch computer storage resources and observing times (recording 25 frames per second, over 11 hours to get 1 good frame!). If we used a smaller telescope with $D/r_0 \sim 5$, the odds improve to 1 in 9. This is a drastic improvement, but at the cost of diffraction limited

resolution. Fried (1966) determined that, in the far-field short exposure regime, the optimal resolution will be obtained when $D/r_0 \sim 7$, at which the odds are around 1 in 370.

Beckers and Rimmele (1996) found that the Fried probability only applies to perfect telescope optics, and dubbed this the “lucky observer” imaging mode. When frame selection is used on telescopes with moderate aberrations, the sharpest frames will be those taken when the atmospheric wavefront aberrations cancel those of the optics, rather than simply when the atmospheric turbulence is minimal. They found that the probability of a good frame in this situation is less than the Fried probability, and called this the “very lucky observer” mode.

The development of electronic computer storage and processing capability and fast read-out electronic cameras in the 1980s meant selective imaging could be attempted more easily. One of the first uses of selective imaging in this period was by Lelievre et al. (1988) on the Canada France Hawaii Telescope. They masked the 4 m aperture into 9 sub-pupils with sizes ranging up to 1m. Imaging binary stars with a photon counting camera achieved a resolution of 0.26 arcseconds by selecting the best 10% of frames. They found the resolution improved by a factor of 3 over traditional long exposure imaging that used the whole aperture. This was not as great a gain as expected, and they conceded that the 0.4 s frame exposure time may not have been short enough to sufficiently freeze the image motion.

Because selective imaging relies on fast shutter speeds, it is most easily applicable to bright objects, such as bright stars, the Sun, Moon, solar system planets, nearby minor planets and Earth orbiting satellites. Dantowitz (1998) attracted the interest of the U.S. National Reconnaissance Office with his images of orbiting satellites, the space shuttle and the Mir space station. He called his technique Selective Image Reconstruction (SIR). Images were recorded onto video tape using a 12 inch or 16 inch telescope, and frames selected by eye. As a result of Dantowitz’s article in the popular astronomy magazine “Sky & Telescope”, many well equipped amateur astronomers were inspired to try selective imaging on planets using video cameras or webcams, with remarkable results. Meade, Celestron and other telescope manufacturers now have proprietary

planetary cameras with software that use selective imaging. In addition, there are now a number of available astronomical image processing software packages, the most famous being Registax (Berrevoets 2008), that incorporate or are based on selective imaging.

Green and Hunt (1999) used simulations to further develop Dantowitz's work for the purpose of tracking and cataloging of artificial satellites. They took as their object data a close-up photograph of the Hubble Space Telescope, and added aberrations at various SNRs to simulate consecutive turbulence degraded image frames. They applied blind deconvolution algorithms to estimate the object. Frame selection was used and found to give better results than speckle imaging alone.

Early on, a significant niche application of selective imaging was found. Because of Mercury's proximity to the Sun, the Hubble space telescope cannot be used on it, and since imaging is often done in daylight or twilight there are no nearby guide stars for adaptive optics. Warell and Limaye (2001) began imaging Mercury in 1995 with the 0.5 m Swedish Vacuum Solar Telescope (SVST) on La Palma. Although only the best frames were selected each finalist was significantly post-processed individually, so this was not "shift-and-add" type selective imaging. However, they resolved detail to around 200km, which achieved the diffraction limit for that telescope of 0.28 arcseconds at $\lambda=550$ nm, and compiled a global map of Mercury.

Dantowitz et al. (2000) began using their SIR technique in 1998 on the 60 inch (1.5 m) Mt Wilson telescope to detect albedo features on previously unmapped areas of Mercury. Frames were recorded in analogue on video tape. They used 16.7 ms exposures at 60 Hz and selected frames by pixel gradient across Mercury's bright limb. The final image was post-processed by un-sharp masking. Baumgardner et al. (2000) used the same telescope on the same day to test the selective imaging component of a spectral imaging system designed to analyse Mercury's tenuous atmosphere (Wilson et al. 2004; 2006) but recorded frames digitally. Although the resulting images appeared different from those by Warell and Limaye, because of the different processing, the albedo features agreed and they achieved the same resolution (Mendillo et al. 2001).

Others who have imaged Mercury by selective imaging are Ksanfomality (2003),

and Cecil and Rashkeev (2007). Features found on Mercury by these teams are in agreement with each other, and with those regions that were mapped by Mariner 10. It was found in some cases that bright features were not in good agreement with radar data.

Davis and North (2001) used Dantowitz’s SIR method to image bright binary stars. They compared their resulting measurements of angular separation, magnitude difference and position angle with those known from other imaging techniques, and found good agreement. Like Dantowitz, they recorded images onto video tape and scanned the tape visually frame-by-frame. Rather than shift-and-add the best frames, they measured the binary parameters on each best frame and averaged the measurements. This is a form of frame selection, and appropriate for astrometric measurements, but it did not produce a single high resolution image.

The recent development of fast low-noise cameras has allowed the use of selective imaging to be extended to faint objects. Over the past few years the “Lucky Imaging” team from the Institute of Astronomy and Cavendish Laboratory, University of Cambridge, UK have discovered many faint low-mass binaries using frame selection on images taken with an Electron Multiplying CCD (EMCCD) system called “Luckycam” through the 2.56 m Nordic Optical Telescope. This telescope gave, on average, approximately $D/r_0 \approx 7$, matching Fried’s predicted optimum normalised aperture. They measure the Strehl ratio of a guide star for frame selection. Because the EMCCD has very low readout noise they were able to image very faint objects at high frame rates, achieving FWHM smaller than equivalent images taken by the HST, of similar aperture (Baldwin et al. 2001; Tubbs 2004; Law et al. 2005). These experiments were supplemented by simulations to explore frame selection parameters (Baldwin et al. 2008). Experiments have also been carried out using a Luckycam at the back of the Palomar 5m AO system (Law et al. 2007), which produced significantly finer resolution than HST because the combination of AO and frame selection made the most of the larger aperture. Further, proposals for using Luckycam arrays on large segmented aperture telescopes to assemble image mosaics have been made (Mackay 2006; 2005). This essentially combines frame selection with AO and speckle interference techniques,

over a very wide field ($\gg \theta_0$). Promising results have been obtained with “Luckycam High Res” on the 3.6m NTT at La Silla, Chile (Mackay 2007).

Bailey and Chamberlain (2006) achieved the sharpest ground based images of Mars to date using the UKIRT during the 2003 opposition. They took several series of 60 or 80 frames, with a frame exposure time of 90 *ms*. Observing in the near IR utilised the larger r_0 and longer coherence time, as well as the good seeing at Mauna Kea. These factors combined such that D/r_0 was optimised even for the 3.8 m aperture. From each series the original frames were analysed visually and the best 10% were selected. The frames were shifted and combined using median pixel values. Once again the results compared favourably with similar HST images.

As mentioned in section 2.3.1, much work has been done in the restoration of images for terrestrial surveillance. Some researchers have incorporated selective imaging. In particular Carhart and Vorontsov (1998) have made use of Fried’s suggestion that some frames that are not completely sharp may still have small undistorted areas (Fried 1978). They developed an algorithm that detects and combines sharp local regions within a series of short exposure frames. This method was found to be effective in anisoplanatic imaging, where the field of view is greater than the isoplanatic angle. It was, however, susceptible to variations in tilt across individual frames (Vorontsov and Carhart 2001).

All of the studies thus far have concentrated on the imaging regime, observing site or application of the particular project. As such they have only explored small ranges of parameter space.

3.3 Frame Selection Methods

The success of selective imaging depends critically on the method used to select the best frames. There are a range of methods, with various hardware, software and time requirements. Some perform post-selection on a set of previously recorded images, and therefore require large storage capacity. Others scan images as they are recorded and discard them before combining if they don’t measure up. All methods need some

quality criteria with which to measure and rank the frames.

The simplest method for frame selection is to look at them visually, as did Dantowitz (1998), Davis and North (2001) and Bailey and Chamberlain (2006). Unfortunately this is also the most subjective and time consuming method. For efficiency and repeatability it is necessary and desirable to automate the process.

The first automated systems used photometric seeing monitors to trigger their cameras. The device suggested by Platt (1957) used a photomultiplier tube to measure the light from a guide star passed through a small aperture. When the seeing was good, the seeing disc would shrink, and more light would pass through the aperture and register on the photocell. When the current exceeded a threshold value the shutter would open. The desired resolution would be determined by the aperture size. Anisimov's seeing monitor took light from a guide star and projected it onto the edge of a dividing prism. From there each half of the beam was monitored by a photocell. When the seeing was good and the star was stable, the currents through the photocells were equal and the camera was triggered. When the star scintillated, the currents were unbalanced and the camera was stopped (Anisimov et al. 1970). Although these are time selection rather than frame selection mechanisms, they are equivalent because each short exposure frame represents a moment in time.

Modern frame selection methods make use of a range of software algorithms to scan frames according to some sharpness metric. A sharpness value is thus given to each frame. For selection one may either set a threshold minimum sharpness score, or, in a previously recorded image series, set the fraction of frames to accept. This fraction is called the Frame Selection Rate or *FSR*.

3.3.1 Image Sharpness Metrics

Muller and Buffington (1974) suggested several image sharpness metrics to be used to measure AO system performance. The metrics are formulae from which software algorithms may be developed, so that an image can be measured to produce a sharpness score. These metrics take their maximum value when measuring the diffraction limited image (Roggemann and Welsh 1996). Some of them can be used in frame selection.

The first two are useful for images of point sources. The first of these is defined by

$$S_1 = \int I^2(x, y) dx dy \quad (3.2)$$

where $I(x, y)$ is the irradiance at pixel (x, y) . Squaring the pixel values before the integration gives weight to small bright areas. The second sharpness metric is

$$S_2 = I(x_0, y_0) \quad (3.3)$$

the brightness at an arbitrary pixel (x_0, y_0) . When an image has a single brightest point, (x_0, y_0) can be set to the location of the brightest pixel. This is equivalent to measuring the Strehl ratio of the brightest star in the image. The brightest pixel is also used for frame alignment in the Cady and Bates (1980) shift-and-add method. Because of its simplicity we chose S_2 to measure and align our stellar images, which we used to test the behaviour of the frame selection method.

The next metric is useful for extended objects. It utilises partial derivatives of pixel values.

$$S_4 = \int \left| \frac{\partial^{m+n} I(x, y)}{\partial x^m \partial y^n} \right|^2 dx dy, \quad (3.4)$$

If $m = n = 1$ the partial derivatives become the pixel gradient, which is a measure of contrast. Squaring gives weight to small areas of high contrast. One algorithm to find pixel gradients is the following contrast operator used by Baumgardner et al. (2000) when imaging Mercury.

$$C(i, j) = |P(i, j) - P(i + 1, j + 1)| + |P(i + 1, j) - P(i, j + 1)| \quad (3.5)$$

where $C(i, j)$ is the pixel difference measured between diagonally adjacent pixels around pixel (i, j) , and $P(i, j)$ is the pixel value at (i, j) . Squaring and summing to calculate S_4 is then straightforward.

The last of Muller and Buffington's metrics was the "fidelity defect" function,

$$S_8 = - \int | I(x, y) - I_0(x, y) |^n dx dy \quad (3.6)$$

which measures differences between the recorded image and the ideal one. This, of course, requires prior knowledge of the diffraction limited image. S_8 is useful for system calibration, or when using a guide star for frame selection.

Roggemann et al. (1994) have used a modified version of S_1 in frequency space;

$$S_{S1} = \int_{|u| \leq D/\lambda d} | I(u) |^2 du, \quad (3.7)$$

where this time $I(u)$ is the detected image spectrum. So $| I(u) |^2$ is the squared modulus, or the Fourier transform of the autocorrelation. $D/\lambda d$ is the diffraction limited cutoff frequency for the telescope, where d is the distance between the exit pupil and the image plane. Setting this as the upper integration limit eliminates from this metric those components of photon and readout noise with spatial frequencies beyond the telescope cutoff. When images are blurred fine detail is lost; that is, high spatial frequencies are attenuated. Frames with strong high spatial frequencies will score well. So S_{S1} is universally applicable to extended objects, and we used it for experimental observations of the Moon and solar system planets. For comparison some runs were also processed using the contrast operator, equation 3.5, given above.

Note that these metrics measure high order distortions, so frames with high sharpness scores may still have tilt and uncorrelated low-order distortions (rubber sheeting). Shifting and combining is still needed to correct for tilt.

For cases where the field of view is greater than θ_0 (anisoplanatic imaging) the probability of a given short exposure frame having a sharp local region is given by the Fried equation (equation 3.1), even if the image as a whole is severely degraded. In this imaging regime it is thus desirable to only select any sharp regions from each frame. This may be done by convolving an image sharpness metric with a window function that scans across each frame. To this end, Vorontsov and Carhart (2001) developed

their Synthetic Imaging method. They set up an initial blank synthetic image, and for each new frame used an “evolution equation” to update the synthetic image if any local region of the new frame was sharper than the same region of the synthetic image. The window size corresponds to the parameter D/r_0 , and must be optimised for best results. In scanning and updating many window positions in each frame, this method requires a great deal more computer processing time than simply scanning whole frames.

3.4 Summary

The frame selection or lucky imaging method involves co-aligning and combining only the best of a series of short exposure frames. Frames can be chosen during observation if they meet the required quality level, or post-facto either by quality threshold or by selecting a desired fraction of the best ranked frames. The probability of a short exposure frame meeting a strict quality criterion is a function of the seeing-normalised aperture D/r_0 ; small D or large r_0 give more good frames. The resolution and the probability are optimised when $D/r_0 \sim 7$. The method has been increasingly used in a number of applications, the most high profile being the discovery of many faint binary companions. However, because of the necessity for short exposures lucky imaging is most easily applied to routine surveys of bright targets such as solar system objects using small to medium sized telescopes.

There are several image sharpness metrics that are useful for ranking frames for selection. The simplest of these is the brightest pixel (S_2), useful for fields with a single brightest star, which not only gives a measure of sharpness but also reference point for co-alignment. It was therefore chosen for use on the stellar images in the *MUSIC* project as the simplest way to test the general behaviour of the frame selection method. The S_{S1} metric that makes use of spatial frequency information was chosen for its universality to process images of the Moon and planets. The next chapter describes the experimental setup and methods for the *MUSIC* observations.

Chapter 4

Observing with the *Macquarie University Selective Imaging Camera*

4.1 Introduction

Selective imaging comes into its own when imaging bright objects such as the Sun, Moon, solar system planets and near Earth objects. In this regime smaller telescopes may be employed, so routine observing can be undertaken without competition for observing time. The object brightness gives a high SNR, so that the only special requirement for the imager is a high frame rate to minimize observing time. These factors make selective imaging the simplest and least expensive technique for high resolution planetary imaging.

At Macquarie University a selective imaging system has been used to test how well selective imaging performs at increasing the resolution of astronomical images of bright sources. The system was called the Macquarie University Selective Imaging Camera, or *MUSIC*. This system was initially tested on Macquarie University's 40cm telescope, then used in observations from the Australian National University (ANU) 1m telescope and the Anglo-Australian Telescope (AAT), both on Siding Spring mountain, NSW.

The observing log is contained in Appendix C. this chapter details the aims and methods of these observations.

4.2 Aims

The aim of this project is to investigate the effects of various parameters on the performance of a selective imaging system over a wider range of parameter space than has been previously explored. The purpose of this is to develop a software and camera package that will be able to optimise these parameters and perform frame selection in real time, which will be used for routine imaging of solar system objects.

To investigate the performance of selective imaging at restoring blurred images the resulting images must be compared with ideal diffraction-limited images. For stars the ideal PSF can be easily found for any given telescope, so imaging bright stars is the simplest way to test the frame selection method. Fields with a single brightest star were chosen so that the simplest sharpness metric of brightest pixel value (Muller and Buffington's S_2) could be used to rank and select the best frames.

The frame selection variables tested were frame exposure time t , normalised aperture D/r_0 , frame selection rate FSR , and colour band λ . In order to obtain D/r_0 the Fried parameter r_0 was measured for each observation from the simulated long exposure (stacked) image, according to equation 2.10. A number of binaries and clusters were also recorded to see the effects of frame selection on sharpness in different parts of the images. The quality of the output stellar images was measured using the Strehl ratio, chosen because it compares the real image with the ideal one. The FWHM was used to measure the stars in the stacked images in order to determine r_0 . However it is not a good measure of sharpness for shift-and-added images because a star will have significant flux in the broad halo even though there may be a narrow core.

Three measurements are of particular interest in examining selective imaging:

- The first is Strehl ratio versus D/r_0 . This will give an indication of the size of telescope aperture needed to optimise resolution for a given r_0 .

- The second is the measurement of Strehl ratio improvement over a range of frame exposure times. In selective imaging it is crucial to optimise t so that image motion is frozen but SNR is maximised.
- The third is how the shift-and-add method affects the image quality across the frame. When frames are co-aligned on a single point of high quality it is expected that the region close to that point will be of artificially high quality, and that the quality will diminish with radius from that point.

4.3 Methods

Observations were conducted using *MUSIC*, comprising a small digital video camera with a frame grabber. Time series of frames were stored as FITS cubes. Post-selection was performed using software written in C++, adapted from image capture software developed originally for the IRIS2 project and the AAO2 data controllers on the Anglo-Australian Telescope (Shortridge et al. 2004).

Images of planets and the Moon were also taken in order to test algorithms for sharpness metrics and alignment of images of extended objects.

Natural fluctuations in r_0 will create a small range of D/r_0 for a given telescope aperture. In order to explore a wide range of D/r_0 we constructed sets of aperture masks for the AAT and the ANU 1m telescope so that we could widely vary D . It is possible that the position across the telescope pupil of a mask affects the results of frame selection, particularly if there are significant optical aberrations. We did not test this variable; only one position was used for any given mask. Various colour filters were also used. For some observations a Televue Powermate 2.5 \times magnifier was used to modify the pixel resolution.

4.4 Hardware Setup

The initial imager used for *MUSIC* was a Watec Neptune 100 monochrome video camera. Two of these cameras were tested over three observing trips. The CCD had

TABLE 4.1: Summary of *MUSIC* Observing Trips

Date	Location	Instrument
8th March 2005	Macquarie University, Nth Ryde NSW	Meade 40cm SC
11th to 23rd March 2005	Siding Spring, NSW	ANU SSO 1m RC
25th June 2005	Siding Spring, NSW	Anglo-Australian Telescope
9th to 14th November 2005	Siding Spring, NSW	ANU SSO 1m RC

dimensions 768 by 576 pixels, each $8.6 \times 8.3 \mu\text{m}$. The camera produces interlaced output; that is, in each frame the camera scans the odd rows and then the even rows, and then splices them together. The camera gain and electronic shutter speed were set manually on a control box connected to the camera by a dedicated cable. The frame exposure time was determined by the shutter speed. The available exposure times were 0.1, 1, 2, 4, 8.3 and 20 milliseconds. The longest exposure was determined by the 25Hz frame rate, and achieved with the shutter “off” setting. The gain was set by a dial marked from 0 through 13. The video data was recorded using a Data Translation DT3155 PCI frame grabber mounted in a PC system using a 3GHz Pentium 4 processor. The PC was configured with 1 TB of disk space (two 400 GB and one 200 GB drives) to

TABLE 4.2: Imaging parameters of telescopes used with *MUSIC*

Telescope		Meade 40cm SC	ANU SSO 1m RC	Anglo-Australian Telescope
Full aperture diffraction limited resolution at 550nm (arcsec)		0.34	0.13	0.035
Pixel resolution (arcsec)	Without magnifier	0.43	0.22	0.057
	With magnifier	0.172	0.086	Not used
Field of view, X×Y (arcsec)	Without magnifier	329×247	165×124	43×33
	With magnifier	132×99	66×50	Not used

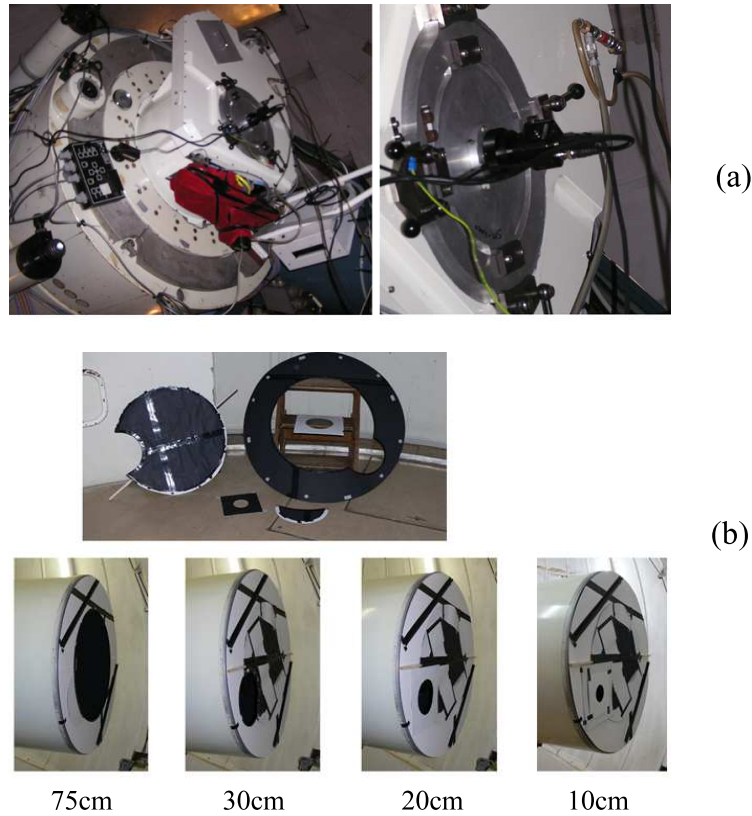


FIGURE 4.1: (a) The Watec video camera mounted at the Cassegrain focus of the ANU 1m telescope. (b) Aperture masks used on the ANU 1m telescope, unassembled (top), and assembled as indicated (bottom).

record the large data files. The operating system was Fedora Core Linux.

MUSIC was used on three telescopes. The observing dates, locations and instruments used are summarised in table 4.1. Imaging parameters such as pixel scale and field of view for each telescope, with and without the Powermate magnifier, are outlined in table 4.2. The diffraction limited resolution is given for full aperture and visible wavelength. The resolution, of course, changes for different wavelengths and aperture masks. The particular setup for each telescope is described below.

4.4.1 Macquarie University 40cm Telescope

For an initial test of the camera and image capture software, the camera was mounted on the Macquarie University's 40cm Meade LX200 $f/10$ Schmidt-Cassegrain telescope

at the Cassegrain focus by means of a C-mount adaptor attached to a standard 1.25inch barrel fixed in the eyepiece holder. This test verified that the hardware and image capture software worked well.

4.4.2 ANU 1.0m Telescope

The camera was mounted by the 1.25inch barrel at the Cassegrain focus of the Siding Spring Observatory's 1m $f/8$ Ritchey-Chretien telescope. The camera output was cabled through the wiring loom to the PC in the control room. This allowed various processes such as telescope aim and monitoring of the images to be done from the control room. However, camera adjustments had to be done from within the dome because of the limited control box cable. The telescope's built-in UVBRI filters were used. Aperture masks of 75cm, 30cm, 20cm and 10cm were constructed from cardboard such that they could be mounted on the front of the telescope. The 75cm mask was concentric with the optical axis. The rest were offset because of the large secondary mirror. The unmasked 1m aperture was also used.

4.4.3 Anglo-Australian Telescope

The 3.9m AAT afforded a greater range of apertures to try at the same site as the ANU 1m telescope. The camera was mounted by means of an "L" bracket at the auxiliary Cassegrain focus, where a diagonal mirror reflected the image out to the side behind the primary mirror cell. It proved impossible to wire the camera output through the telescope's wiring loom, so the computer's CPU had to be mounted inside the instrument cage. Furthermore, because of the limited camera control box cable, an observer had to ride in the cage during observing in order to make changes to camera settings. The aperture was masked by placing a circular wooden cover over the "chimney" at the hole in the primary mirror, as shown in figure 4.2(b). The cover had an offset hole, over which a desired sub-aperture could be placed. The size of each sub-aperture was geometrically designed to give an equivalent full-aperture mask diameter. The equivalent mask diameters used were 1.0m, 0.8m, 0.6m, 0.4m, 0.2m,

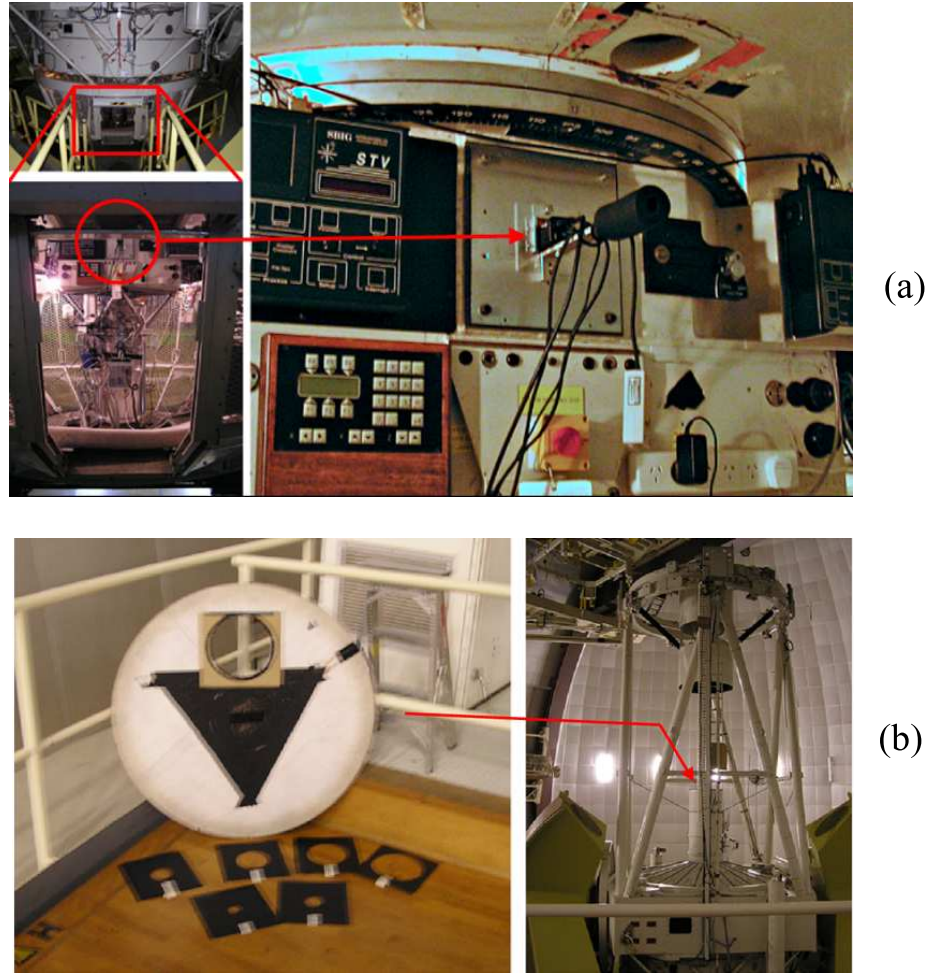


FIGURE 4.2: (a) The camera mounted on the AAT at the auxiliary Cassegrain focus (right), inside the instrument cage (lower left), under the mirror cell (upper left). (b) Aperture masks used on the AAT, unassembled (left), and their location on the chimney (right).

and 0.1m, as well as the 3.9m clear aperture. An additional 2.5m aperture was created by partially closing the mirror cover. With the AAT in $f/8$ configuration, the effective focal length is 30.78 m. The mask position was 6.35 m from the focal point, 0.2 times the focal length. The width of the camera's CCD was 7 mm, so from the centre to the edge of the frame corresponded to only 14 mm distance on the primary mirror. This was considered negligible, especially for the larger aperture masks.

4.5 Image Acquisition

The software programming for *MUSIC* was done in the C++ language. The initial programming was done by Jeremy Bailey, and I performed additions, modifications and wrote new code as required. The programs used are listed in Appendix A.

Image capture software was used to record short exposure frames in series of image cubes in the FITS format. Frame calibration and frame selection was performed later using different programs.

In order to monitor the camera output during observing, the ESO's GAIA image display program was used with a plug-in called *music_plugin.tcl* that enabled viewing of the video output from the frame grabber. The program *acquire.C* was used to send the camera frames to the GAIA display in real time during telescope pointing, focusing and camera adjustments.

To record frames as well as send new frames to the GAIA display, a program named *music.C* was employed. *music.C* took the FITS cube dimensions and output filename from a text file called *music.conf*. It then wrote the desired number of frames to that filename, with pixel values in 8 bit BYTE format.

A bias frame was created for each camera at every gain setting by covering the camera aperture and averaging 1000 0.1 ms frames taken at each gain setting. In our bias correction, camera temperature was neglected, because, using an inexpensive camera, there was no way to measure, let alone control the temperature. However, comparison of bias frames taken in summer with those taken during our winter observations showed negligible difference. At each telescope, twilight flat field frames were compiled for each filter with and without the Powermate, again by averaging 1000 frames. Since we only imaged bright objects over short exposure times, the dark current was assumed to be negligible.

To reduce file size and conserve storage capacity the image capture software allowed us to specify in *music.conf* the frame window size in pixels.

The process of recording sets of FITS cubes typically ran as follows:

1. The telescope was prepared with the camera, an aperture mask and colour filter.

The *acquire.C* program was started in order to monitor the camera output during setup.

2. The telescope was slewed to the selected target object.
3. The desired frame size and number and the output filename were saved to *music.conf*. The exposure time was set, and the gain was adjusted to produce high peak pixel values without saturation by watching the real-time image monitor using the *acquire* program.
4. The *music.C* image capture program was run to collect the desired number of frames, which were stored on the hard disc drive. This run was added to the observing log.
5. Steps 3 to 4 were repeated for various combinations of frame exposure time, colour filter and aperture mask.
6. A new object was selected, and steps 2 to 5 were repeated.

To test frame selection parameters, a number of stellar objects were targeted. Bright stars gave us a simple way to measure r_0 , and hence D/r_0 and Strehl ratio. Imaging binary stars of various separations as well as compact clusters such as M42 (the Trapezium in Orion) enabled us to measure the Strehl ratio at different regions in the images, and thus compare image quality at the point of co-alignment with the quality at other regions. With the use of the brightest pixel criterion such targets needed to have a single brightest star in the field.

All solar system planets out to Uranus were captured to test the suitability of frame selection for planetary imaging. Various Lunar regions were also imaged. This gave insights into the behaviour of selective shift-and-add processing where the field is filled with detail.

4.6 Summary

The *MUSIC* camera, consisting of a small video camera and a frame grabber in a LINUX PC, was used to capture sequences of FITS frames of astronomical targets on three telescopes at two different sites. Such observations of bright stars, binary and

multiple systems were used to measure the general performance of the frame selection method by imaging with a range of aperture masks, colour filters and frame exposure times. Chapter 5 describes the methods used to process the many FITS cubes, while chapters 6 and 7 detail the results from the stellar and planetary images respectively.

Chapter 5

Processing of *MUSIC* Images

5.1 Introduction

We collected 810 FITS cubes over the three observing trips, totaling 451 GB of raw stellar and planetary data. This chapter gives details of the software methodology for the frame selection processing. The image capture, calibration and frame selection software was written in the C++ language. For the automated batch processing of the many FITS cubes, these various programs were called and managed by PERL scripts. Measurements of the output star images made use of the European Southern Observatory's (ESO's) ECLIPSE package designed for FITS images (Devillard 2001).

5.2 Stellar image processing.

The calibration and initial processing of the stellar image cubes followed these steps:

1. Every frame in the cube was calibrated using the *biasflat.C* program: each pixel had the value of the same pixel in the bias frame subtracted from it, then it was divided by the pixel value from the flat-field frame. This involved a change of data type from BYTE to FLOAT in order to retain precision from the pixel arithmetic.
2. The *deint.C* program was called to de-interlace each calibrated frame. Odd and even rows were copied to separate blank frames and the gaps in each were filled by interpolation. The original frame was replaced by the two new ones, doubling the

length of the FITS cube and halving the frame exposure time. There is also a corresponding halving of pixel resolution in the y direction. This is recovered assuming a significant number of both odd row and even row frames meet the quality criteria.

3. *stackfwhm.C* created a simulated long exposure image from the FITS cube. All frames were average-combined (stacked) without selection or alignment. The FWHM of the brightest star was measured by finding the peak pixel and tracing along the orthogonal and diagonal axes until the pixel value dropped below half the peak. The FWHM was taken to be twice the average of the eight radii thus measured. The algorithm included a rejection of large outlying distances in order to account for the elongated peaks of unresolved binaries.

The frame selection processing of the stellar images was done for $FSR = 1\%$, 10% and 100% using the *combsort.C* program, and went through the following steps:

1. The FITS cube was opened and its dimensions found, then a single blank output FITS frame of the same size was created.
2. A blank array for frame quality scores was declared.
3. If the sorted array of frame numbers and quality scores had already been saved for this FITS cube, this array was written to the blank one, then the program skipped to step 6. Otherwise it continued to step 4.
4. Each frame was scanned to find the brightest pixel value and its (x, y) location. This data was written to the quality array along with the respective frame numbers.
5. The quality array was sorted in order of peak pixel value. The sorted array was saved to a text file on disc.
6. For the desired fraction of best frames (FSR), starting from the top of the sorted array, each frame was shifted to co-align the brightest pixel with that in the best frame, then the values of each pixel in the selected frames were averaged and written to the blank output image. This image was saved to disc. The algorithm eliminated spurious transient peaks such as cosmic ray hits by rejecting the “best” frame if its brightest pixel value was more than 30 greater than that in the second best frame

(which then became the best).

Measurement of the sharpness of the resulting images was done as follows;

1. The ESO's ECLIPSE *strehl* function requires input FITS images to be squares of dimensions $2^n \times 2^n$ pixels. Therefore the product images were pasted onto blank square frames using *squarify.C*.
2. The ESO's ECLIPSE *peaks* command was used to locate the stellar peaks in each output image, and the angular distances between binary and cluster stars were measured.
3. The Strehl ratio of each peak in the output image was measured using the *strehl* command.

The FWHM measured by *stackfwhm.C* was converted from pixels to arcseconds, then to radians, and used to calculate r_0 according to equation 2.10, which can be expressed as $r_0 = 0.98\lambda/\text{FWHM}$.

The ECLIPSE *peak* function works by creating a binary map of all pixel positions with values more than 2 standard deviations above the median. Peaks of less than 3×3 pixels are filtered to omit bad pixels from the count. A “floodfill” algorithm is used to find the geometric centres of the white spots in the map, weighted against pixels in the original image.

The ECLIPSE *strehl* function takes as input various parameters such as primary and secondary mirror diameters, central filter wavelength, pixel scale in arcseconds and the position of the star to be measured. It generates an ideal *PSF* for the telescope and camera configuration and calculates the peak and flux of this ideal peak. It then finds the actual peak and flux and computes the Strehl ratio using the formula

$$\text{Strehl} = \frac{(\text{star peak}/\text{star flux})}{(\text{psf peak}/\text{psf flux})}. \quad (5.1)$$

The Strehl ratios were plotted against the normalised aperture (D/r_0), frame exposure time (t) and angular distance (θ) to see the effects of these parameters on the image sharpness produced by different frame selection fractions (*FSR*). This analysis is shown in chapter 6.

5.3 Planetary image processing.

The processing of planetary images was more complicated. Frame calibration and de-interlacing was the same as for the stellar images described above except for the FWHM measurement. For its universality, the Roggeman et al S_{S1} metric defined in equation 3.7 was chosen as quality criterion. This metric uses autocorrelation to find the spectral frequency information in each frame. The program we used for frame selection and shift-and-adding was called *combfft.C*. It used cross-correlation with the best frame to compute the shift of each frame to add. The frame selection processing of calibrated planetary FITS cubes, again done for $FSR = 1\%$, 10% and 100% , ran as follows:

1. The FITS cube was opened and its dimensions read, then a single blank output FITS frame of the same size was created for the output.
2. Blank complex arrays for forward and inverse Fourier transforms were created, as well as a blank array for frame quality scores.
3. If the sorted array of frame numbers and quality scores had already been saved for this FITS cube, this array was written to the blank one, then the program skipped to step 7. Otherwise it continued to step 4.
4. The normalised autocorrelation of each frame was computed. This involved taking the Fourier transform of the frame, multiplying each element in the transform by its complex conjugate, taking the inverse Fourier transform, and dividing each array element by the highest element value.
5. The quality factor for each frame was calculated by summing all the elements in the autocorrelation more than halfway from the centre in the x and y directions, and the frame number and its score were read in to the quality array. The array was sorted in order of sharpness score, with low scores corresponding to high sharpness. The sorted array was saved to a text file on disc.
7. Starting with the second best frame as listed in the quality array, the cross-correlation of each frame with the best one was computed by multiplying its Fourier transform with the complex conjugate of the transform of the best frame.

Then the inverse transform was computed. The location of the peak in this cross-correlation provided the co-ordinates for shifting the frame to match the best frame. This was done for the desired fraction of sharp frames.

8. These sharp frames were shift-and-added.

The *fftscore.C* program could be used to measure and sort frames using the same algorithms as *combfft.C*, but without shift-and-adding frames. Thus *fftscore.C* was used to measure the sharpness of the frame-selection output images.

For comparison, some of the planetary observations were also processed by frame selection using the contrast operator given in equation 3.5, repeated here:

$$C(i, j) = | P(i, j) - P(i + 1, j + 1) | + | P(i + 1, j) - P(i, j + 1) | \quad (5.2)$$

The program to do this was named *combcont.C*. The corresponding program to measure sharpness without shift-and-adding frames was called *contscore.C*. The sharpness of the final images produced by the two methods was measured using both *fftscore.C* and *contscore.C* in order to compare the results of the two methods, and also to check the agreement of the two sharpness measurement methods. The analysis of the planetary images is contained in chapter 7.

5.4 *MUSIC* program origins and development.

A summary table of all the C++ software programs used and their object-oriented associations is contained in Appendix A. The initial *MUSIC* software programs were written by Jeremy Bailey. I modified these and wrote new code as needed.

For the stellar image processing my *combsort.C* program was based on the *combine.C* program, but I added code to handle FLOAT data, and to sort the frames and select the desired *FSR* instead of using a quality threshold. Because each FITS cube was processed for three different *FSRs* I made *combsort.C* save the sorted array of frame numbers the first time, then use the saved data on subsequent processes, instead of measuring and sorting every time. Likewise for *stackfwhm.C* I added functions to

the original *stack.C* to enable FLOAT data and measure the FWHM. I wrote *biasflat.C* for frame calibration, *combconsec.C* for averaging groups of consecutive frames, and *squarify.C* to change the frame size, based on the methods used in the other programs. In the planetary processing I added code to *combfft.C*, again for FLOAT data and to save the sorted array of frame numbers. The fast Fourier transforms were handled by the function library called *Fastest Fourier Transform in the West* version 3.1 (FFTW3) published by Frigo and Johnson (2005) of MIT. I wrote *combcont.C* and *contscore.C* with the contrast algorithm in equation 5.2 for measuring sharpness, but took the cross-correlation method of shift-and-add from *combfft.C*.

In keeping with the object-oriented programming style the following object headers were called by the various *MUSIC* programs. Both *acquire.C* and *music.C* included the class *dproc_rtd*, originally developed by Jeremy Bailey for the Anglo-Australian Observatory. *dproc_rtd* in turn included *rtdImageEvent*, developed by ESO's VLT project (Herlin et al. 1996). *dproc_rtd* contained functions to connect or disconnect to the real-time display server (rtd), send images to the rtd, handle memory allocations, and get shared memory pointers.

The class *datafile*, included by most of the *MUSIC* programs, provided manipulations such as opening, creation, closing, reading data from and writing data to, and finding properties of, FITS files. It was based on *iris2datafile* created by Shortridge et al. (2004) for use with the IRIS2 imager on the AAT, then modified by Jeremy Bailey for use with *MUSIC*. I added functions to the class to enable combined read/write access, handle FLOAT data and find the image data type, and renamed it. *datafile* uses the *cfitsio* library package, maintained by William D. Pence (1999) at NASA Goddard Space Flight Centre.

5.5 Summary

The *MUSIC* software was used to capture FITS cubes using a frame grabber. Post-processing involved calibrating and de-interlacing the frames, then measuring and ranking the frames for sharpness, and shift-and-adding the desired fraction of the best

frames. The stellar images thus produced were analysed by locating stars and then measuring their Strehl ratios. The Strehl ratios produced by various *FSRs* were plotted against the various parameters to examine their effects on image sharpness, and also compared with simulated long exposure images produced by stacking all the frames. This was done to empirically test the frame selection method in the simplest possible way. The results from the stellar observations are detailed in the next chapter.

Planetary and lunar observations were processed using an autocorrelation score as the sharpness metric, and frame co-alignment was done using cross-correlation. Some of the images thus produced were compared with results from the use of a contrast operator metric. These results are contained in chapter 7.

Chapter 6

Analysis of Stellar Images

6.1 Introduction

A list of the stellar objects that were imaged is in appendix B, and the observing log is contained in appendix C. The stellar observations were processed as described in chapter 5. A small fraction of the observations produced blatantly spurious results. For example, some FITS cubes showed transient hot pixels that affected the astrometric measurements as well as the shift-and-add process. Some binaries of similar magnitude also showed incorrect shift-and-add. These examples are discussed in section 6.4.

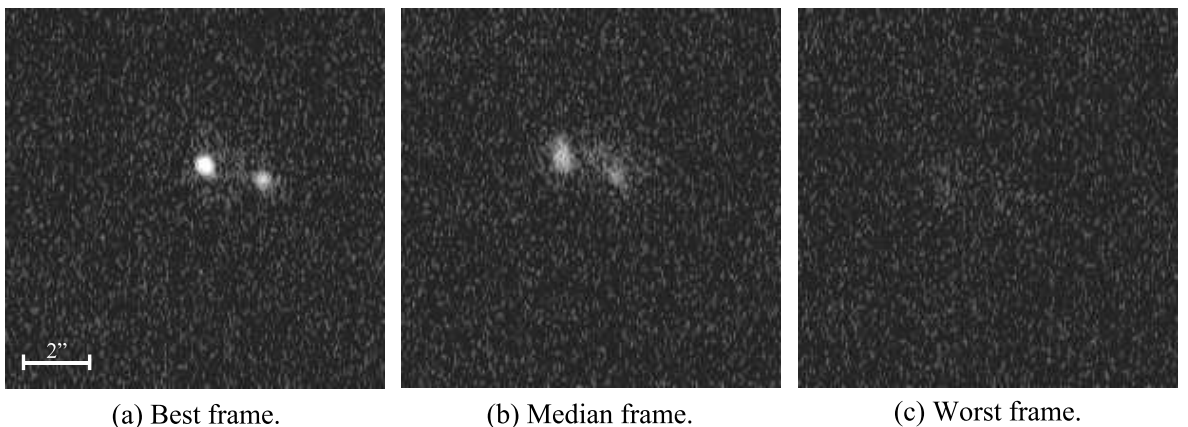


FIGURE 6.1: Individual frames from an observation of the binary τ Ophiuchi that were ranked as best, worst and median according to the brightest pixel critereon. Images are diplyed with logarithmic pixel scale.

Occasionally when fainter stars were imaged during very high winds the maximum camera gain convolved with the blurring to make the images too noisy to detect the stars even in the best frames. Images that suffered these problems were culled from the analysis. It should be noted that the images presented in this chapter and the next were chosen not because they are necessarily excellent images. They were chosen because they demonstrate the effectiveness or some other aspect of the frame selection method compared with uncompensated long-exposure imaging, in the conditions that prevailed during our observing trips.

Frame selection was carried out on FITS cubes of star images using the brightest pixel value (Muller and Buffington's S_2 metric) as the quality criterion for ranking the frames. Several binaries and a cluster were also imaged in order to see how shift-and-adding frames affects the sharpness across the field. The quality of all the processed star images was determined by measuring the Strehl ratio as described in section 5.2. The Strehl ratios of the stellar peaks were plotted against the different frame selection parameters. Key results contained in this chapter were published in *Monthly Notices of the Royal Astronomical Society* (Smith et al. 2009).

6.2 Stellar Image Results.

Figure 6.1 shows the frames from a FITS cube that were ranked respectively as best, median and worst. In the best frame the two peaks are distinct, compact and well correlated. The median frame has the peaks in a different position but approximately the same separation, demonstrating the effect of tilt, and the speckle patterns of the peaks are not correlated. In the worst frame the peaks are almost indistinguishable from the noise. This shows the effectiveness of the peak pixel quality criterion in ranking the frames for this type of image. Note that the images are shown with logarithmic pixel scale for clarity.

6.2.1 Frame selection rate FSR

Figure 6.2 shows a set of images of the binary system τ Ophuchii.

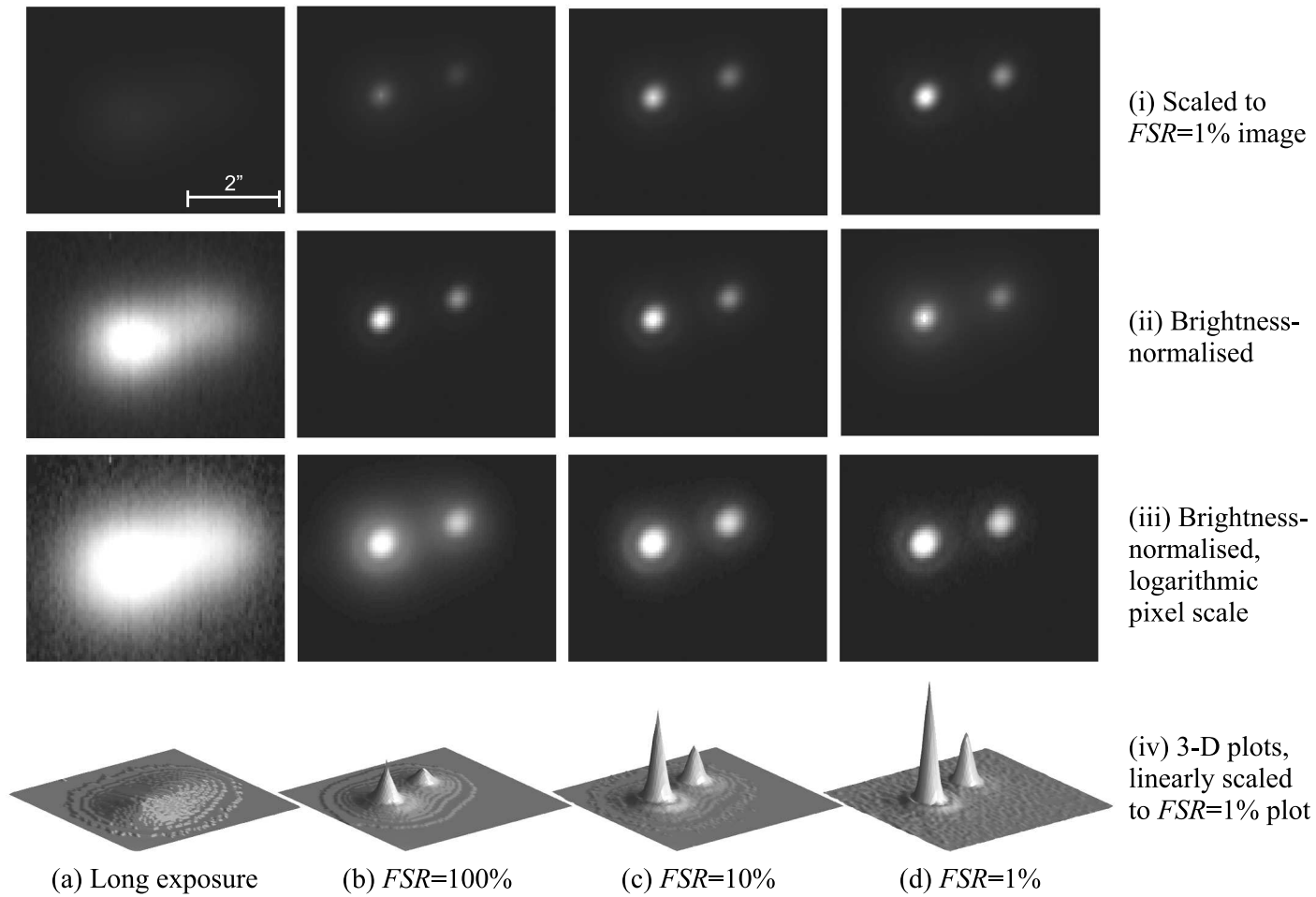


FIGURE 6.2: Images of binary τ Ophiuchi, $1.7''$ separation. Columns show different FSR . The rows show different pixel scaling to highlight different features. The images were taken on the AAT, $D=40$ cm aperture mask, $\lambda=700$ nm (red filter) and $t=8.3$ ms frame exposure time.

Each column represents a particular FSR , and shows the same image with different pixel scales in order to highlight different features. The images in row (i) and the 3 dimensional plots in row (iv) show the greater peak brightness with lower FSR . Row (ii) displays the images with normalised brightness (i.e. all pixel values are divided by the highest value, and are then displayed in the range of 0 to 1) and shows how the PSF reduces in size with frame selection. In the stacked image the binary is unresolved. When all the frames are shift-and-added the binary is easily resolved with a measured separation of 1.7 ± 0.1 arcseconds averaged from all of our observations, which is close to the catalogue value of 1.7 arcseconds (see appendix B. Each star shows a bright central peak with a significant halo, resembling the tilt corrected PSF shown in figure 2.3.

The $FSR=10\%$ and $FSR=1\%$ pictures show successively narrower central peaks, corresponding to increasing resolution. Row (iii) shows the images brightness-normalised and with logarithmic pixel scale in order to highlight the halo around each peak. The halo can be seen to diminish with increasing selectivity since more flux is in the central peak. In the $FSR=1\%$ image a dark ring is visible at a radius of 8 pixels around each peak, matching the Rayleigh criterion for a diffraction limited image. The primary peak in this image has a Strehl ratio of 0.799. This is among our best results and more than twice that achieved in other lucky imaging studies.

An example of the usefulness of frame selection is in the resolution of faint stellar companions, as demonstrated by Law et al. (2005) among others. Figure 6.3 of ζ Orionis (Alnitak) shows that although pure shift-and-add ($FRS = 100\%$) reveals the faint companion ζ Orionis B visually, it is still poorly resolved, being in the halo of ζ Orionis A. With frame selection the halo is reduced and the companion is well resolved. There are also dark rings and faint spikes on the primary star, again consistent with a diffraction limited image. Our measured separation of 2.5 ± 0.1 arcseconds compares well with the published value of 2.4 arcseconds.

The improvement in image sharpness with decreasing FSR is shown to be a general trend in figures 6.4 and 6.5, which are broken down into the different frame selection rates.

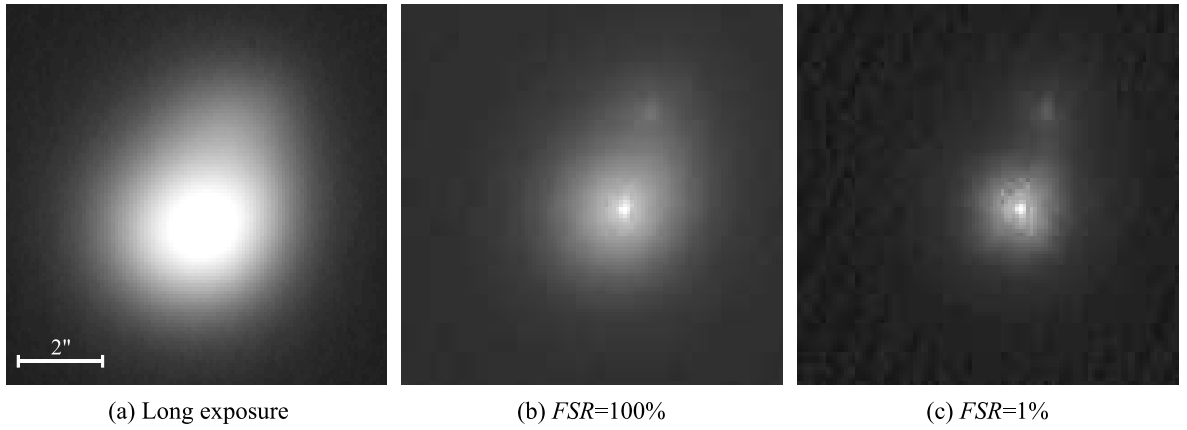


FIGURE 6.3: Images of binary ζ Orionis (Alnitak, $2.5''$ separation) produced by different FSR , displayed brightness normalised and logarithmic scale. The images were taken on the ANU 1m telescope, $D=75$ cm aperture mask with $2.5\times$ focal reducer, $t=8.3$ ms, $\lambda=800$ nm (infrared filter).

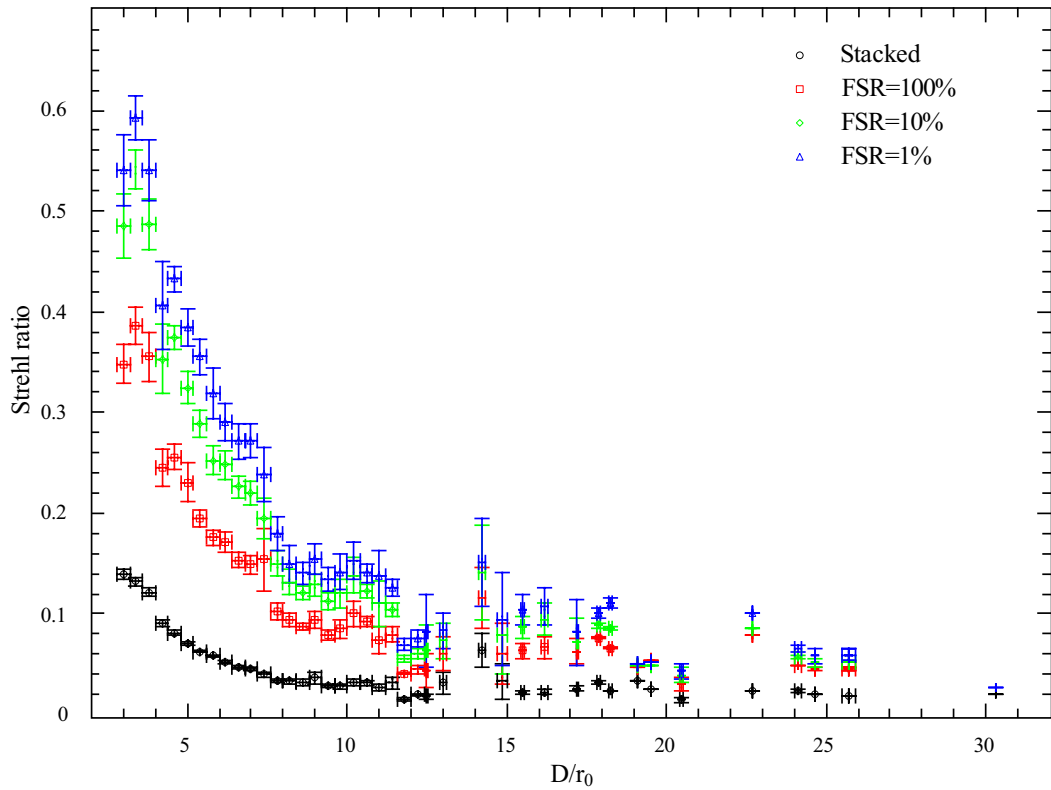


FIGURE 6.4: Strehl ratio versus D/r_0 for stellar images binned in D/r_0 .

6.2.2 Seeing-normalised aperture D/r_0

Over all of our observations r_0 ranged from 1 to 12 cm, and D/r_0 from 2.8 to 30.3. Figure 6.4 plots Strehl ratios of stellar peaks versus D/r_0 , with the scatter points binned in D/r_0 . The horizontal error bars represent the bin widths, and the vertical error bars are the standard errors of the sample in each bin. The obvious trend is for higher Strehl ratios at low D/r_0 . For example, the image cube from which figures 6.1 and 6.2 were compiled had an average $r_0=11.5$ cm, giving $D/r_0 = 3.5$. Low D/r_0 is achieved in good seeing (large r_0) and/or with smaller apertures (small D). In these conditions there are not only more good frames to choose from (equation 3.1) but the average frame quality is better, as indicated by the higher Strehl ratios of the long exposure images at low D/r_0 . This result makes frame selection most suitable for use with small to medium sized telescopes. This does, however, limit the magnitudes of usable target objects or guide stars. The trends of the frame selected data are not as smooth as that of the long exposure data. This is because frame selected images are more susceptible than long exposures to variations in exposure time and colour filter, as well as atmospheric dispersion that elongates images taken at large zenith angles (see section 6.4.1). At $D/r_0 > 12$ the Strehl ratios decrease more slowly. The trends in this region are less smooth and some of the error bars are larger because of smaller statistical samples.

The improvement in image quality is indicated by the gain in Strehl ratio; that is, the Strehl ratio of a frame selected image divided by that of the long exposure image derived from the same cube. Figure 6.5 shows the bin-averaged improvement factors versus D/r_0 . It compares the improvement made by pure shift-and-add (100%FSR) with that from 1%FSR. The 1%FSR points are consistently higher than those for 100%FSR, confirming the advantage of being more selective. The 1%FSR images show improvement factors greater than 5 for D/r_0 between 4.5 and 7.8, with a small peak at $D/r_0 \sim 7$. This represents the best compromise between diffraction-limited resolution, which improves with increasing D , and seeing-limited resolution that improves with increasing r_0 , with an acceptable probability of good frames of around 1 in 370. For larger D/r_0 , the difference in improvement factor between $FSR = 100\%$ and

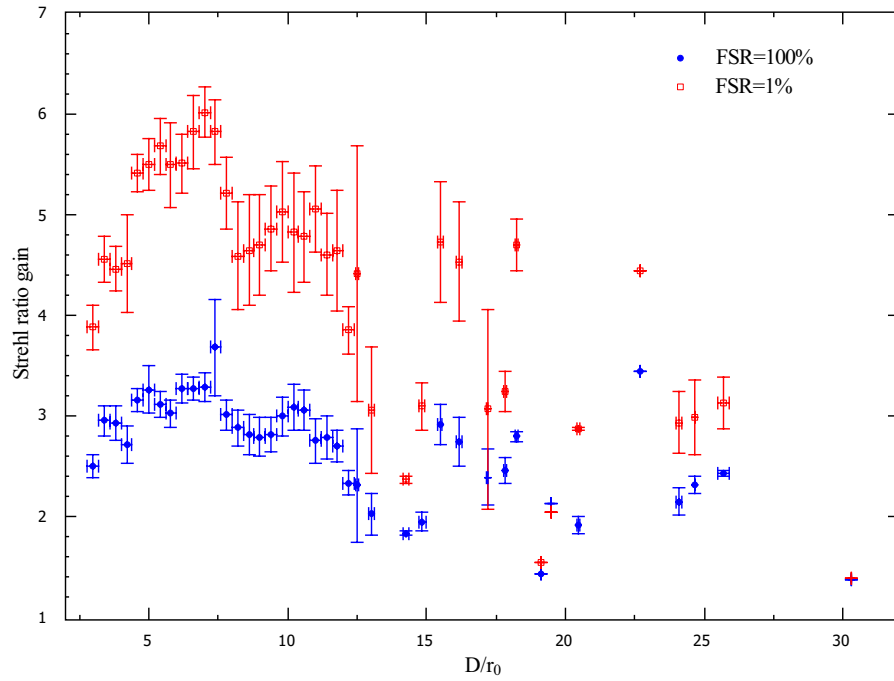


FIGURE 6.5: As for figure 6.4, but plotting the improvement in Strehl ratio compared with the long exposure image for each bin of D/r_0 .

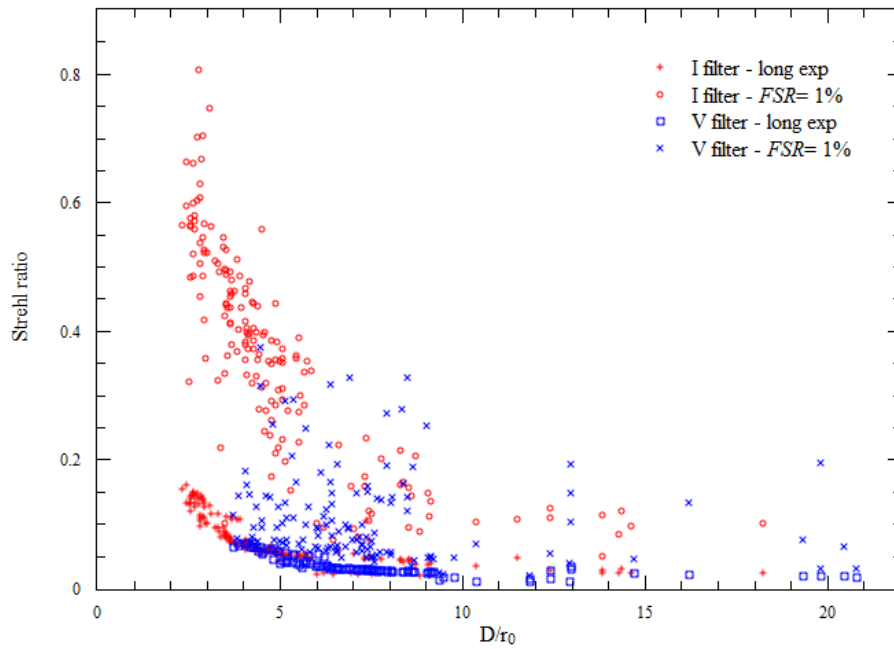


FIGURE 6.6: Strehl ratio versus D/r_0 for infrared and visual bands, long exposure and $FSR = 1\%$.

$FSR = 1\%$ seems to decrease. The error bars appear large because of the cumulative variances of the frame selected data and the stacked data. The largest error bars are, again, due to small sample sizes.

6.2.3 Colour band λ

Because $r_0 \propto \lambda^{6/5}$ it was expected that the Strehl ratio would improve at longer wavelengths. Figure 6.6 shows that the Strehl ratios are generally higher for infrared images than for those taken in the visual band. Also, the range of D/r_0 for observations in the visual band is higher than for the infrared band. The trends are the same as in figure 6.4, indicating that the better performance in the infrared is due to the lower range of D/r_0 , giving better average frame quality than in other bands. This produces higher average Strehl ratios in the long exposures, and hence also in the frame selected images. Atmospheric dispersion has a greater effect at short wavelengths, so the frame selected data in the visual band shows broader scatter. A smaller amount of data collected for the B and R bands were also consistent with these trends.

6.2.4 Frame exposure time t

The exposure times used for our observations (after deinterlacing) were 1, 2, 4, 8.3 and 20 ms. To test longer exposures additional runs of 40, 80, 160, 320 and 640 ms were created by combining groups of 2, 4, 6, 8 and 16 consecutive frames respectively from the 20 ms runs. These simulated runs thus had fewer frames to choose from, and so the resulting images have lower SNR than those from the original runs. The top panel of figure 6.7 shows Strehl ratios against exposure times for $1\%FSR$, with the data binned into four ranges of D/r_0 .

For all normalised apertures the Strehl ratios are consistently higher for shorter frame exposures. The bottom panel plots the improvement in Strehl ratio over the stacked images. Even at the longest times tested the Strehl ratios improved by a factor of around 2 for all D/r_0 . Shorter times gave greater improvement, but the trends are less steep for $t < 10$ ms, especially for large D/r_0 . Hence we find that, although

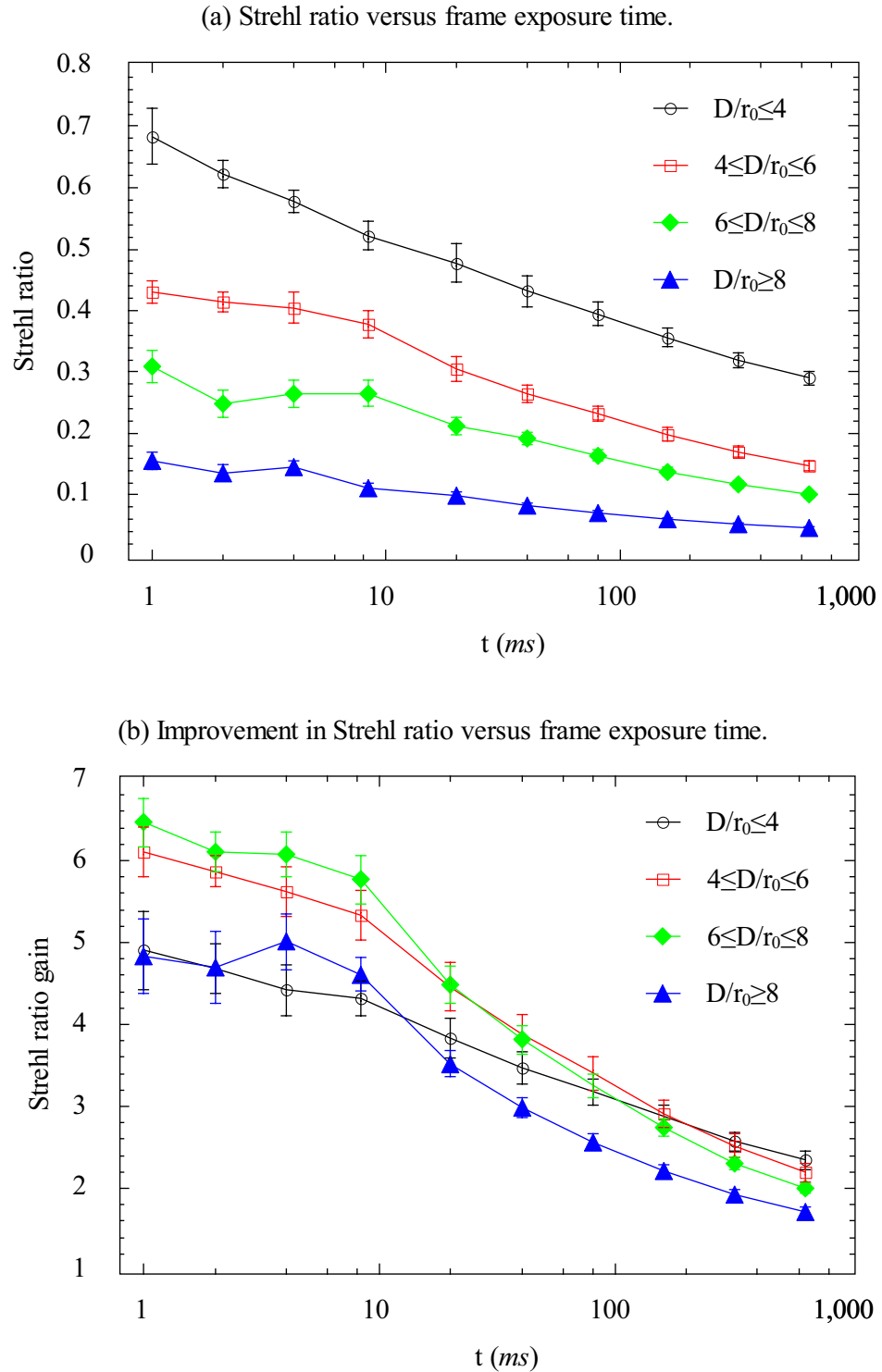


FIGURE 6.7: (a) Strehl ratio and (b) Strehl improvement factor for data processed by selection and alignment of the best 1% of frames as a function of exposure time. The data is binned into four different ranges of D/r_0

TABLE 6.1: Strehl ratios of peaks in images of α Centauri in figure 6.8.

Peak	Frame Selection Rate			
	Long Exp.	100%	10%	1%
Primary	0.025	0.055	0.080	0.091
Secondary	0.028	0.037	0.049	0.057
Normalised	1.12	0.67	0.61	0.62

selective imaging gives improved image quality for any reasonably short exposure time, for the Siding Spring site if the target is sufficiently bright t should be limited to 10 ms. At sites with better seeing, longer exposures will be acceptable, enabling fainter targets to be imaged.

6.2.5 Strehl ratio versus angular distance θ

The average size of r_0 during an observation has an effect on the sharpness across the field of view of a shift-and-added image. Even frames with high overall sharpness may not be isoplanatic. By co-aligning the frames on the brightest pixels the sharpness of this spot is artificially enhanced. Other peaks may have a different tilt and speckle pattern. Shift-and-adding may still improve the sharpness of these features, but to a lesser extent than the primary peak, as seen in figure 6.8 and table 6.1.

Figure 6.8 shows the binary α Centauri with a separation of 10.2 ± 0.1 arcseconds. It is noticeable in the 3 dimensional plots that although the secondary peak does grow with decreasing FSR , it does not do so in direct proportion to the primary peak. The measured Strehl ratios for both peaks in each picture are listed in table 6.1. Note that the Strehl ratios are small simply because of the large D/r_0 of 17 for this observation. In the long exposure image the Strehl ratios of the two peaks are, as expected, approximately equal. In each of the frame selected images, the Strehl ratio of the secondary peak is higher than that in the long exposure, but in all cases is less than 70% of the corresponding primary peak. This ratio, the Strehl ratio of a secondary peak divided by that of the primary peak in the same image, I define as the normalised

Strehl ratio. Figure 6.9 plots

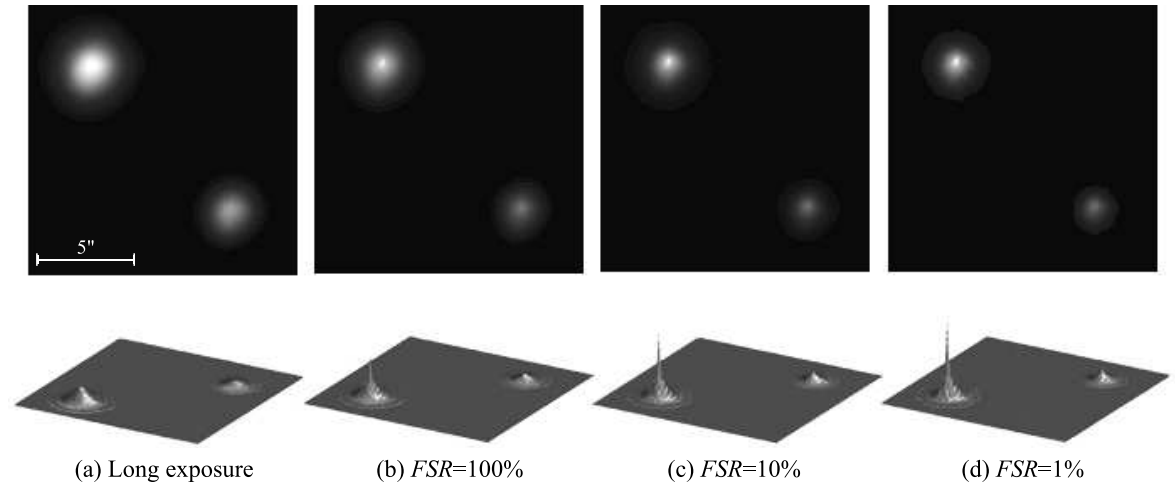


FIGURE 6.8: Binary system α Centauri, $11''$ separation. Images are brightness-normalised and logarithmic pixel scale. The 3-dimensional plots are linear scale. Images were taken on the ANU 1m telescope, $D = 75\text{ cm}$ aperture mask with $2.5\times$ focal reducer, $t = 1\text{ ms}$, $\lambda = 550\text{ nm}$ (visual filter).

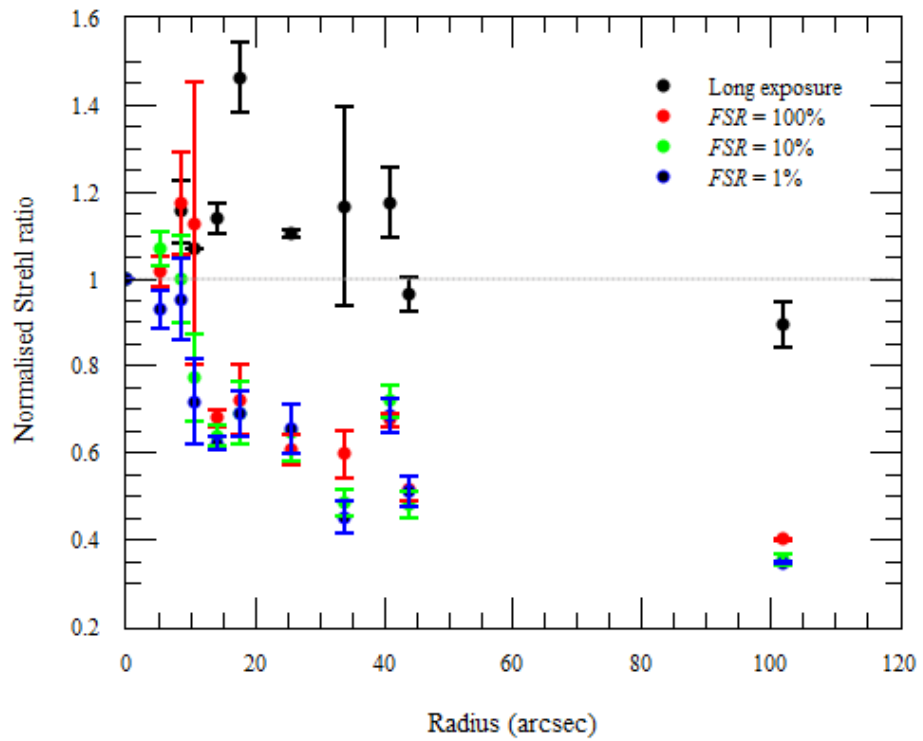


FIGURE 6.9: Graph of normalised Strehl ratio versus radius for long exposures, $FSR = 100\%$, 10% and 1% .

normalised Strehl ratio against angular distance (radius) for the different FSR values used, and figure 6.10 for high D/r_0 (> 6) and low D/r_0 (≤ 6) for all binaries and clusters that we imaged. Our data shows a general trend to diminishing Strehl ratio and less Strehl improvement with increasing angular distance from the alignment location. This trend seems to be largely independent of FSR and D/r_0 . This is in qualitative agreement with the simulations by Baldwin et al. (2008), though a direct quantitative comparison is not possible. Both figures 6.10 and 6.9 show, on average, that the normalised Strehl ratio drops sharply to around 0.6 at 15 arcseconds, then more slowly to around 0.4 at 100 arcseconds. However, in all of our observations the secondary peaks showed improvement with frame selection. Even over angular separations as large as 100 arcseconds an improvement factor of around 3 was seen with $FSR = 1\%$.

6.3 *MUSIC* data compared with other studies

The scatter data of our individual long exposure and $1\%FSR$ images is displayed in figure 6.11 compared with results from other experiments. The scatter of the *MUSIC* data can again be explained by the range of frame exposure times and colour filters used, as well as by atmospheric dispersion. Of the many experiments done in selective imaging, few of the results have been presented in a way that included D/r_0 and Strehl ratio, or that enabled them to be derived. The black line indicating the simulations of *LuckyCam* by Baldwin et al. (2008) follows the same trend as our data at the upper edge of our scatter. Their slightly higher Strehl ratios in its range of D/r_0 are due to two factors. The first is that they modelled the particular scenario of imaging with a low noise ECCD in the good seeing quality found at the La Palma site of the Nordic Optical Telescope. Our *MUSIC* data was acquired using an inexpensive, relatively noisy camera at two different sites with worse seeing on average than La Palma, so the raw image frames will have been, on average, of a lower quality. The second, more significant reason is that the simulations assumed perfect diffraction limited telescope optics. In this regime the best quality frames are those in which atmospheric turbulence is at a minimum. On real telescopes with aberrations the

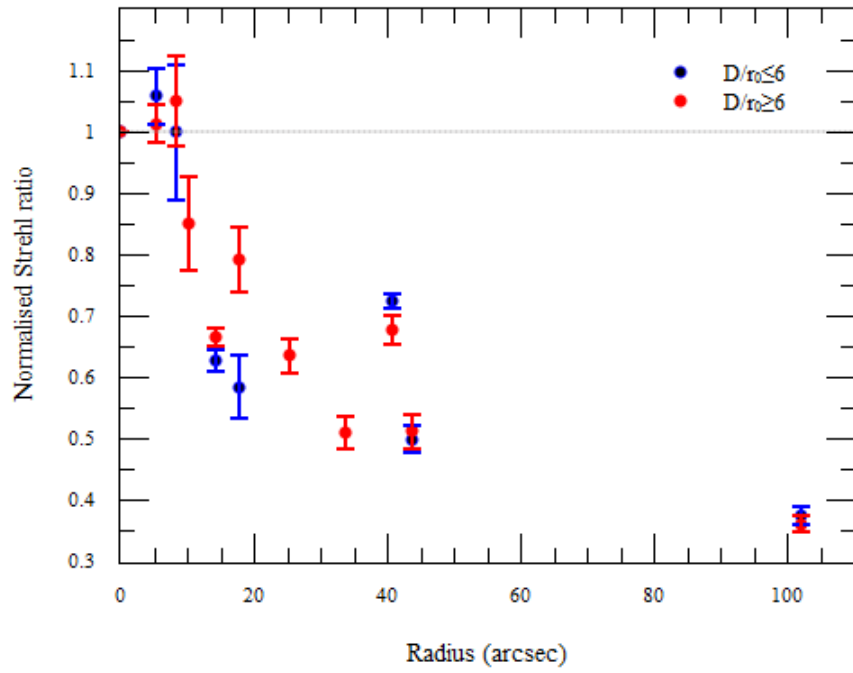


FIGURE 6.10: Graph of normalised Strehl ratio versus radius for $D/r_0 \leq 6$ and $D/r_0 > 6$.

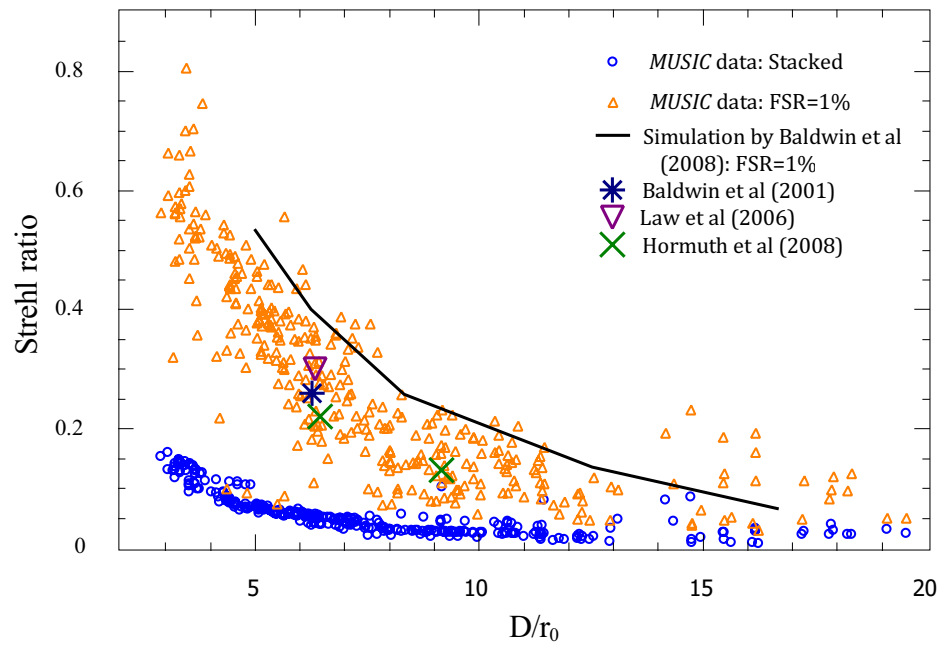


FIGURE 6.11: Strehl ratio versus D/r_0 , for all stellar images where $D/r_0 < 20$. *MUSIC* data is shown for $FSR = 100\%$ (orange triangles) and for long exposures (blue circles). Other data points are sourced from other studies as referenced in the legend.

sharpest frames are those in which the atmospheric aberrations cancel those of the optical system. In this “very lucky observer” regime there will be fewer frames meeting the quality threshold (Beckers and Rimmele 1996). Other data points were derived from sources, listed in the legend, where D/r_0 could be calculated from given apertures and seeing FWHM. These observational data points are quite consistent with the *MUSIC* scatter data.

It can be seen that the *MUSIC* observations cover a much wider range of D/r_0 than the other studies. This was done in two ways. Firstly, we observed in whatever conditions prevailed rather than waiting for good seeing, and so many of our observing runs were made with very small r_0 and hence large D/r_0 . Secondly we used various aperture masks ranging down to 10 cm, giving very small D/r_0 . It can be seen that Strehl ratios as high as 0.8 were achieved at $D/r_0 \sim 2.8$, even with imperfect optics. Although the models of Baldwin et al predict a Strehl ratio of 5.3 at $D/r_0 \sim 5.5$, the highest previously achieved in stellar observations has been ~ 0.3 .

6.4 Limitation of the brightest pixel criterion

Our use of the brightest pixel (S_2) as quality measure was purely for its simplicity. It was never imagined, however, to be the best criterion for use with all stellar images. This section discusses the problems we encountered, including those in some way attributable to the use of this metric. The results obtained from the brightest pixel metric are also briefly compared to those of the S_{S1} that uses Fourier analysis, suitable for images of extended objects.

6.4.1 Atmospheric Dispersion

The refraction of the atmosphere produces chromatic dispersion at large zenith angles. This makes star images taken at such elevations through broad band-pass filters elongated. For this dispersion effect to be reduced by frame selection there would have to be moments when the turbulence happened to counteract not only any telescope

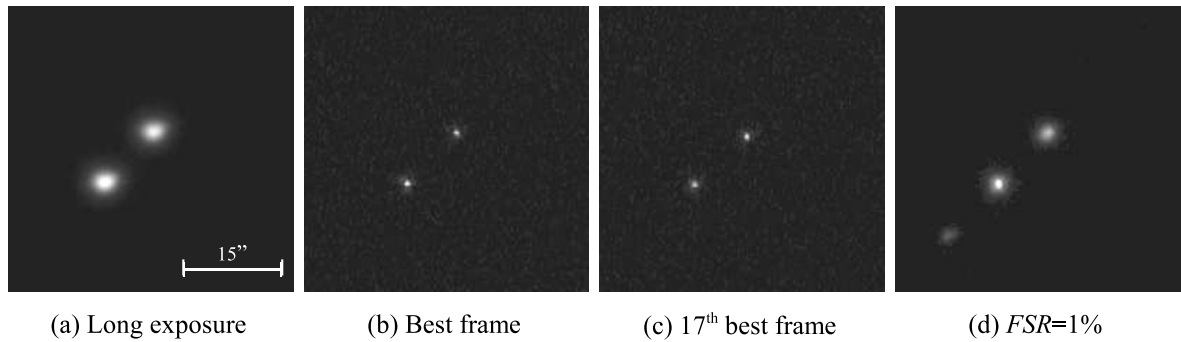


FIGURE 6.12: Binary stars k2 (lower left) and k1 (upper right) Puppis, $9.9''$ separation, magnitudes 4.5 and 4.7 respectively. Images (a), (b) and (c) are linear scale, (d) is logarithmic scale to highlight the faint spurious peak. All are brightness normalised. Images were taken on the ANU 1m telescope, $D = 30\text{ cm}$ aperture mask, $t = 8.3\text{ ms}$, $\lambda = 800\text{ nm}$ (infrared filter).

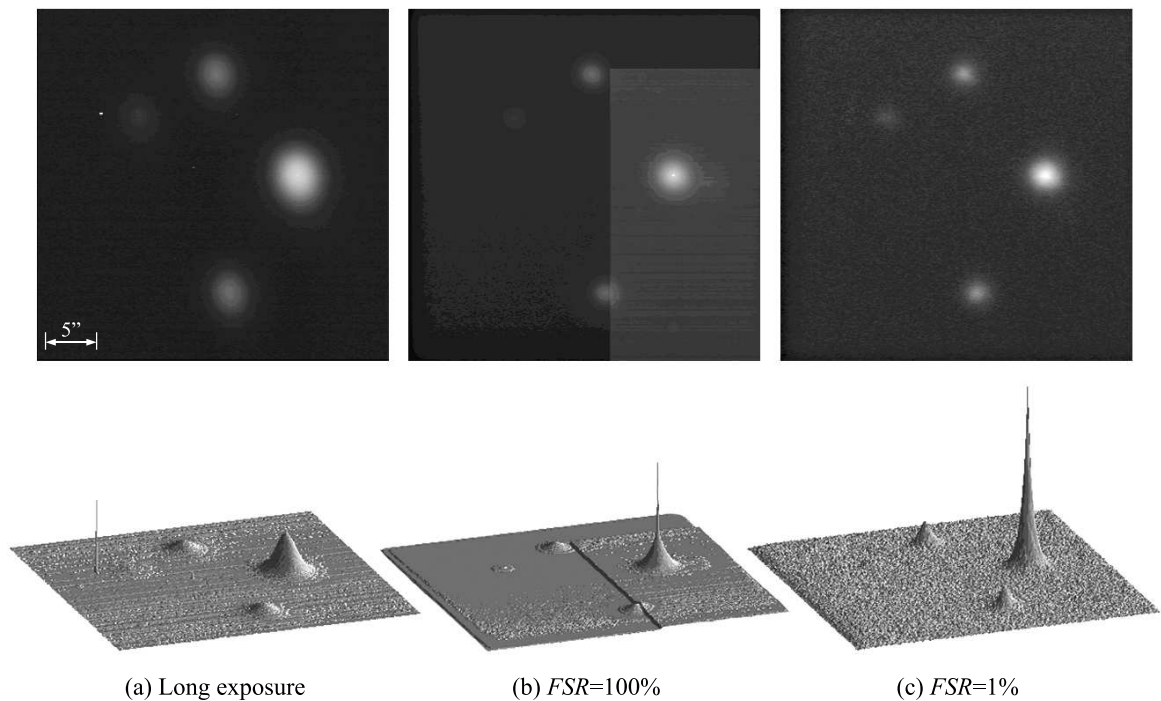


FIGURE 6.13: Images, displayed logarithmic scale and brightness normalised, and linear 3-D plots of the Trapezium cluster in M42 in Orion, showing the effects of a hot pixel on frame selection. Images were taken on the ANU 1m telescope, $D = 75\text{ cm}$ aperture mask with $2.5\times$ focal reducer, $t = 20\text{ ms}$, $\lambda = 440\text{ nm}$ (blue filter).

aberrations (Beckers' and Rimmele's very lucky observer mode) but also the curvature of the atmosphere. We might call this the very *very* lucky observer mode. Our frame selected images taken in this situation still showed elongation. Thus, dispersion correction should be utilised if available.

6.4.2 Small magnitude differences in binaries and multiples

For any field with a single bright star the results were an increase in Strehl ratio, and so of image sharpness, with decreasing FSR or increasing quality threshold. However, it was realised beforehand that the technique would not suit fields where there is only a small magnitude difference between the brightest stars in the field. In such cases there may be instances when the speckle patterns of the different peaks are uncorrelated and a secondary peak may be momentarily brighter than the primary. When this happens the frame will be shifted such that the wrong peaks are co-aligned. The result is the creation of spurious peaks, and the relative brightnesses of the real peaks are incorrect. An example of this occurrence is shown in figure 6.12. The two stars k1 and k2 Puppis are almost equal magnitudes, 4.5 and 4.7 respectively. k2 is slightly brighter, and is the lower left star in 6.12(a), (b) and (c). Figure 6.12(b) shows frame number 7576 (out of 10000 de-interlaced frames) which was ranked the sharpest. It shows k2 as slightly brighter than k1. Figure 6.12(c) shows frame number 3882, which was ranked the 17th sharpest, that instead shows k2 as slightly fainter than k1. The speckle patterns of the two peaks, although compact, are poorly correlated, meaning that they are momentarily in different isoplanatic patches. There were 11 such frames in the best 100 frames (1% of the total), and 2375 in the whole run of 10000. With shift-and-add processing these frames were aligned such that k1 coincided with k2 in the best frame, artificially increasing k2's image brightness. This placed k2 from these frames at the lower left, creating a spurious third peak. In many cases these spurious peaks are faint and so easily overlooked. It is possible for the peaks in these suspect frames to be shifted out of the picture. Such cases are very difficult to detect by visual inspection alone.

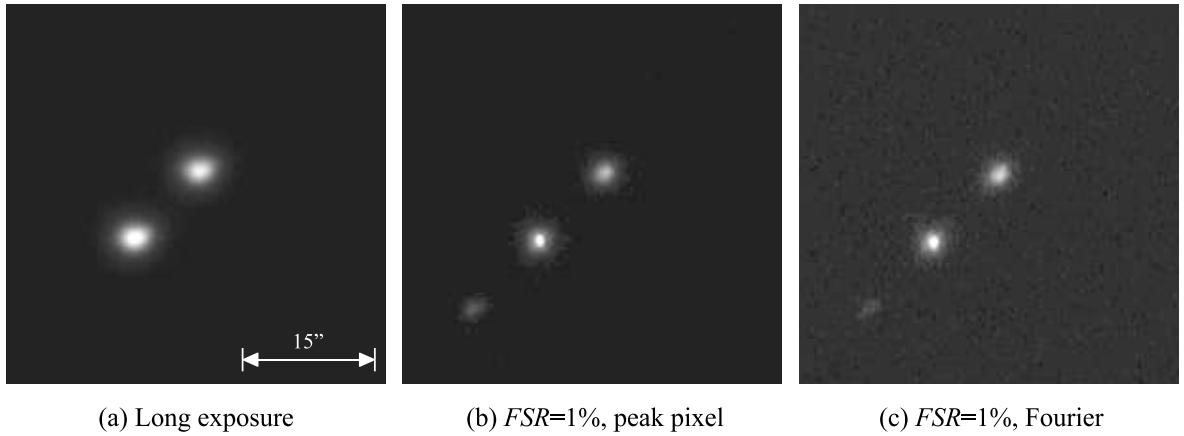


FIGURE 6.14: Images of binary kPuppis, comparing the 1% frame selected images produced using the peak-pixel algorithm with that from the S_{S1} metric and the long exposure image.

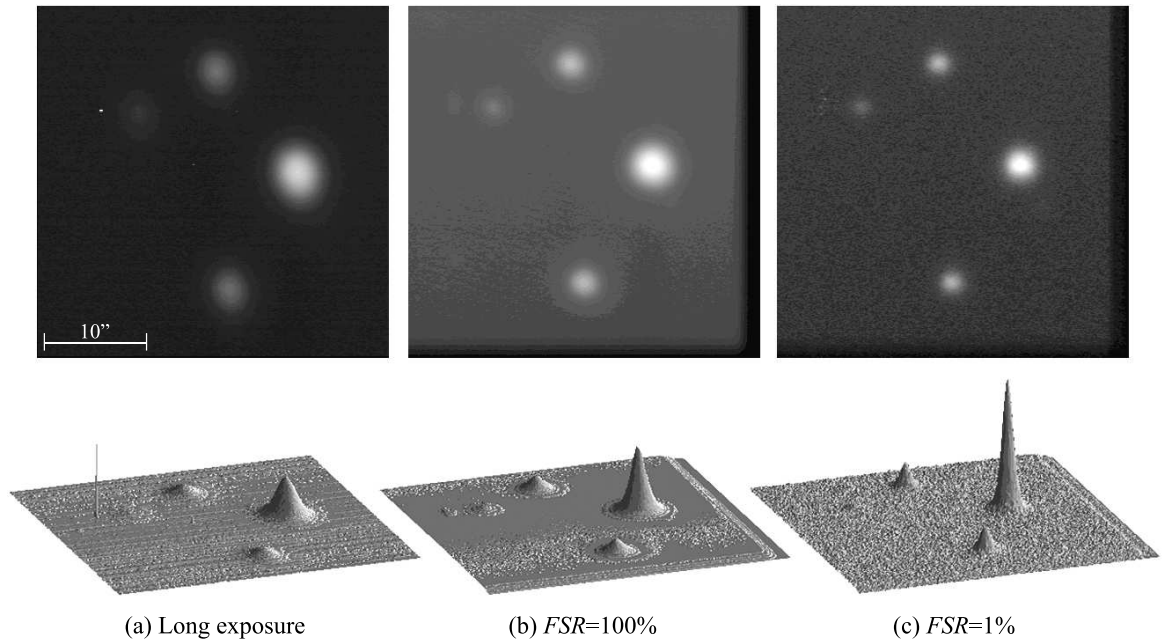


FIGURE 6.15: Images and 3-D plots of the Trapezium, from the same FITS cube as in 6.13, but frame selected using Fourier methods.

6.4.3 Hot pixels

Another problem that was encountered was a transient hot-pixel in one of the cameras. Since it varied in brightness over time, even during individual observations, it was not fully resolved by bias correction. In frames where the hot pixel was brighter than the brightest star, the shift-and-add processing moved that frame to add the hot pixel

to the star. Again this can produce spurious peaks in the final image and shift flux from other peaks out of the image. In the particular case shown in figure 6.13(b), this occurred in many frames producing the spike at the brightest star, even though 6.13(c) shows that at its brightest the brightest star exceeded the hot-pixel in the best 1% of frames. Of course, for research purposes, the frames would have been scanned with a hot-pixel correction algorithm prior to frame selection.

6.4.4 Comparison of the peak-pixel and S_{S1} metrics

Tests were done to compare the peak-pixel frame selection algorithm with the Roggemann et al. (1994) S_{S1} metric that we used for the planetary images. S_{S1} uses Fourier methods and is more suited to extended objects. In processing the same image sequence of kPuppis shown in figure 6.12, it was surprising to see that the spurious 3rd peak was not eliminated, although it was diminished (see figure 6.14).

When the Fourier method was tried with the same Trapezium FITS cube as in figure 6.13, it improved the Strehl ratios of the main stars and smeared out the hot-pixel so that it merged in to the background noise (see figure 6.15). Interestingly the improvement in Strehl ratios of the minor stars diminished with distance from the brightest, just as with the peak-pixel method. This is probably because the cross-correlations will usually be strongest near the brightest star, and so the brightest stars will often be co-aligned, as they were in the peak-pixel method. This may not be the case for fields with no single brightest star.

Another example of Trapezium images, shown in figure 6.16, was taken in very bad seeing. The extreme blurring made the video output very faint, so the camera was used at maximum gain. This resulted in extremely noisy frames, and frame selection by the S_{S1} metric actually showed a reduction of the star peaks with decreasing FSR , which is the reverse of usual trend. This is because moments of extreme speckling, as well as the high noise, are seen in the autocorrelations as having strong high spatial frequencies, and the algorithm ranks these highly. In this case, therefore, the peak-pixel algorithm was clearly superior, as shown in figure 6.17.

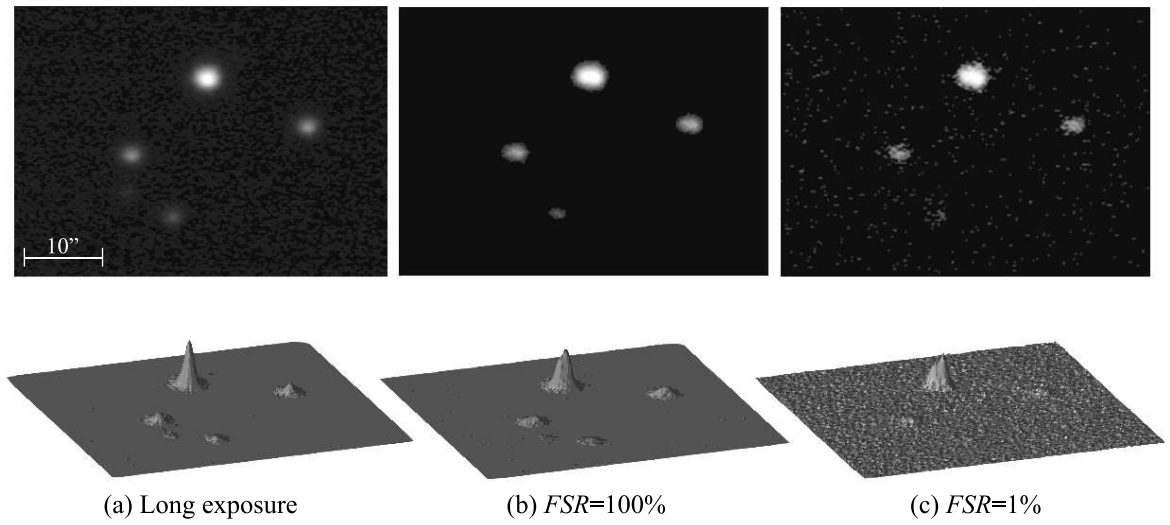


FIGURE 6.16: Images and 3-D plots of the Trapezium taken in extremely bad seeing, frame selected using Fourier methods. The images are brightness-normalised.

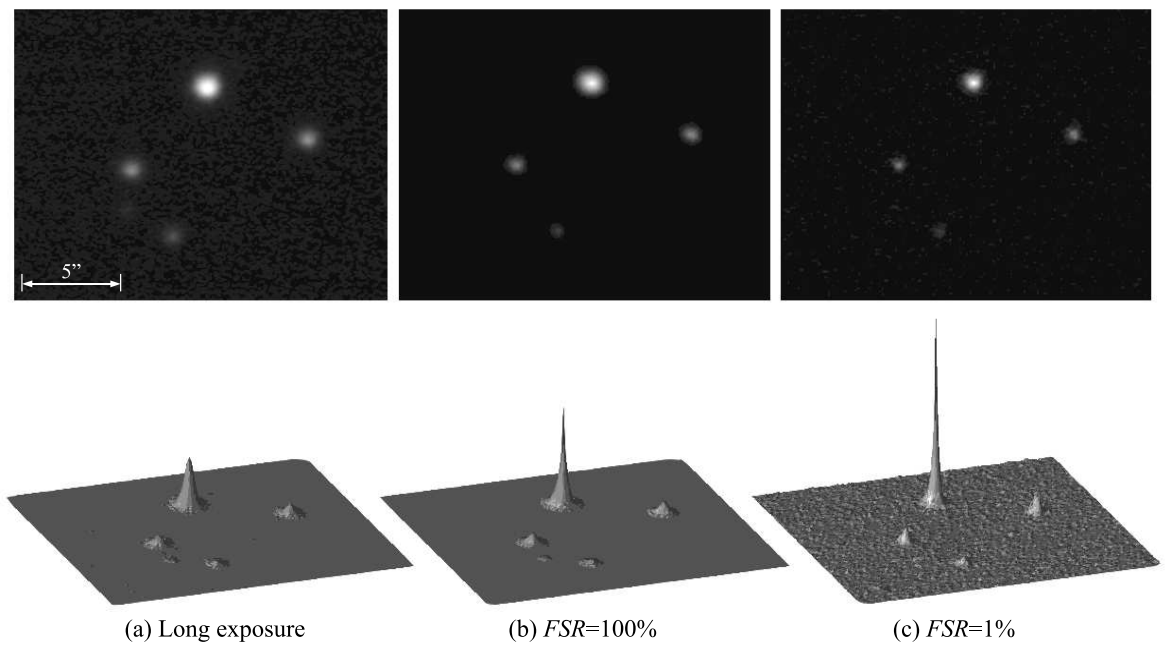


FIGURE 6.17: Images and 3-D plots of the Trapezium taken in extremely bad seeing, frame selected using the peak-pixel method. The images are brightness-normalised.

6.5 Summary

The use of the brightest pixel metric enabled the frame selection method to be examined in the simplest possible way. We used the *MUSIC* camera to image many bright stars, binaries and multiple systems, using a range of aperture masks, frame exposure times and colour filters. The FITS cubes were post-processed with different frame selection fractions, and also by stacking. Thus we performed the most wide-ranging empirical study of the performance of the frame selection method possible. Our results were consistent with previous theoretical and experimental studies, but more thoroughly explored the parameter space.

It was found that the sharpness of frame selected images depended crucially on D/r_0 . The use of small apertures, as well as occasions of fair seeing, gave small values of D/r_0 . This enabled Strehl ratios as high as 0.8 to be attained at $D/r_0 \sim 2.8$. This is competitive with high-order adaptive optics, but was achieved with a fraction of the cost and complexity of hardware. The highest Strehl ratio previously achieved in frame selection observations has been ~ 0.3 . Strehl ratio improvement was produced with frame selection over long exposures at all D/r_0 , but the greatest gain was found when $D/r_0 < 12$. The highest gain factor achieved was 6 at $D/r_0 \sim 7$ and $FSR = 1\%$, but this peak was only small. The gain was greater than 5 for D/r_0 between 4.5 and 8.

Improvement in image sharpness was gained with all reasonably short frame exposure times, even as long as 0.64 s. The improvement was found to be greater the shorter the exposure. The improvement began to level out at ~ 10 ms, so based on our observations this is the optimum exposure time for the Siding Spring site.

Frame selection produced a gain in Strehl ratios at all wavelengths, but, as predicted, the most favourable results were found in the infrared because of the larger values of r_0 . So frame selection is particularly suited to astrophysical and planetary atmospheric and mineralogy applications that are imaged at long wavelengths.

Image sharpness, as measured by Strehl ratio, was found to diminish with distance from the brightest star. This was unsurprising when using the peak-pixel metric since

the brightest star becomes artificially enhanced. A small number of tests with the S_{S1} metric, however produced the same result. The normalised Strehl ratio was found on average to reduce quickly to around 0.6 at 15 arcseconds. After this the curve levelled off somewhat, dropping to around 0.4 at around 100 arcseconds. This effect seems to be independent of both D/r_0 and FSR .

The next chapter contains the analysis of the planetary images.

Chapter 7

Analysis of Planetary Images

7.1 Introduction

In chapter 6 we examined the behaviour of frame selection with regard to the imaging parameters, and showed its effectiveness in sharpening turbulence-degraded images. We plan to use the technique for surveys of planetary atmospheres and mineralogy, so this chapter presents the results of our experimental observations of the Moon and solar system planets using *MUSIC*. Again, the images included in this chapter were chosen because they show some feature of the frame selection method as applied to extended objects, and are not presented necessarily as excellent images. In addition, the effectiveness of selective imaging when used for transient events such as a Jovian

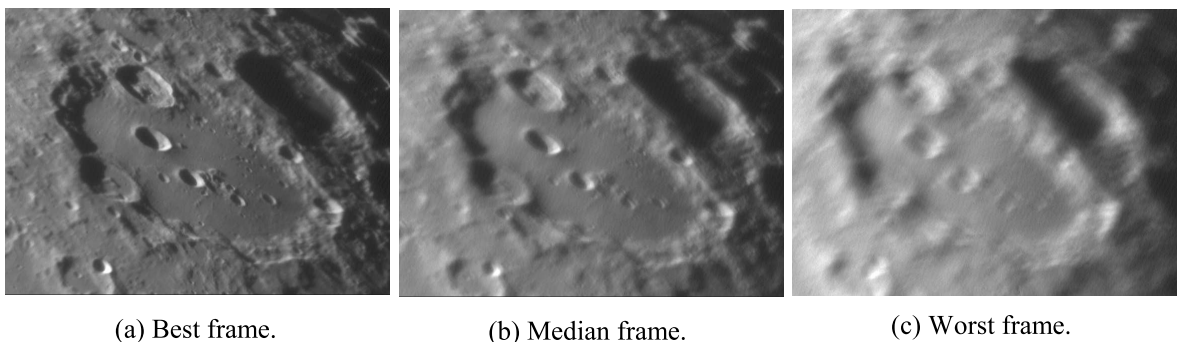


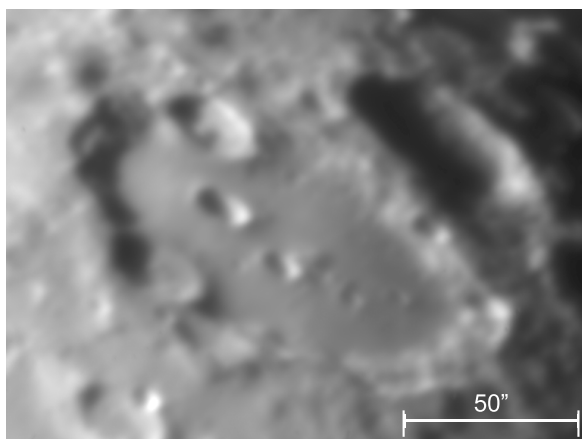
FIGURE 7.1: The best, median and worst ranked frames from an observation of the lunar crater Clavius. Observations were taken on the ANU 1m telescope, $D = 30cm$ aperture mask, $t = 20ms$, $\lambda = 550nm$ (visual filter). Images are brightness-normalised.

moon transit was tested. We chose the Roggemann et al. (1994) S_{S1} metric for this analysis because it is generally applicable to extended objects. Some FITS cubes were also processed with a contrast metric in order to compare the two methods.

7.2 General planetary imaging

The effectiveness of the S_{S1} sharpness metric for measuring and ranking the frames is demonstrated in figure 7.1, which shows the frames that were ranked best, median and worst in that FITS cube. Note that the images are brightness-normalised, so that the best frame appears overall to be darker than the others because the small bright regions such as the small crater rim at the bottom left are sharpest and therefore brightest in this frame. Figure 7.2 again shows the increasing sharpness with decreasing FSR , and this was among our best results. Because the lunar images completely fill the field, the shift-and-added images show edges of individual frames that have been shifted. These artifacts of alignment are not obvious in the stellar images where the edges are usually dark. These edge regions would normally be cropped for presentation purposes.

The metric also worked well with objects that did not fill the field. This, as well as the behaviour of the metric in different seeing conditions is illustrated by the images of Saturn in figure 7.3. Table 7.1 shows the sharpness scores for each of the images in figure 7.3. Again, as with stellar images, there was improvement made by frame selection in all the seeing conditions encountered. The D/r_0 values shown were derived from the average and standard error values of r_0 for each night, calculated from all of the stellar images taken each night with the visual filter. In the absence of real-time seeing monitoring, this was the only possible way to estimate the seeing during the planetary observations. Since r_0 fluctuates on all time scales, these average nightly values of D/r_0 are only indicative of the conditions each night, rather than the average for each observation. The improvement is the ratio of the sharpness scores of the long exposure over the frame selected image. This is the inverse of the improvement calculation for stellar images because in our S_{S1} algorithm low scores represent high quality.



(a) Long exposure

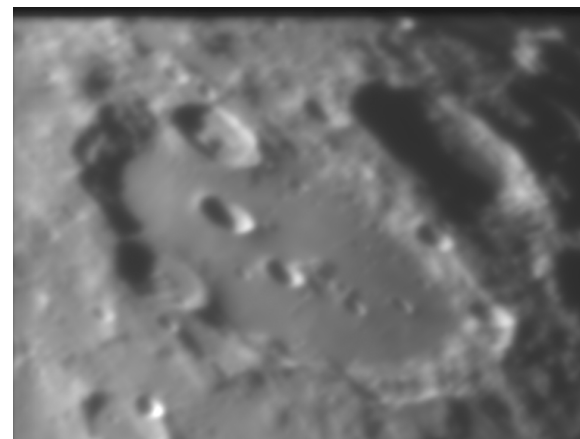
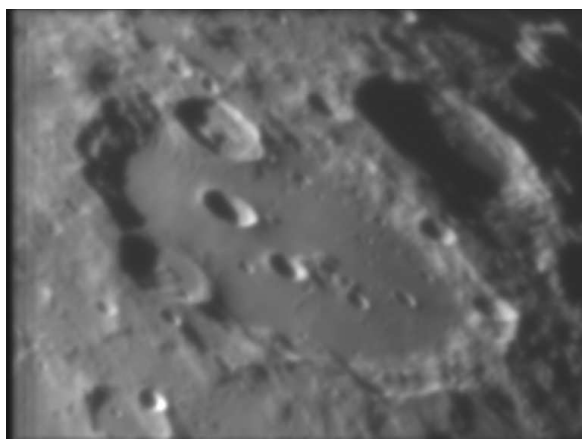
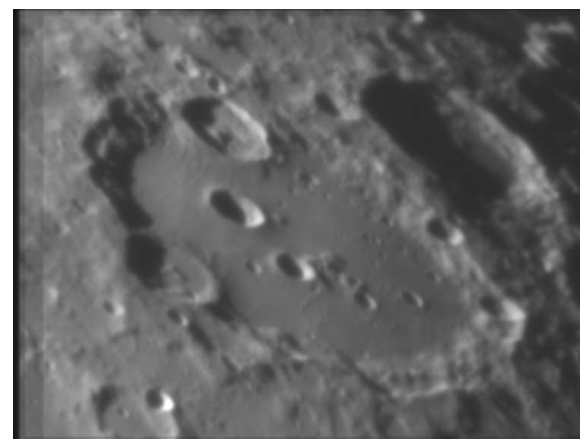
(b) $FSR=100\%$ (c) $FSR=10\%$ (d) $FSR=1\%$

FIGURE 7.2: Images of lunar crater Clavius, with frame selection regime as shown. Images were processed from the same FITS cube as the frames shown in figure 7.1. The angular scale is shown in arcseconds.

TABLE 7.1: Sharpness scores of images in figure 7.3. Note that low scores reflect high quality.

Date	Long Exp.	$FSR = 1\%$	Best frame	Improvement	Average D/r_0
20/3/05	0.245	0.211	0.201	1.16	9.2 ± 1.9
21/3/05	0.205	0.189	0.184	1.08	7.7 ± 1.8
23/3/05	0.202	0.188	0.178	1.07	5.3 ± 3.1

The degree of improvement is again only weakly dependent on D/r_0 just as for stellar images. The slightly higher improvement on the worst night was because of the greater difference between the best and worst frames on that night, as seen in figure 7.4. It is interesting to see, too, that the best frames on the worst night were around the same quality as the worst frames on the better nights.

7.3 Imaging transient events

Transient phenomena put a time constraint on any form of imaging. For selective imaging the requirement is that a statistically significant number of frames must be captured quickly enough that the field has not changed considerably during the observation. For example, when tracking the evolution of fine structure features on the solar photosphere, Denker et al. (2005) took an image sequence every minute, but the time for each image sequence was restricted by the proper motions of the features. They restricted their imaging runs to 30 seconds, which was the average time for solar granules to shift 1 pixel width in the image. Of course, turbulence can cause uncorrelated displacement of different features in an image, that is, rubber sheeting, by several pixels in successive frames.

We imaged a transit of Io on 15th March 2005, where the satellite traversed approximately 41 arcseconds across Jupiter's disc in around 160 minutes while the telescope tracked Jupiter. In figure 7.5 this equates to Io moving at a rate of 1 pixel in 20 seconds or 500 frames. This shift will have an effect on the cross-correlations used to calculate the frame shifts.

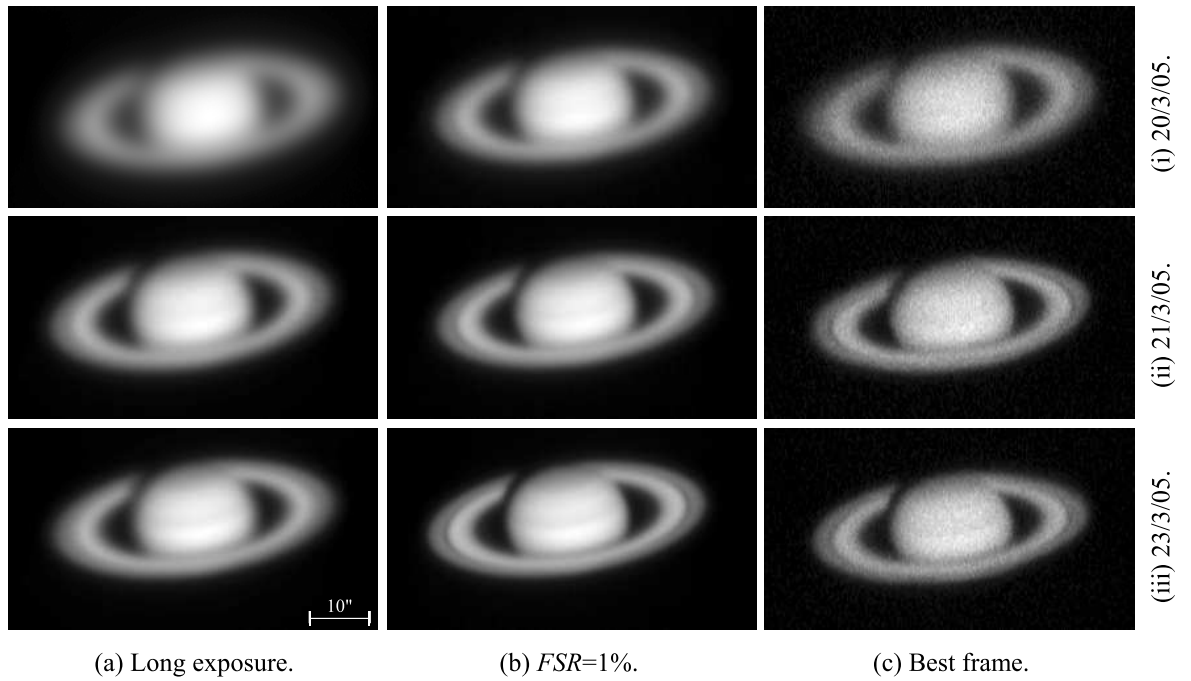


FIGURE 7.3: A table of images of Saturn comparing different seeing conditions. Rows are different dates as shown. Columns show the stacked (a), frame selected (b), and best frame (c) from the observations made on those dates. Observations were taken on the ANU 1m telescope, $D = 30cm$ aperture mask, $t = 20ms$, $\lambda = 550nm$ (visual filter). All images are brightness-normalised.

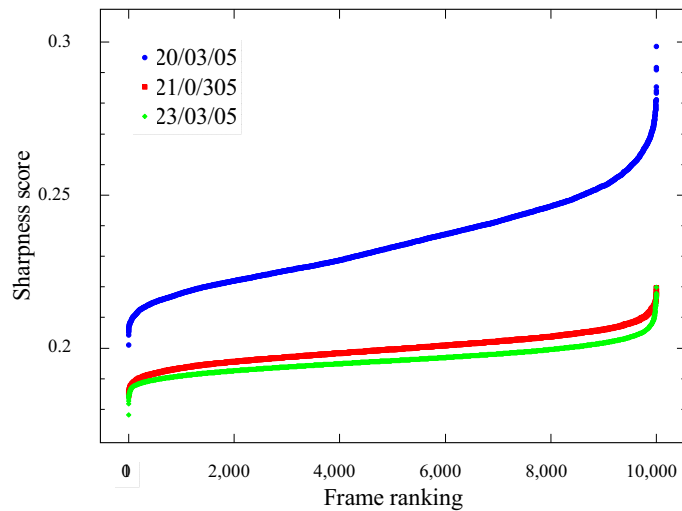


FIGURE 7.4: Graph of sharpness scores for the calibrated and de-interlaced frames from the FITS cubes used in figure 7.3. They are ranked in order of quality from best at left to worst at right. Low scores correspond to high sharpness.

We took 3000 frames in 120 seconds, six times the “pixel-shift” period, and still found an improvement with frame selection, as can be seen in the insets in figure 7.5. The imaging time was still short compared to the time for the entire transit. Although there is some slight elongation of Io in the 1%*FSR* image it is still much more compact than the stacked image. It is possible that, as the seeing comes and goes, many of the good frames occur within a short time interval. To optimise this technique it is possible in post-facto selection to pick out from the whole image sequence the subset of frames spanning the pixel-shift period that has the highest average frame quality, and select the best frames from this subset.

7.4 Comparison of the S_{S1} metric with a contrast operator

We have seen that the S_{S1} metric is an effective measure of the sharpness of images of extended objects such as the Moon and planets. To be fair we need to test other methods for comparison. Of all the metrics described in section 3.3.1 the easiest to apply to extended objects, where there is no prior knowledge of the ideal image, is the S_4 operator (equation 3.4). Baumgardner et al. (2000) used a simple algorithm as a contrast operator (equation 3.5), restated here.

$$C(i, j) = |P(i, j) - P(i + 1, j + 1)| + |P(i + 1, j) - P(i, j + 1)| \quad (7.1)$$

After applying the operator they squared the new image to emphasise small areas of high contrast, and then summed to obtain a sharpness score.

Figure 7.6 shows the 1%*FSR* images and the best frames chosen by each of the two metrics from the same observation of the crater Clavius as in figures 7.1 and 7.2. The coloured box in each of the best frames highlights a region that is sharper than other areas of the same frame (anisoplanatism), and also sharper in that frame than the same region in the rival method’s choice of best frame. The red box in the frame chosen by the S_{S1} metric covers a larger area, suggesting that this method was more

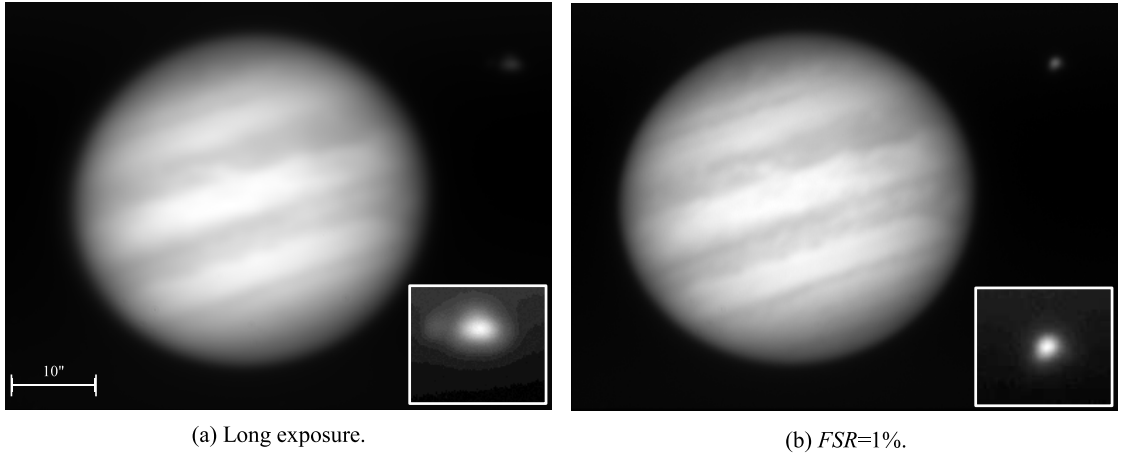


FIGURE 7.5: Images of Jupiter and Io shortly after a transit. Insets show Io magnified and logarithmic scaled. Observations were taken on the ANU 1m telescope, $D = 75cm$ aperture mask with 2.5x magnifier, $t = 20ms$, $\lambda = 700nm$ (red filter).

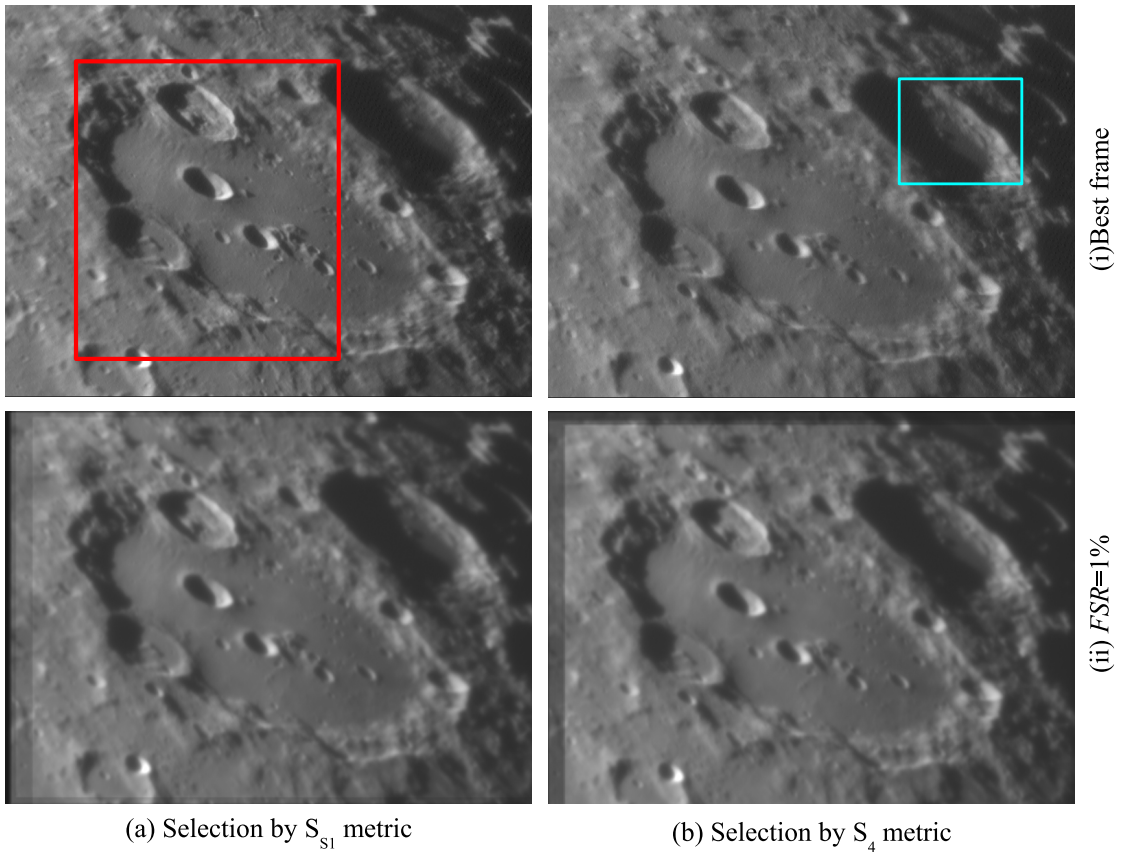


FIGURE 7.6: Images of lunar crater Clavius, from the same FITS cube as in figure 7.2, with best frames (row (i)) and 1% FSR (row(ii)), comparing selection by Fourier methods (S_{S1} metric, column (a)) with the contrast operator (S_4 metric, column (b)).

successful at choosing the best frame than the contrast metric. Despite this, the 1%*FSR* images compiled using both methods show equal sharpness on visual inspection.

The next picture, figure 7.7, shows images of the planet Mercury. It was captured in evening twilight after very warm days, and so the background in the FITS images was bright and the seeing was very poor. The long exposure image shows, in addition to the expected blur, elongation that is due to both atmospheric dispersion and to telescope wind-shake. Both of these effects are the results of the low altitude angle. The best frame chosen by the S_{S1} metric, figure 7.7(a)(iii), shows the planet with a darker patch in the middle of the crescent, giving it somewhat the shape of a cashew nut. The best frame chosen by the contrast operator was more semi-circular, which, at 49% illumination for that date, was closer to the true appearance of Mercury during this observation. So it appears that in this case, the contrast operator made a better choice of best frame. This was because the images of Mercury show little spatial frequency information at this pixel scale, but have distinct contrast between the bright planet and the darker background.

For Venus, the improvement in the ultraviolet image with frame selection was small. This was partly because of the poor twilight seeing, just as for Mercury, but also because at short wavelengths r_0 is smaller, so D/r_0 is larger. Close inspection of the best frames shows that both metrics are finding what they are looking for. S_4 's best frame shows darker and lighter patches, giving a higher average pixel gradient. In the best frame chosen by S_{S1} these features are not as distinct, so it picked out more of the individual pixel-to-pixel noise as high spatial frequency information. The 1%*FSR* images produced by both methods, although not quite identical, are of equivalent visual quality.

Both of the best frames of Mars in figure 7.9 are quite distorted, having uncorrelated displacements of different image regions (rubber sheeting). The best frame chosen by the S_{S1} metric is more compact than it's rival. The sizes of the Martian disc in the 1%*FSR* images from each metric correspond to those in the best frames. It seems that the S_{S1} metric saw frames with a smaller disc as having a higher spatial frequency than

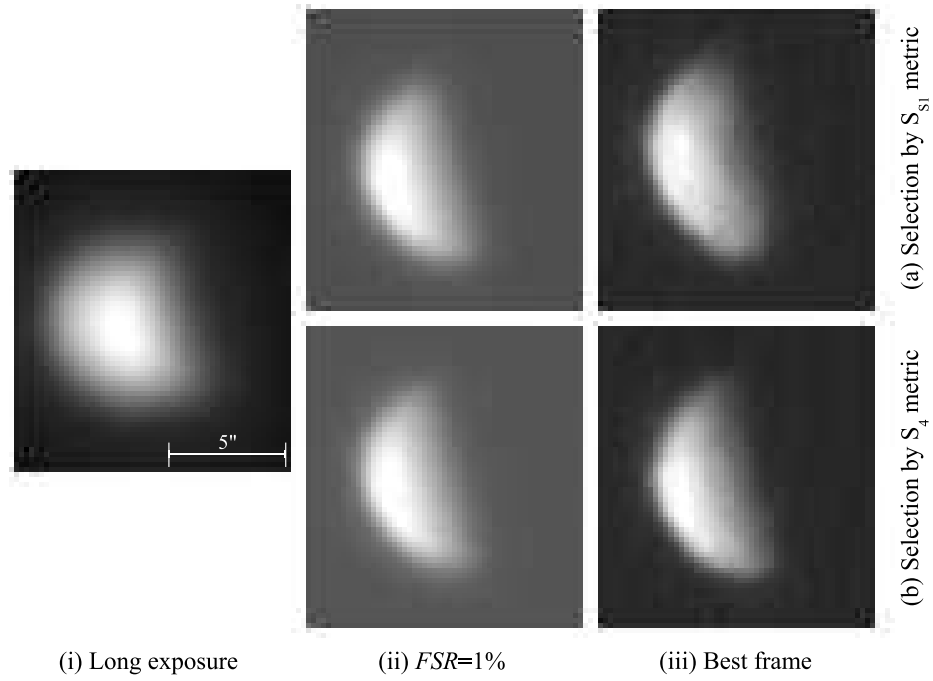


FIGURE 7.7: Images of Mercury, with the long exposure (column (i)), 1% FSR (column (ii)) and best frames (column(iii)) selected from the same FITS cube by Fourier methods (S_{S1} metric, row (a)) and the contrast operator (S_4 metric, row (b)). Observations were taken on the ANU 1m telescope, $D = 30cm$ aperture mask, $t = 8.3ms$, $\lambda = 800nm$ (infrared filter).

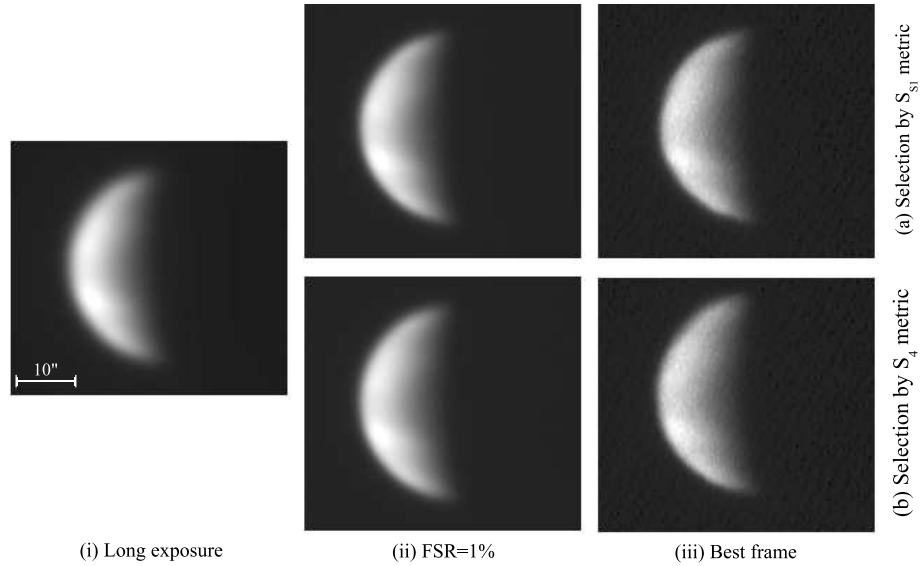


FIGURE 7.8: Images of Venus, with the long exposure (column (i)), 1% FSR (column (ii)) and best frames (column(iii)) selected from the same FITS cube by Fourier methods (S_{S1} metric, row (a)) and the contrast operator (S_4 metric, row (b)). Observations were taken on the ANU 1m telescope, $D = 30cm$ aperture mask, $t = 20ms$, $\lambda = 300nm$ (ultraviolet filter).

those with larger discs. The fact that both metrics chose distorted frames shows that they take no account of morphology. The use of a morphological filter, based on the predicted size and shape of a planet, would be useful to correct for such bad choices. Based on the predicted size of the Martian disc during the observation, 19.8 arcseconds, obtained from the NASA JPL Horizons On-Line Ephemeris System (Giorgini et al. 1996), the best frame of the S_{S1} metric is the better choice. This is discussed further in section 7.5.

The S_4 metric, in the observation of Saturn in figure 7.10, chose as the best frame one where there is contrast between the equatorial and mid-latitude bands, although the outer ring on the right side is more blurred. Once again, however, the 1%*FSR* images from both methods are, visually, practically identical.

Of the fifteen FITS cubes processed with both metrics, in one case both methods chose the same best frame and worst frame, although the median ranked frames were different. In all other cases the two metrics selected different frames. This is unsurprising because the two methods select for different features.

For a less subjective analysis the improvement with frame selection was measured for each method by obtaining the ratio of the sharpness score of the 1%*FSR* image to that of the stacked image for each observation. Both metrics were used to measure not only their own products but also those of the rival method to see if they were in agreement. The metrics agreed that both methods resulted in improvement in every case. However, the metrics generally disagreed on which method gave the greatest improvement. In one case the S_4 metric judged its own product to be slightly inferior to that of its rival, with a difference in improvement factor of only 4%. Apart from this each metric always judged its own product as better. Of course, each metric finds in its own product the features that were selected for; S_{S1} selects for high spatial frequency information, whereas the S_4 metric looks for high contrast as measured by pixel gradient. What is perhaps surprising is what little difference there was in the images produced by the two methods. The S_{S1} method measured the greatest difference in sharpness score (in its own favour) for one observation as 12%, six cases showed less than 5% difference and three cases less than 1% difference.

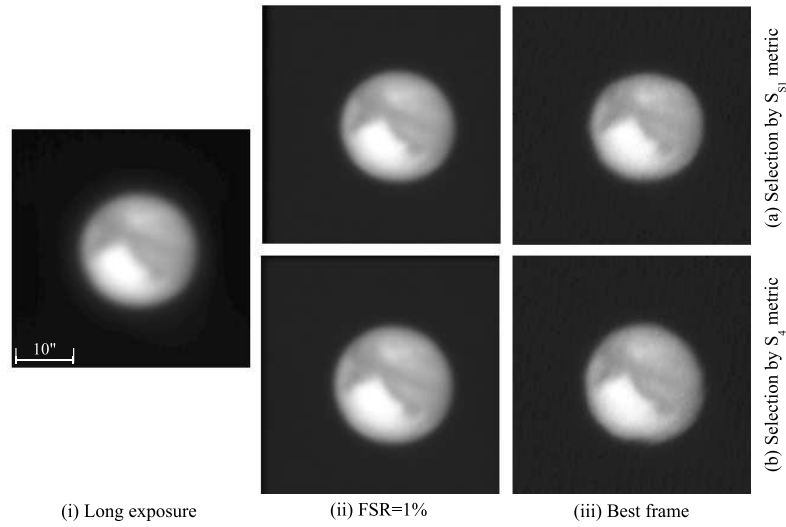


FIGURE 7.9: Images of Mars showing part of the Valles Marineris, with the long exposure (column (i)), 1%FSR (column (ii)) and best frames (column(iii)) selected from the same FITS cube by Fourier methods (S_{S1} metric, row (a)) and the contrast operator (S_4 metric, row (b)). Observations were taken on the ANU 1m telescope, $D = 30cm$ aperture mask, $t = 20ms$, $\lambda = 800nm$ (infrared filter).

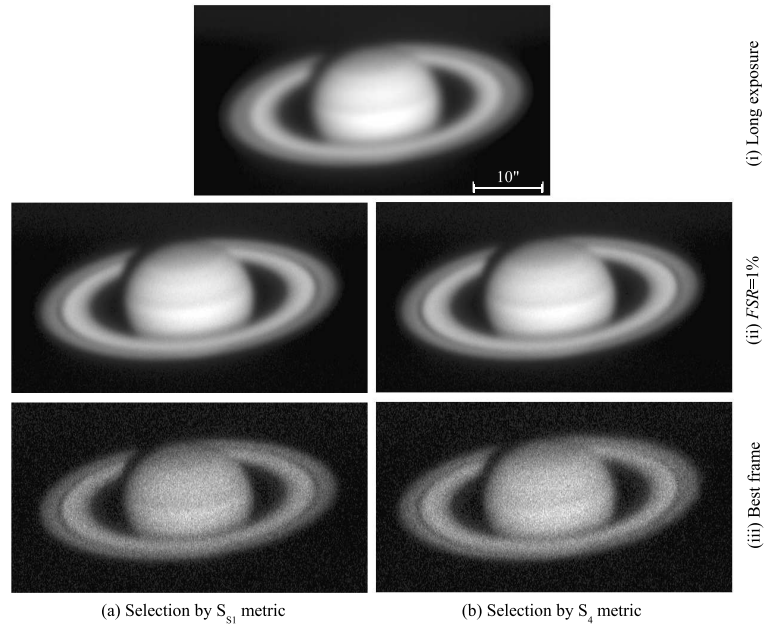


FIGURE 7.10: Images of Saturn, with the long exposure (row (i)), 1%FSR (row (ii)) and best frames (row(iii)) selected from the same FITS cube by Fourier methods (S_{S1} metric, column (a)) and the contrast operator (S_4 metric, column (b)). Observations were taken on the ANU 1m telescope, $D = 75cm$ aperture mask with $2.5\times$ focal reducer, $t = 8.3ms$, $\lambda = 550nm$ (visual filter).

On balance it appears that both methods can produce equally sharp images of solar system planets. The method S_{S1} should be applied to objects with strong spatial frequencies such as atmospheric or ring banding. For objects with sharp edges the contrast operator may be more applicable. S_4 is the simpler algorithm to encode, but S_{S1} may be more universally useful, not just for planetary imaging but also when applied to deep sky objects. Future observations with low noise EMCCD cameras will enable this to be tested.

7.5 Limitations of the S_{S1} and S_4 metrics

The stellar and the planetary images presented in this chapter and the previous one show that frame selection is effective in improving the sharpness of turbulence degraded images. However it is evident that the results were better for stars than for planets. The fact is, because the ideal star image is easily determined it is much easier to judge the sharpness of stellar images than planetary images.

Stars very closely approximate point sources, and would hypothetically appear as small bright points in images taken in the absence of atmosphere or telescope structure. In reality light is spread away from the image point mostly by turbulence, but also by telescope optics, which includes diffraction from the aperture and mirror supports, and any optical aberrations. This spread of flux most commonly produces a speckle pattern and reduces the brightness of the star's image. There is thus a direct relationship between the brightness of the peak and the sharpness of the image. The brightest pixel metric by its nature selects frames where the flux is concentrated in the smallest spot. Thus it is effective not only at finding the minority of frames where turbulence is minimal, but also the very rare frames where the turbulence compensated for the optics (very lucky observer mode). That is why the brightest pixel criterion worked so well.

For extended objects, such as lunar and planetary features, there is usually no ideal image by which to measure the raw frame sharpness. Unless there is a bright star in the image, there is also no way to deconvolve the PSF. The greater the wavefront

aberrations the more speckled is the instantaneous PSF. Each raw pixel value is affected by not only the speckle pattern at that point, but also by the speckle patterns of all the surrounding pixels within the seeing radius. In general this convolution will result in blur, which reduces pixel gradients and the strength of high spatial frequency information. Thus the sharpest frames are usually those that retain strong high spatial frequencies in the autocorrelation, and steep pixel gradients. Both the S_{S1} and S_4 metrics we used work on that basis.

There may be moments, however, when the instantaneous PSF causes smooth areas to become speckled or edges to become jagged. The result will be a momentary increase in average pixel gradients and high spatial frequencies. Both of the metrics will rank such frames as among the sharpest even though the image is of poor quality. Also, just as it is possible in very rare moments for the turbulence to counteract optical aberrations, it is also possible that at times the seeing will accentuate these aberrations such that the metrics are fooled. This might be termed the “very *unlucky* observer mode”. The upshot is that the correspondence between high spatial frequencies, or average pixel gradients, and image quality is not as strong as for the peak pixel metric for star images.

This study used a relatively inexpensive camera. When the seeing was very bad, the amount of blur necessitated the camera gain being set to maximum, making the pixel noise significant. This pixel noise adds to average pixel gradients and high spatial frequency information, making it harder for the metrics to distinguish the quality of different frames. It is important to have a satisfactory SNR, and this effect is expected to be much less substantial with the use of a low noise EMCCD. In addition, the majority of our observations were made on the ANU 1 m telescope, which is known to have astigmatism. This aberration reduces the contrast of an image, and so the extended object metrics have less contrast with which to work. The effect is less noticable for point sources than extended objects.

The distortions in the shape of Mars in both of the best frames (figure 7.9), as well as the cashew shape of Mercury (figure 7.7), show that, regardless of the sharpness metric used, morphological filtering of frames can be beneficial to reduce the effects of rubber

sheeting, as demonstrated by Baumgardner et al. (2000) in identifying features on the surface of Mercury. The trade-offs of this extra step are the requirement for a-priori knowledge of the subject, difficult for some objects, and the additional computational complexity.

Taking the Mars example of figure 7.9, the best frames and 1%*FSR* images are displayed again in figure 7.11, with red circles representing the known size and shape of Mars obtained from the NASA JPL ephemeris superposed on the Martian discs. Note that the Martian oblateness of 0.0065 is negligible at this image scale. It can be seen that, although in the S_{S1} best frame Mars is somewhat distorted it fits inside the red circle, as it does in the corresponding frame-selected image, very neatly. Both the best frame and the selective image for the S_4 metric are stretched so that they don't fit into the circle. So in this case the S_{S1} metric produced the more morphologically correct image.

The main reason for the dramatic improvement in the stellar images processed by the peak pixel metric was that the brightest star was also the co-alignment point, so this place in the image showed artificially high improvement in sharpness, with improvement factors as high as 6. Elsewhere in the image the improvement was not as great, dropping to around 3 within 20 arcseconds for 1%*FSR*. In the planetary images the co-alignment position is not necessarily sharpened more than any other region, so the best possible improvement may be only the factor of 3 across the field.

7.6 Summary

Using metrics suited to extended objects rather than point sources, these experimental observations showed that the frame selection technique is well suited to solar system imaging. Although improvement was made in all seeing conditions, the results of frame selection were better when either the seeing was good or smaller apertures were used, or both, giving low D/r_0 . Likewise, the lower the *FSR* the less bad frames are included so the output images are sharper.

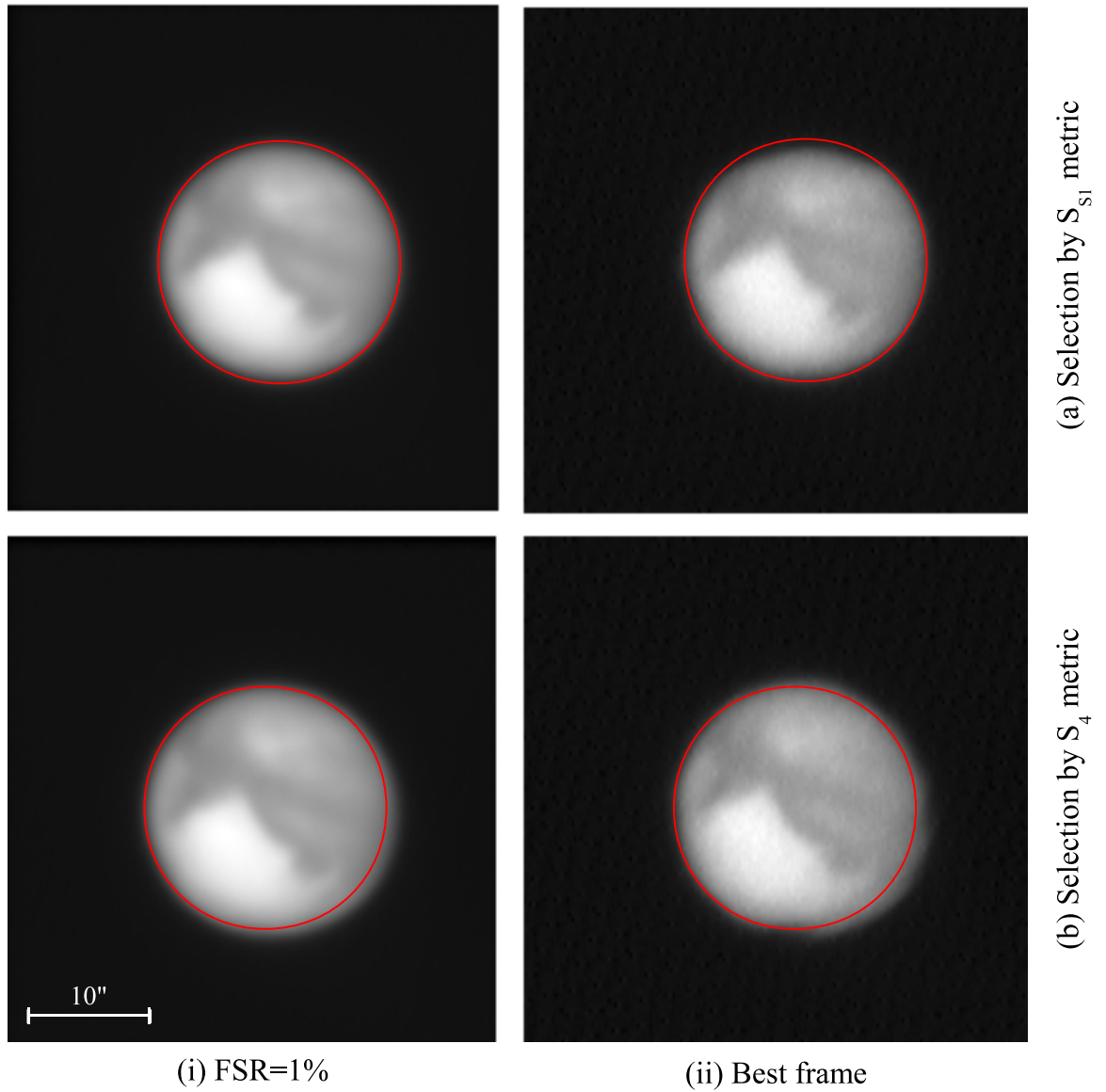


FIGURE 7.11: $1\%FSR$ and best frame images of Mars from figure 7.9. The red circles are $19.8''$ diameter, and show the size and shape of Mars in the images compared to the known morphology.

Transient phenomena can be imaged effectively by lucky imaging. Ideally a significant number of frames, enough to have several good ones to choose from, need to be captured in a short interval such that the image doesn't change. We demonstrated that frame selection gives improvement even when the imaging run is several times longer than the ideal time, as long as the period is short compared to the time for the whole

event.

The S_{S1} metric was used for the general analysis because it is universally applicable to extended objects. Its performance was compared to that of a contrast operator on several of the FITS cubes. It was found that they usually ranked the frames in a different order, each selecting frames that strongly show the features for which they look. In spite of the different ranking orders the difference in quality of the resulting images from each method was usually small, and often negligible.

These experiments successfully demonstrated the improvement in image sharpness that selective imaging provides. However, it was noted that the improvement in the planetary images was not as great as for the stellar images. Lower sharpness gains may be intrinsic to images of extended objects, as opposed to point sources. The situation may be improved in future observations that will be made with a low noise EMCCD. This camera will be used in surveys of solar system planets, their mineralogy and atmospheric composition and dynamics.

Chapter 8

Conclusions

The behaviour and effectiveness of the selective imaging method, sometimes known as lucky imaging, has been examined empirically by observing both stellar and planetary objects using the *MUSIC* instrument as described in chapter 4. Post-processing of the data was performed using the frame selection programs outlined in chapter 5. The stellar imaging in particular enabled frame selection parameters to be thoroughly tested, making use of the simplest possible sharpness metric; the brightest pixel in each frame. The effects of the various frame selection parameters were found by plotting them against the Strehl ratios of the stellar peaks in the output images.

Our results are consistent with previous theoretical and observational studies, but supplement them by covering a much wider range of parameter space. Other studies have mostly concentrated on particular instruments at sites with good seeing, imaging in particular wavelength bands and exposure times, as appropriate to their specific research areas. To make our data as generally applicable as possible, we used a variety of telescopes, each with an array of aperture masks, colour filters, and camera exposure times. To maximise the range of r_0 we also conducted our observations in whatever seeing conditions prevailed, sometimes making use of raw data that was of poor quality that would normally be rejected outright.

It has been found in many prior studies that shift-and-add processing of short exposures is very effective at removing the tilt component of the seeing effects, although it does little to negate any high order effects. Our data confirmed this, but also found

that by being selective of the quality or sharpness of the frames to include in the shift-and-add, high order effects can be attenuated. The more selective one is, that is, the smaller one's FSR or the higher one's quality threshold for frame inclusion, the more closely the resulting image approaches the diffraction limit. Many of the stellar images that were created by taking just 1% of the sharpest frames display faint diffraction rings and spikes. Increasing sharpness comes at the cost of signal-to-noise ratio, but this is recovered by recording many thousands of frames (which is becoming easier with improvements in computing technology), and by the increasingly common use of low noise cameras.

The quality of the final images depends crucially on the seeing-normalised aperture, D/r_0 . Image quality was improved with frame selection at all values of D/r_0 that we tested, between 2.8 and around 30. Because in good seeing the average frame quality is better, and small apertures cover fewer turbulence cells, frame selected images taken at low D/r_0 have the highest sharpness. Several of our images had Strehl ratios greater than 0.6, and the highest we achieved was 0.8 at $D/r_0 = 2.8$. Other observational tests of frame selection have reached Strehl ratios of around 0.3.

For low to moderate D/r_0 (< 12) the improvement factor, that is the gain in Strehl ratio for shift-and-added images compared to the long exposure images, was rather insensitive to D/r_0 . The peak at $D/r_0 \sim 7$ was expected but was not very pronounced. The improvement was greatest for smaller FSR , with the 1% FSR images showing an improvement factor greater than 5 for D/r_0 between 4.5 and 7.8.

Frame selection produced improvements in Strehl ratio for frame exposure times as long as $t = 0.64$ s. The improvement is greater for shorter times, but we found that the trends begin to flatten at $t \sim 10$ ms, below which the gain in improvement was not significant. So we recommend that for sufficiently bright targets viewed from the Siding Spring mountain site the frame exposure time should be limited to 10 ms. This is shorter than the coherence times found for some other sites that have better seeing.

Image sharpness was improved for all wavelength bands tested. However, it was found that imaging at longer wavelengths produced higher Strehl ratios in the long exposure images, hence also in the frame selected images. This was because r_0 is larger

at longer wavelengths, giving a smaller D/r_0 for a given aperture. Hence the average frame quality was better. This makes selective imaging most suitable for observing in the infrared.

When stellar image cubes were shift-and-added it was found that the sharpness of region around the recentring co-ordinates was significantly improved, but that the quality diminished with distance across the field. For example, secondary stars improved with frame selection even over distances as large as 100 arcseconds, but not in proportion to the brightest star in the field. This occurred with both the peak-pixel and the cross-correlation methods of image recentring, and seemed to be independent of FSR or D/r_0 .

For planetary imaging the S_{S1} metric, which uses autocorrelation to measure frame sharpness, was found to be effective at it's job. It worked well with lunar images, which filled the whole field with structure, as well as with images of solar system planets that are generally discs (or portions of discs) surrounded by darkness. The S_4 metric in the form of a contrast operator was found to produce equally sharp images from the same FITS cubes in most cases, despite ranking the frames in a different order. The difference in sharpness of the final products of the rival methods, as measured by both algorithms, was usually only a few percent. The S_4 metric involves less computation but is less universally applicable than the S_{S1} metric. It was found that because neither metric considered the object morphology, both of them occasionally ranked distorted images among the best. So planetary frame selection could benefit from the extra step of morphological filtering of frames in addition to sharpness filtering. Of course, this adds computational complexity and is not possible where there is no prior knowledge of the object.

It was found, however, that the improvement in the sharpness of the planetary images was, in many cases, not as great as for the stellar images. This was because the peak pixel metric for point sources has a direct correspondence with image sharpness, whereas the correspondence is not as strong for the extended-object metrics. Also, when cross-correlation is used for the shift-and-add processing of extended object images, it does not sharpen the alignment point more than the rest of the image, as it

did for images with a single brightest star.

Frame selection was found to give improvement in sharpness even when imaging transient events where one or more objects in the field are slowly moving. Optimizing these observations requires that enough frames be captured in a sufficiently short time that the field does not change during the recording.

We have found that a selective imaging system will give best performance when using a low-noise camera on a telescope that has good quality optics, so that the raw data is as good as possible. The telescope aperture should be at least 7 times the average r_0 for the site. When the seeing varies from this, D/r_0 must be optimised by the use of aperture masks. It may be possible to construct a variable-aperture diaphragm in the focal plane that can continuously adjust the aperture in response to real-time seeing monitoring. Of course, this will make the system more complex and expensive. Dispersion correction should be used, if available, for imaging at high zenith angles. The frame exposure time should be limited to the average coherence time for the site. The effects of anisoplanatism should be minimised by windowing the field of view to be only as large as necessary to capture the target. Finally, a sharpness metric suitable for extended objects, such as S_{S1} , will be most generally applicable.

We have treated the frame selection technique in isolation to examine its behaviour, and in appropriate imaging regimes it can be used as a stand-alone process. However its ultimate usefulness is in complementing or reducing the dependence on other techniques. For example shift-and-added images can benefit from further sharpening by un-sharp masking or wavelet filtering, but the need for such post-processing is reduced by the use of frame selection. It can also be used in conjunction with speckle imaging and/or adaptive optics to improve the results of those techniques. Our study shows that lucky imaging deserves its growing status and popularity as a technique for high resolution astronomical imaging.

Appendix A

MUSIC Software Programs

This table lists the C++ software programs used in the *MUSIC* project. The purpose and function of each program is briefly described, and those included object header files relevant to *MUSIC* are listed to show the object oriented connections. The authorship and important algorithms are detailed in section 4. The programs are divided into four broad categories: those used for data acquisition and calibration, for frame selection, for sundry tasks such as separating frames or image resizing, and the object headers for image access and manipulation.

TABLE A.1: *MUSIC* Software Summary

Program Name	Description	Relevant Header Files Included
Frame acquisition and calibration		
acquire.C	Sends camera output to rtd tool for real time display on GAIA.	dproc_rtd.h, datafile.h, dt3155.h, dt3155_lib.h
music.C	Same as acquire.C, and writes frames to FITS cube.	dproc_rtd.h, datafile.h, dt3155.h, dt3155_lib.h
biasflat.C	Performs bias and flat field calibration of frames in a FITS cube.	datafile.h
deint.C	De-interlaces frames in a FITS cube.	datafile.h
Frame selection and combining		
stack.C	Average-combines all frames in a FITS cube without selection or alignment. Simulates a long exposure.	datafile.h
stackfwhm.C	Modified version of stack.C that also measures the FWHM of the brightest star.	datafile.h

Program Name	Description	Relevant Header Files Included
combine.C	Early test of frame selection using peak pixel criterion, and shift-and-adding those exceeding quality threshold.	datafile.h
combsort.C	Modified version of combine.C that sorts frames in order of peak pixel value and shift-and-adds the desired <i>FSR</i> .	datafile.h
combfft.C	For extended objects, measures sharpness by autocorrelation, then shift-and-adds by cross-correlation.	datafile.h
combcont.C	For extended objects, measures sharpness by pixel contrast, then shift-and-adds by cross-correlation.	datafile.h
fftscore.C	Measures sharpness by autocorrelation without shift-and-adding frames.	datafile.h
contscore.C	Measures sharpness by pixel contrast without shift-and-adding frames.	datafile.h
Miscellaneous programs		
combconsec.C	Stacks groups of n consecutive frames to make a FITS cube of simulated longer exposures.	datafile.h
squarify.C	Pastes a FITS image onto a larger blank square image of size 2^n , to use image with <i>strehl</i> function.	datafile.h
playback.C	Displays a FITS cube as a video sequence on GAIA.	dproc_rtd.h, datafile.h
playframe.C	Displays a selected frame from a FITS cube on GAIA.	dproc_rtd.h, datafile.h
frame.C	Writes a selected frame from a FITS cube to its own FITS file.	datafile.h
Header files used with MUSIC		
rtdImageEvent.h	Takes data to an rtd application such as GAIA.	
dproc_rtd.h	Class to take CCD data to the rtd tool.	dproc_err.h, rtdImageEvent.h
dproc_err.h	Provides error handling for dproc_rtd.h.	
datafile.h	Creates, opens, closes, establishes access to FITS files	fitsio.h, dproc_err.h
dt3155.h, dt3155_lib.h	Drivers for the DT3155 frame grabber.	

Appendix B

Stellar Objects Observed with *MUSIC*

This appendix contains tables that show relevant astrometric data on the stellar objects observed for the *MUSIC* project. Table B.1 lists the single stars of various magnitudes that were observed to test how well the system worked with bright and faint stars. The data was obtained from the Hipparcos catalogue (Perryman et al. 1997).

TABLE B.1: Data on single stars imaged for *MUSIC*

Identifier	R. A. (Hr Min Sec)	Dec (Deg Min Sec)	V mag	Epoch
SRS 1491 (Cen)	12 31 59.3	-41 3 18.5	7.1	2000
θ Cen	14 6 40.9	-36 22 11.8	2.1	2000
Diphda (β Cet)	00 43 35.4	-17 59 11.8	2.0	2000
Alphard (α Hyd)	9 27 35.2	-08 39 31.0	2.0	2000
ν Hydrae	10 49 37.5	-16 11 37.1	3.1	2000
ϕ 2 Lupi	15 23 9.4	-36 51 30.6	4.5	2000
Rigel (β Ori)	5 14 32.3	-8 12 5.9	0.2	2000
Ankaa (α Pho)	0 26 17.1	-42 18 21.5	2.4	2000
δ Vel	8 44 42.3	-54 42 31.8	1.9	2000
λ Vel	9 07 59.8	-43 25 57.3	2.2	2000

Binary and multiple systems of various magnitude differences and angular separations were captured to test the effects of selective shift-and-add processing on the sharpness across the field, and also to see how closely spaced stars could be resolved. The data in table B.2 for these objects was taken from either the Washington Double Star Catalog (WDS) maintained at the U.S. Naval Observatory (Mason et al. 2001), or from <http://www.dibonsmith.com/orbits.htm>, copyright Richard Dibon-Smith (D-S). For the WDS catalogue the year stated is the date of the most recent measurement. In table B.2 I have included angular separations from the catalogues (Ref sep column), which are the latest standard measurements, and those calculated from our observations (Meas sep column), which are the average of those measured from all the FITS cubes for each object. Differences between measured and reference separations are usually due to proper motions over the time interval. For multiple systems each line in table B.2 refers to the two stellar components of the system listed (A, B, ...). There were 5 cases where the separations could not be measured because they were too close and/or the raw frames were too noisy.

TABLE B.2: Data on binary and multiple systems imaged
for *MUSIC*

Identifier	R. A. (Hr Min Sec)	(Dec) (deg min sec)	V mag	Meas sep. (arcsec)	Ref sep (arcsec)	Epoch/ Date	Ref
ν Car	9 47 6.1	-65 4 18.2	3.0, 6.0	5.3	5.0	2000	WDS
α Cen	14 39 40.9	-60 50 6.5	0.1, 1.2	10.2	8.8	2007	WDS
42 Cet	1 19 48.3	-0 30 32.5	6.5, 7.0	1.0	1.7	2008	WDS
66 Cet	2 12 47.5	-2 23 37.1	5.7, 7.7	17.8	16.6	2007	WDS
γ Cet	2 43 18.0	+3 14 8.9	3.5, 6.2	2.4	2.3	2006	WDS
Acamar (θ Eri)	2 58 15.7	-40 18 17.0	3.2 4.1	8.7	8.4	2002	WDS
ρ 2 Eri	3 2 42.3	-7 41 7.7	5.4, 8.9	-	1.5	1990	WDS
FIN 333 (Hor)	2 43 26.6	-66 42 51.2	6.5 8.2	-	0.4	2008	WDS
β Hyd	11 52 54.5	-33 54 29.3	4.7, 5.5	-	0.7	1998	WDS
γ Lep	2 43 18.0	+3 14 8.9	3.6, 6.3	102.1	97.1	2002	WDS
γ Lup	15 35 8.4	-41 10 0.4	3.0 4.5	0.8	0.8	2009	WDS
π Lup	15 5 7.2	-47 3 4.3	4.6, 4.6	1.7	1.7	2007	WDS
β Mon A,B	6 28 49.1	-7 1 59.0	4.6, 5.0	8.2	7.2	2008	WDS
β Mon A,C	6 28 49.1	-7 1 59.0	4.6, 5.3	10.0	9.9	2008	WDS
ρ Oph	16 25 35.1	-23 26 49.6	5.1 5.7	3.3	3.3	2007	WDS
τ Oph	18 3 4.9	-8 10 49.3	5.2, 5.9	1.7	1.7	2000	D-S
η Ori	5 24 28.6	-2 23 49.7	3.6, 4.9	1.9	1.8	2009	WDS
ζ Ori	5 40 45.5	-1 56 33.3	1.9, 3.7	2.5	2.4	2008	WDS
M42 Trapezium (θ 1Ori A,C) ¹	5 35 15.8	-5 23 14.3	5.1, 6.6	14.2	12.8	2008	WDS
θ Pic	5 24 46.3	-52 18 58.5	6.2, 6.8	40.9	38.1	2002	WDS
k Pup	7 38 49.3	-26 48 06.6	4.5, 4.7	9.9	10.9	2000	D-S
SAO234538 (Pup)	6 29 49.0	-50 14 20.7	6.0, 8.0	11.9	11.9	1999	WDS
β Sco	16 5 26.2	-19 48 19.4	2.6, 4.5	14.4	13.6	2007	WDS
γ Sext	9 52 30.5	-8 06 17.7	5.4, 6.4	0.6	0.6	2009	WDS
γ Vel	8 9 32.0	-47 20 11.8	1.8, 4.1	43.8	42.9	2002	WDS
ψ Vel	9 30 42.0	-40 28 0.2	3.9, 5.1	-	0.3	2006	WDS
ADS9392 (Virg)	14 48 53.3	+05 57 15.9	7.0, 8.9	0.9	0.9	2008	WDS
γ Virg	12 41 39.6	-1 26 57.9	3.5 3.5	-	1.2	2000	WDS

¹For the Trapezium WDS only lists separations from θ 1Ori A, but we measured from the brightest star which is θ 1OriC, so only that pair is included here.

Appendix C

MUSIC Observation Log

This table contains the log of observations carried out for the *MUSIC* project. For clarity it is sorted by target object. Stars, binaries and clusters are in alphabetical order of constellation, and then the Moon and planets.

The telescope and camera used for the object is indicated across the top of each table section. Each line of the table refers to a particular observing run, or FITS cube. The first two columns show the observation date and Universal Time. Column 3 shows the number of the observing run on the particular night. As the FITS cubes were acquired they were stored on the Linux PC in a folder named for that date. The cubes for each night were numbered from 001. An example of a filename and location is `../mar1505/run032.FITS`. The next two columns indicate the aperture and colour filter used, respectively. Next is the frame exposure time as indicated on the camera control box. The setting “off” means that the electronic shutter was disabled and the exposure time was equal to the camera frame rate of $1/25$ sec. The seventh column shows the camera gain. Columns 8 through 10 show the dimensions of the FITS cube. Column 11 indicates whether the Powermate focal extender was used (y) or not used (n). The final column contains any notes for that run.

TABLE C.1: *MUSIC* Observing Log

Date	UT	Run no.	Aperture	Filter	Exposure	Gain	Total Frames	Frame Size X pixels Y pixels	Power- mate	Notes
α Canis Majoris (Sirius)										
ANU 1m, camera 1										
14/3/05		001	75cm	I	1/10000	0	5000	400	300	n
ν Carinae										
ANU 1m, camera 1										
14/3/05	14:30	042	75cm	I	1/1000	7	5000	160	160	n
"	14:35	043	"	I	1/500	5	5000	160	160	n
"	14:41	044	"	I	1/250	3	5000	160	160	n
"	12:46	045	"	I	1/120	2	5000	160	160	n
"	14:50	046	"	I	off	0	5000	160	160	n
"	15:07	047	30cm	I	off	1	5000	160	160	n
"	15:12	048	"	I	1/120	3	5000	160	160	n
"	15:16	049	"	I	1/250	4	5000	160	160	n
"	15:21	050	"	I	1/500	5	5000	160	160	n
"	15:25	051	"	I	1/1000	6	5000	160	160	n
"	15:30	052	"	V	1/1000	6	5000	160	160	n
"	15:34	053	"	V	1/500	5	5000	160	160	n
"	15:39	054	"	V	1/250	4	5000	160	160	n
"	15:44	055	"	V	1/120	2	5000	160	160	n
"	15:49	056	"	V	off	0	5000	160	160	n
α Centauri										
ANU 1m, camera 1										
14/3/05	14:13	041	75cm	I	1/1000	0	5000	200	200	n
"										
15/3/05	15:53	041	"	I	1/1000	3	5000	200	200	n
"	15:58	042	"	I	1/500	1	5000	200	200	n
"	16:03	043	"	I	1/250	0	5000	200	200	n
"	16:08	044	"	V	1/120	0	5000	200	200	n
"	16:14	045	"	V	1/500	0	5000	200	200	n
"	16:18	046	"	V	1/1000	0	5000	200	200	n
θ Centauri										
ANU 1m, camera 1										
18/3/05	17:57	042	30cm	V	1/1000	4	5000	200	200	n
"	18:02	043	"	V	1/500	4	5000	200	200	n
"	18:10	044	"	V	1/250	3	5000	200	200	n
"	18:17	045	"	V	1/120	2	5000	200	200	n
"	18:22	046	"	V	off	1	5000	200	200	n
"	18:27	047	"	I	off	1	5000	200	200	n

Date	UT	Run no.	Aperture	Filter	Exposure	Gain	Total Frames	Frame Size X pixels Y pixels		Power- mate	Notes
"	18:32	048	"	I	1/120	1	5000	200	200	n	
"	18:36	049	"	I	1/250	2	5000	200	200	n	
"	18:42	050	"	I	1/500	4	5000	200	200	n	
"	18:47	051	"	I	1/1000	6	5000	200	200	n	
<i>v</i> Centauri											
ANU 1m, camera 1											
19/3/05	12:01	013	75cm	I	1/250	6	5000	200	200	n	
"	12:07	014	"	I	1/500	7	5000	200	200	n	
"	12:12	015	"	I	1/120	4	5000	200	200	n	
"	12:17	016	"	I	off	3	5000	200	200	n	
"	12:25	017	"	I	off	2	5000	200	200	n	
"	12:29	018	"	I	1/1000	9	5000	200	200	n	
"	12:38	019	"	V	1/1000	8	5000	200	200	n	
"	12:46	020	"	V	1/500	5	5000	200	200	n	
"	12:52	021	"	V	1/250	4	5000	200	200	n	
"	12:58	022	"	V	1/120	2	5000	200	200	n	
"	13:14	023	"	V	off	0	5000	200	200	n	Cloud
SRS 1491 (Centaurus)											
AAT, camera 2											
25/6/05		030	1m	R	off	4	3000	768	576	n	
"		031	1m	R	off	14	1000	768	576	n	Defocussed
"		032	1m	R	off	14	1000	768	576	n	Defocussed
"		033	1m	R	off	9	3000	768	576	n	In focus
β Ceti (Diphda)											
ANU 1m, camera 2											
9/11/05	10:13	038	30cm	R	1/250	0	3000	768	576	n	
"	10:15	039	"	I	off	0	3000	768	576	n	
"	10:22	040	"	V	off	0	3000	768	576	n	
"	10:25	041	"	B	off	0	3000	768	576	n	
"	11:05	042	75cm	R	1/250	0	3000	768	576	y	
"	11:08	043	"	V	off	0	3000	768	576	y	
"	11:13	044	"	B	off	0	3000	768	576	y	
"	11:19	045	"	I	1/120	0	3000	768	576	y	
42 Ceti											
ANU 1m, camera 2											
11/11/05	11:01	040	30cm	R	off	7	5000	200	200	n	
"	11:08	041	"	V	off	7	5000	200	200	n	
"	11:14	042	"	B	off	14	5000	200	200	n	
"	11:21	043	"	I	off	10	5000	200	200	n	

Date	UT	Run no.	Aperture	Filter	Exposure	Gain	Total Frames	Frame Size X pixels Y pixels	Power- mate	Notes
66 Ceti										
ANU 1m, camera 2										
11/11/05	12:01	048	30cm	R	off	6	5000	200 200	n	
"	12:08	049	"	V	off	7	5000	200 200	n	
"	12:15	050	"	B	off	11	5000	200 200	n	
"	12:21	051	"	I	off	7	5000	200 200	n	
g Ceti										
ANU 1m, camera 2										
11/11/05	13:45	060	30cm	I	off	6	5000	200 200	n	
"	13:50	061	"	R	off	4	5000	200 200	n	
"	13:55	062	"	V	off	4	5000	200 200	n	
"	14:07	063	"	B	off	5	5000	200 200	n	
θ Eridani										
ANU 1m, camera 2										
9/11/05	14:18	070	30cm	I	off	2	5000	200 200	n	
"	14:24	071	"	R	1/120	0	5000	200 200	n	
"	14:30	072	"	V	1/120	0	5000	200 200	n	
"	14:35	073	"	B	off	0	5000	200 200	n	
"	15:03	074	75cm	R	off	0	5000	300 300	y	
"	15:09	075	"	I	off	2	5000	300 300	y	
"	15:13	076	"	V	off	2	5000	300 300	y	
"	15:18	077	"	B	off	2	5000	300 300	y	
ρ2 Eridani										
ANU 1m, camera 2										
11/11/05	12:39	052	30cm	V	off	7	10000	200 200	n	
"	12:47	053	"	R	off	6	10000	200 200	n	
"	12:56	054	"	I	off	7	10000	200 200	n	
"	13:06	055	"	B	off	14	10000	200 200	n	
12/11/05	12:55	039	75cm	I	1/120	8	10000	200 200	y	
"	13:09	040	"	R	1/120	7	10000	200 200	y	
"	13:18	041	"	V	1/120	7	10000	200 200	y	
"	13:28	042	"	B	1/120	14	10000	200 200	y	
13/11/05	13:34	053	30cm	I	off	5	10000	200 200	n	
"	13:41	054	"	R	off	5	10000	200 200	n	
FIN333 (Horologium)										
ANU 1m, camera 2										
12/11/05	13:45	043	75cm	R	off	8	10000	200 200	y	
12/11/05	13:53	044	"	I	off	8	10000	200 200	y	

Date	UT	Run no.	Aperture	Filter	Exposure	Gain	Total Frames	Frame Size X pixels Y pixels		Power- mate	Notes
α Hydrae											
ANU 1m, camera 1											
18/3/05	13:01	001	30cm	I	1/1000	5	5000	200	200	n	
"	13:06	002	"	I	1/500	4	5000	200	200	n	
"	13:10	003	"	I	1/250	3	5000	200	200	n	
"	13:15	004	"	I	1/120	1	5000	200	200	n	
"	13:20	005	"	I	off	0	5000	200	200	n	
"	13:34	006	"	V	off	0	5000	200	200	n	
"	13:39	007	"	V	1/120	2	5000	200	200	n	
"	13:44	008	"	V	1/250	3	5000	200	200	n	
"	13:59	009	"	V	1/500	4	5000	200	200	n	
"	14:03	010	"	V	1/1000	5	5000	200	200	n	
β Hydrae											
ANU 1m, camera 1											
18/3/05	14:36	014	30cm	V	1/250	9	5000	200	200	n	
"	14:42	015	"	V	1/120	7	5000	200	200	n	
"	14:47	016	"	V	off	5	5000	200	200	n	
21/3/05	13:53	042	30cm	I	off	5	5000	200	200	n	
"	14:00	043	"	I	1/120	7	5000	200	200	n	
"	14:05	044	"	I	1/250	8	5000	200	200	n	
"	14:14	045	"	I	1/500	11	5000	200	200	n	
"	14:19	046	"	I	1/1000	13	5000	200	200	n	
"	14:23	047	"	V	1/1000	13	5000	200	200	n	Saturating
"	14:29	048	"	V	1/500	9	5000	200	200	n	
"	14:39	049	"	V	1/250	7	5000	200	200	n	Seeing improving
"	14:47	050	"	V	1/120	4	5000	200	200	n	
"	14:52	051	"	V	off	3	5000	200	200	n	
23/3/05	11:48	024	75cm	I	off	5	5000	200	200	y	
"	11:53	025	"	I	1/120	7	5000	200	200	y	
"	11:57	026	"	I	1/250	9	5000	200	200	y	
"	12:02	027	"	I	1/500	12	5000	200	200	y	Faint & noisy, wind
"	12:07	028	"	V	1/500	9	5000	200	200	y	increasing 20kt
"	12:12	029	"	V	1/250	7	5000	200	200	y	
"	12:16	030	"	V	1/120	5	5000	200	200	y	
"	12:21	031	"	V	off	4	5000	200	200	y	
ν Hydrae											
ANU 1m, camera 1											
18/3/05	15:04	017	30cm	V	off	0	5000	200	200	n	
"	15:09	018	"	V	1/120	2	5000	200	200	n	
"	15:13	019	"	V	1/250	3	5000	200	200	n	
"	15:18	020	"	V	1/500	5	5000	200	200	n	

Date	UT	Run no.	Aperture	Filter	Exposure	Gain	Total Frames	Frame Size		Power- mate	Notes
								X pixels	Y pixels		
"	15:23	021	"	V	1/1000	7	5000	200	200	n	
"	15:28	022	"	I	1/1000	7	5000	200	200	n	
"	15:33	023	"	I	1/500	5	5000	200	200	n	
"	15:38	024	"	I	1/250	4	5000	200	200	n	
"	15:42	025	"	I	1/120	3	5000	200	200	n	
"	15:46	026	"	I	off	2	5000	200	200	n	
γ Leporis											
ANU 1m, camera 2											
11/11/05	14:17	064	30cm	B	off	5	5000	200	576	n	
"	14:22	065	"	V	off	4	5000	200	576	n	
"	14:29	066	"	R	off	3	5000	200	576	n	
"	14:34	067	"	I	off	3	5000	200	576	n	
γ Lupi											
ANU 1m, camera 1											
14/03/05	16:53	062	30cm	I	1/120	6	5000	600	576	n	
15/3/05	16:30	047	75cm	V	1/250	4	5000	200	200	n	
"	16:36	048	"	I	1/250	7	5000	200	200	n	
π Lupi											
ANU 1m, camera 1											
14/3/05	16:53	061	30cm	I	1/120	6	5000	400	400	n	
ϕ2 Lupi											
ANU 1m, camera 1											
14/3/05	17:45	065	30cm	I	1/250	0	5000	200	200	n	
"	17:50	066	"	I	1/120	0	5000	200	200	n	
"	17:54	067	"	I	1/500	3	5000	200	200	n	
"	17/59	068	"	I	1/1000	4	5000	200	200	n	
β Monocerotis											
ANU 1m, camera 1											
22/3/05	11:59	038	30cm	I	off	6	5000	200	200	n	
"	12:03	039	"	I	1/120	7	5000	200	200	n	
"	12:07	040	"	I	1/250	8	5000	200	200	n	
"	12:12	041	"	I	1/500	10	5000	200	200	n	
"	12:18	042	"	I	1/500	13	5000	200	200	n	
"	12:22	043	"	V	1/500	13	5000	200	200	n	
"	12:26	044	"	V	1/250	11	5000	200	200	n	
"	12:31	045	"	V	1/120	8	5000	200	200	n	
"	12:35	046	"	V	off	6	5000	200	200	n	

Date	UT	Run no.	Aperture	Filter	Exposure	Gain	Total Frames	Frame Size X pixels Y pixels		Power- mate	Notes
ANU 1m, camera 2											
9/11/05	17:10	094	30cm	I	off	6	5000	200	200	n	Bad scope shake 25kt gusts!
"	17:15	095	"	R	off	6	5000	200	200	n	
"	17:20	096	"	V	off	4	5000	200	200	n	
"	17:25	097	"	B	off	6	5000	200	200	n	
"	17:29	098	"	B	1/120	8	5000	200	200	n	
"	17:35	099	"	V	1/120	6	5000	200	200	n	
"	17:39	100	"	R	1/120	6	5000	200	200	n	
"	17:44	101	"	I	1/120	7	5000	200	200	n	
11/11/05	16:54	090	30cm	B	off	5	5000	200	200	n	
"	16:58	091	"	V	off	5	5000	200	200	n	
"	17:03	092	"	R	off	4	5000	200	200	n	
"	17:09	093	"	I	off	5	5000	200	200	n	
12/11/05	16:38	069	75cm	I	off	7	5000	300	300	y	
"	16:43	070	"	R	off	3	5000	300	300	y	
"	16:49	071	"	V	off	3	5000	300	300	y	
"	16:54	072	"	B	off	5	5000	300	300	y	
NGC 2264, Xmas tree cluster (Monoceros)											
ANU 1m, camera 2											
11/11/05	16:15	084	30cm	R	off	9	3000	768	576	n	
"	16:19	085	"	V	off	9	3000	768	576	n	
ρ Ophiuchii											
ANU 1m, camera 1											
19/3/05	18:28	066	30cm	I	off	6	5000	200	200	n	Some cloud
"	18:33	067	"	I	1/120	7	5000	200	200	n	
"	18:37	068	"	I	1/250	8	5000	200	200	n	
"	18:43	069	"	I	1/500	10	5000	200	200	n	
"	18:48	070	"	V	1/500	10	5000	200	200	n	
"	18:53	071	"	V	1/250	9	5000	200	200	n	
"	18:57	072	"	V	1/120	7	5000	200	200	n	
"	19:01	073	"	V	off	6	5000	200	200	n	
21/3/05	17:39	080	30cm	I	off	5	5000	200	200	n	
"	17:43	081	"	I	1/120	6	5000	200	200	n	
"	17:48	082	"	I	1/250	8	5000	200	200	n	
"	17:53	083	"	I	1/500	10	5000	200	200	n	
"	17:58	084	"	I	1/1000	12	5000	200	200	n	
"	18:03	085	"	V	1/1000	13	5000	200	200	n	
"	18:09	086	"	V	1/500	12	5000	200	200	n	
"	18:13	087	"	V	1/250	10	5000	200	200	n	
"	18:17	088	"	V	1/120	8	5000	200	200	n	
"	18:22	089	"	V	off	6	5000	200	200	n	

Date	UT	Run no.	Aperture	Filter	Exposure	Gain	Total Frames	Frame Size X pixels Y pixels	Power- mate	Notes
22/3/05	17:51	096	30cm	V	off	6	5000	200 200	n	
"	17:55	097	"	V	1/120	7	5000	200 200	n	
"	17:59	098	"	V	1/250	8	5000	200 200	n	
"	18:05	099	"	V	1/500	10	5000	200 200	n	
"	18:09	100	"	V	1/1000	12	5000	200 200	n	
"	18:15	101	"	I	1/1000	14	5000	200 200	n	V. noisy & faint
"	18:19	102	"	I	1/500	14	5000	200 200	n	
"	18:23	103	"	I	1/250	12	5000	200 200	n	
"	18:27	104	"	I	1/120	10	5000	200 200	n	
"	18:32	105	"	I	off	7	5000	200 200	n	
ADS11005 (τ Ophuchi)										
AAT, camera 2										
25/6/05		063	80cm	R	off	8	10000	200 200	n	
"		064	80cm	R	1/120	6	10000	200 200	n	Defocussed
"		065	60cm	R	1/120	6	10000	200 200	n	Defocussed
"		066	40cm	R	1/120	7	10000	200 200	n	In focus
"		067	1m	R	1/120	5	10000	200 200		
Trapezium (Orion)										
ANU 1m, camera 1										
14/3/05	10:38	008	75cm	I	1/250	9	5000	160 220	n	
"	10:45	009	"	I	1/500	11	5000	160 220	n	
"	10:50	010	"	I	1/120	7	5000	160 220	n	
"	10:55	011	"	I	off	5	5000	160 220	n	
"	11:01	012	"	I	1/1000	13	5000	160 220	n	
"	11:26	013	30cm	I	1/250	13	5000	160 220	n	
"	11:31	014	"	I	1/120	9	5000	160 220	n	
"	11:35	015	"	I	off	7	5000	160 220	n	
15/3/05	10:13	007	30cm	I	1/250	11	5000	220 160	n	
"	10:18	008	"	I	1/120	9	5000	220 160	n	
"	10:22	009	"	I	off	7	5000	220 160	n	Cloud
"	10:23	010	"	V	off	5	5000	220 160	n	Cloud
20/3/05	9:59	022	30cm	I	off	11	5000	200 200	n	
"	10:05	023	"	I	1/120	9	5000	200 200	n	
22/3/05	10:07	019	30cm	I	off	7	5000	400 400	n	
"	10:11	020	"	I	1/120	9	5000	400 400	n	
"	10:15	021	"	I	1/250	12	5000	400 400	n	
"	10:20	022	"	V	1/250	12	5000	400 400	n	
"	10:25	023	"	V	1/120	10	5000	400 400	n	
"	10:30	024	"	V	off	7	5000	400 400	n	
23/3/05	9:30	001	30cm	I	off	6	5000	300 300	n	
"	9:34	002	"	I	1/120	7	5000	300 300	n	

Date	UT	Run no.	Aperture	Filter	Exposure	Gain	Total Frames	Frame Size X pixels Y pixels		Power- mate	Notes
"	9:38	003	"	I	1/250	8	5000	300	300	n	
"	9:43	004	"	I	1/500	9	5000	300	300	n	
ANU 1m, camera 2											
9/11/05	16:16	086	75cm	I	off	9	5000	400	400	y	
"	16:21	087	"	R	off	8	5000	400	400	y	
"	16:25	088	"	V	off	8	5000	400	400	y	
"	16:30	089	"	B	off	10	5000	400	400	y	
9/11/05	16:47	086	30cm	B	off	6	5000	400	400	n	
"	16:52	087	"	V	off	6	5000	400	400	n	
"	16:56	088	"	R	off	6	5000	400	400	n	
"	17:01	089	"	I	off	6	5000	400	400	n	
10/11/05	16:05	028	"	V	off	10	5000	200	200	n	
11/11/05	14:43	068	30cm	I	off	6	5000	200	200	n	
"	14:48	069	"	R	off	5	5000	200	200	n	
"	14:54	070	"	V	off	4	5000	200	200	n	
"	14:59	071	"	B	off	5	5000	200	200	n	
α Orionis (Rigel)											
ANU 1m, camera 2											
10/11/05	14:16	016	10cm	B	off	6	5000	200	200	n	8.4" seeing
"	14:21	017	"	V	off	5	5000	200	200	n	
"	14:16	018	"	R	off	4	5000	200	200	n	
"	14:33	019	"	I	off	6	5000	200	200	n	
"	14:50	020	20cm	B	off	4	5000	200	200	n	
"	14:56	021	"	V	off	2	5000	200	200	n	
"	15:03	022	"	R	off	1	5000	200	200	n	
"	15:08	023	"	I	off	1	5000	200	200	n	
"	15:18	024	30cm	I	off	1	5000	200	200	n	
"	15:26	025	"	R	1/120	0	5000	200	200	n	
"	15:33	026	"	V	1/120	0	5000	200	200	n	
"	15:39	027	"	B	off	0	5000	200	200	n	
η Orionis											
ANU 1m, camera 2											
11/11/05	16:25	086	30cm	V	off	4	5000	200	200	n	1.5" sep.
"	16:32	087	"	R	off	3	5000	200	200	n	
"	16:38	088	"	I	off	3	5000	200	200	n	
"	16:46	089	"	B	off	4	5000	200	200	n	
12/11/05	14:27	049	75cm	I	1/120	6	5000	200	200	y	focus drifted
"	14:36	050	"	R	1/120	4	5000	200	200	y	re-focussed
"	14:41	051	"	V	1/120	3	5000	200	200	y	
"	14:45	052	"	B	1/120	4	5000	200	200	y	
13/11/05	13:53	055	30cm	R	off	3	5000	200	200	n	

Date	UT	Run no.	Aperture	Filter	Exposure	Gain	Total Frames	Frame Size X pixels Y pixels	Power- mate	Notes
"	14:01	056	"	I	off	4	5000	200 200	n	
"	14:06	057	"	V	off	2	5000	200 200	n	
"	14:10	058	"	B	off	2	5000	200 200	n	
ζ Orionis										
ANU 1m, camera 2										
12/11/05	17:04	073	75cm	B	off	2	5000	300 300	y	
"	17:10	074	"	V	1/120	0	5000	300 300	y	
"	17:15	075	"	R	1/120	0	5000	300 300	y	
"	17:22	076	"	I	1/120	3	5000	300 300	y	
13/11/05	14:19	059	30cm	B	1/120	1	5000	200 200	n	
"	14:22	060	"	V	1/250	0	5000	200 200	n	
"	14:27	061	"	R	1/250	0	5000	200 200	n	
"	14:31	062	"	I	1/120	0	5000	200 200	n	
α Pheoniciis (Ankaa)										
ANU 1m, camera 2										
11/11/05	10:15	034	30cm	I	1/120	0	5000	200 200	n	2.8" seeing
"	10:20	035	"	R	1/250	0	5000	200 200	n	
"	10:26	036	"	V	1/120	0	5000	200 200	n	
"	10:32	037	"	B	off	3	5000	200 200	n	
12/11/05	10:36	019	30cm	I	1/250	0	5000	200 200	n	1.8" seeing
"	10:42	020	"	R	1/500	2	5000	200 200	n	
"	10:49	021	"	V	1/250	0	5000	200 200	n	
"	10:55	022	"	B	off	0	5000	200 200	n	
"	11:24	023	75cm	I	off	0	5000	200 200	y	1.9" seeing
"	11:28	024	"	I	1/120	0	5000	200 200	y	
"	11:35	025	"	I	1/250	2	5000	200 200	y	
"	11:41	026	"	I	1/500	5	5000	200 200	y	
"	11:47	027	"	I	1/1000	6	5000	200 200	y	
"	11:53	028	"	R	1/250	2	5000	200 200	y	
"	11:58	029	"	V	1/250	3	5000	200 200	y	
"	12:03	030	"	B	1/250	6	5000	200 200	y	
13/11/05	9:55	019	30cm	R	1/500	0	5000	200 200	n	
"	9:59	020	"	V	1/250	0	5000	200 200	n	
"	10:05	021	"	B	1/120	0	5000	200 200	n	
"	10:10	022	"	I	1/250	0	5000	200 200	n	
"	10:30	023	75cm	I	1/250	0	5000	200 200	y	
"	10:34	024	"	R	1/250	0	5000	200 200	y	
"	10:39	025	"	V	1/250	0	5000	200 200	y	
"	10:43	026	"	B	1/250	6	5000	200 200	y	
"	10:49	027	"	I	1/120	0	5000	200 200	y	
"	10:54	028	"	I	1/250	2	5000	200 200	y	

Date	UT	Run no.	Aperture	Filter	Exposure	Gain	Total Frames	Frame Size X pixels Y pixels		Power-mate	Notes
"	10:58	029	"	I	1/500	3	5000	200	200	y	
"	11:03	030	"	I	1/1000	5	5000	200	200	y	
"	11:22	031	1m	I	1/1000	0	5000	200	200	y	
"	11:26	032	"	I	1/500	0	5000	200	200	y	
"	11:31	033	"	I	1/250	0	5000	200	200	y	
"	11:36	034	"	R	1/500	0	5000	200	200	y	
"	11:41	035	"	V	1/500	0	5000	200	200	y	
"	11:45	036	"	B	1/500	0	5000	200	200	y	

θ Pictoris											
ANU 1m, camera 2											
11/11/05	15:50	080	30cm	I	off	9	5000	300	300	n	38" sep.
"	15:54	081	"	R	off	9	5000	300	300	n	
"	15:59	082	"	V	off	8	5000	300	300	n	
"	16:04	083	"	B	off	9	5000	300	300	n	

k Puppis											
ANU 1m, camera 1											
21/3/05	10:52	016	30cm	V	off	2	5000	200	200	n	
"	10:57	017	"	V	1/120	4	5000	200	200	n	
"	11:03	018	"	V	1/250	5	5000	200	200	n	
"	11:08	019	"	V	1/500	6	5000	200	200	n	
"	11:14	020	"	V	1/1000	8	5000	200	200	n	
"	11:21	021	"	I	1/1000	12	5000	200	200	n	V low SNR
"	11:25	022	"	I	1/500	12	5000	200	200	n	
"	11:30	023	"	I	1/250	11	5000	200	200	n	
"	11:37	024	"	I	1/120	7	5000	200	200	n	Seeing improved suddenly
"	11:42	025	"	I	off	5	5000	200	200	n	
"	11:48	026	"	B	off	5	5000	200	200	n	
"	11:53	027	"	B	1/120	6	5000	200	200	n	
"	11:58	028	"	B	1/250	7	5000	200	200	n	
"	12:04	029	"	B	1/500	8	5000	200	200	n	
"	12:09	030	"	B	1/1000	10	5000	200	200	n	
22/3/05	10:39	025	30cm	V	off	5	5000	200	200	n	
"	10:44	026	"	V	1/120	6	5000	200	200	n	
"	10:48	027	"	V	1/250	7	5000	200	200	n	
"	10:52	028	"	V	1/500	8	5000	200	200	n	
"	10:56	029	"	V	1/1000	9	5000	200	200	n	
"	11:04	030	"	I	1/1000	10	5000	200	200	n	V faint & noisy
"	11:07	031	"	I	1/500	10	5000	200	200	n	
"	11:11	032	"	I	1/250	9	5000	200	200	n	
"	11:16	033	"	I	1/120	8	5000	200	200	n	
"	11:20	034	"	I	off	6	5000	200	200	n	

Date	UT	Run no.	Aperture	Filter	Exposure	Gain	Total Frames	Frame Size X pixels Y pixels		Power- mate	Notes
23/3/05	10:47	013	75cm	I	off	4	5000	300	300	n	
"	10:52	014	"	I	1/120	5	5000	300	300	n	
"	10:56	015	"	I	1/250	7	5000	300	300	n	
"	11:00	016	"	I	1/500	9	5000	300	300	n	
"	11:06	017	"	V	1/500	7	5000	300	300	n	
"	11:10	018	"	V	1/250	6	5000	300	300	n	
"	11:15	019	"	V	1/120	5	5000	300	300	n	
"	11:19	020	"	V	off	3	5000	300	300	n	
06298-5014, SAO234538 (Puppis)											
ANU 1m, camera 2											
12/11/05	15:56	065	75cm	R	off	6	10000	200	200	y	
"	16:05	066	"	V	off	6	10000	200	200	y	
"	16:14	067	"	B	off	9	10000	200	200	y	
"	16:22	068	"	I	off	9	10000	200	200	y	
β Scorpii											
ANU 1m, camera 1											
14/3/05	18:30	070	30cm	I	1/120	2	5000	200	200	n	
"	18:33	071	"	I	off	2	5000	200	200	n	
"	18:38	072	"	I	1/250	5	5000	200	200	n	
"	18:43	073	"	I	1/500	7	5000	200	200	n	
"	18:49	074	"	V	1/500	5	5000	200	200	n	
"	18:53	075	"	V	1/250	3	5000	200	200	n	
"	18:57	076	"	V	1/120	2	5000	200	200	n	
"	19:02	077	"	V	off	1	5000	200	200	n	
15/3/05	17:13	050	75cm	V	1/1000	5	5000	200	300	n	
"	17:18	051	"	V	1/500	4	5000	200	300	n	
"	17:23	052	"	V	1/250	2	5000	200	300	n	
"	17:27	053	"	V	1/120	0	5000	200	300	n	
"	17:33	054	"	V	off	0	5000	200	300	n	
"	17:38	055	"	I	off	0	5000	200	300	n	
"	17:42	056	"	I	1/120	1	5000	200	300	n	
"	17:46	057	"	I	1/250	4	5000	200	300	n	
"	17:53	058	"	I	1/500	5	5000	200	300	n	
"	17:58	059	"	I	1/1000	9	5000	200	300	n	
19/3/05	16:52	052	30cm	V	off	0	5000	200	200	n	
"	16:56	053	"	V	1/120	1	5000	200	200	n	
"	17:02	054	"	V	1/250	3	5000	200	200	n	
"	17:06	055	"	V	1/500	4	5000	200	200	n	
"	17:25	056	"	V	1/1000	6	5000	200	200	n	
"	17:32	057	"	I	1/1000	8	5000	200	200	n	
"	17:37	058	"	I	1/500	7	5000	200	200	n	

Date	UT	Run no.	Aperture	Filter	Exposure	Gain	Total Frames	Frame Size		Power- mate	Notes
								X pixels	Y pixels		
	17:42	059	"	I	1/250	5	5000	200	200	n	
	17:47	060	"	I	1/120	4	5000	200	200	n	
	17:51	061	"	I	off	2	5000	200	200	n	
20/3/05	17:10	065	30cm	I	off	4	5000	200	200	n	
	17:16	066	"	I	1/120	5	5000	200	200	n	
	17:20	067	"	I	1/250	6	5000	200	200	n	
	17:25	068	"	I	1/500	7	5000	200	200	n	
	17:32	069	"	I	1/1000	9	5000	200	200	n	
	17:37	070	"	V	1/1000	9	5000	200	200	n	
	17:42	071	"	V	1/500	7	5000	200	200	n	
	17:48	072	"	V	1/250	5	5000	200	200	n	
	17:52	073	"	V	1/120	3	5000	200	200	n	
	17:56	074	"	V	off	2	5000	200	200	n	
20/3/05	18:05	075	20cm	V	off	2	5000	200	200	n	
	18:09	076	"	V	1/120	3	5000	200	200	n	
	18:15	077	"	V	1/250	5	5000	200	200	n	
	18:19	078	"	V	1/500	6	5000	200	200	n	
	18:24	079	"	V	1/1000	7	5000	200	200	n	
	18:42	080	"	I	1/1000	12	5000	200	200	n	
	18:52	081	"	I	1/500	12	5000	200	200	n	
	18:56	082	"	I	1/250	9	5000	200	200	n	
	19:00	083	"	I	1/120	7	5000	200	200	n	
	19:04	084	"	I	off	5	5000	200	200	n	
21/3/05	15:53	060	"	I	off	4	5000	200	200	n	
	15:57	061	"	I	1/120	5	5000	200	200	n	
	16:02	062	"	I	1/250	6	5000	200	200	n	
	16:08	063	"	I	1/500	8	5000	200	200	n	
	16:14	064	"	I	1/1000	10	5000	200	200	n	
	16:21	065	"	V	1/1000	8	5000	200	200	n	
	16:26	066	"	V	1/500	6	5000	200	200	n	
	16:31	067	"	V	1/250	5	5000	200	200	n	
	16:35	068	"	V	1/120	3	5000	200	200	n	
	16:39	069	"	V	off	2	5000	200	200	n	
	16:48	070	30cm	V	off	2	5000	200	200	n	
	16:52	071	"	V	1/120	3	5000	200	200	n	
	16:58	072	"	V	1/250	4	5000	200	200	n	
	17:04	073	"	V	1/500	5	5000	200	200	n	
	17:08	074	"	V	1/1000	6	5000	200	200	n	
	17:14	075	"	I	1/1000	7	5000	200	200	n	
	17:17	076	"	I	1/500	6	5000	200	200	n	
	17:22	077	"	I	1/250	5	5000	200	200	n	
	17:26	078	"	I	1/120	3	5000	200	200	n	
	17:31	079	"	I	off	2	5000	200	200	n	

Date	UT	Run no.	Aperture	Filter	Exposure	Gain	Total Frames	Frame Size		Power- mate	Notes
								X pixels	Y pixels		
22/3/05	16:57	086	30cm	I	off	15	5000	200	200	n	
"	17:02	087	"	I	1/120	5	5000	200	200	n	
"	17:07	088	"	I	1/250	6	5000	200	200	n	
"	17:12	089	"	I	1/500	7	5000	200	200	n	
"	17:18	090	"	I	1/1000	9	5000	200	200	n	
"	17:24	091	"	V	1/1000	9	5000	200	200	n	
"	17:28	092	"	V	1/500	7	5000	200	200	n	
"	17:32	093	"	V	1/250	5	5000	200	200	n	
"	17:37	094	"	V	1/120	3	5000	200	200	n	
"	17:42	095	"	V	off	1	5000	200	200	n	
ε Scorpii											
ANU 1m, camera 1											
15/3/05	16:46	049	75cm	V	1/250	7	5000	200	200	n	
γ Sextantis											
ANU 1m, camera 1											
18/3/05	14:13	011	30cm	V	off	5	5000	200	200	n	
"	14:18	012	"	V	1/120	6	5000	200	200	n	
"	14:22	013	"	V	1/250	9	5000	200	200	n	
δ Velorum											
Macquarie 40cm, camera 1											
8/3/05		003	40cm	G	1/1000	3	10000	300	250	n	
"		004	"	G	1/250	0	10000	300	250	n	Too bright
γ Velorum											
ANU 1m, camera 1											
14/3/05	11:46	016	30cm	I	off	5	5000	250	250	n	
"	11:51	017	"	I	1/120	1	5000	250	250	n	
"	12:57	018	"	I	1/250	4	5000	250	250	n	
"	13:02	019	"	I	1/500	4	5000	250	250	n	
"	13:18	020	"	I	1/1000	6	5000	250	250	n	
"	13:23	021	"	V	1/1000	3	5000	250	250	n	
"	13:27	022	"	V	1/500	0	5000	250	250	n	
"	13:34	023	"	V	1/250	4	5000	250	250	n	
"	13:39	024	"	V	1/120	3	5000	250	250	n	
"	13:45	025	"	V	off	0	5000	250	250	n	
20/3/05	10:25	024	30cm	I	off	3	5000	200	200	n	
"	10:31	025	"	I	1/120	3	5000	200	200	n	
"	10:35	026	"	I	1/250	4	5000	200	200	n	
"	10:40	027	"	I	1/500	5	5000	200	200	n	
"	10:47	028	"	I	1/1000	7	5000	200	200	n	

Date	UT	Run no.	Aperture	Filter	Exposure	Gain	Total Frames	Frame Size X pixels Y pixels		Power- mate	Notes
"	10:54	029	"	V	1/1000	5	5000	200	200	n	
"	10:58	030	"	V	1/500	4	5000	200	200	n	
"	11:03	031	"	V	1/250	2	5000	200	200	n	
"	11:09	032	"	V	1/120	1	5000	200	200	n	
"	11:14	033	"	V	off	0	5000	200	200	n	
21/3/05	9:40	006	30cm	I	off	1	5000	250	250	n	
"	9:46	007	"	I	1/120	3	5000	250	250	n	
"	9:50	008	"	I	1/250	5	5000	250	250	n	
"	9:56	009	"	I	1/500	6	5000	250	250	n	
"	10:01	010	"	I	1/1000	7	5000	250	250	n	
"	10:10	011	"	V	1/1000	4	5000	250	250	n	
"	10:17	012	"	V	1/500	2	5000	250	250	n	
"	10:21	013	"	V	1/250	1	5000	250	250	n	
"	10:26	014	"	V	1/120	0	5000	250	250	n	
"	10:30	015	"	V	off	0	5000	250	250	n	
22/3/05	13:15	051	30cm	I	off	2	5000	300	300	n	
"	13:19	052	"	I	1/120	3	5000	300	300	n	
"	13:23	053	"	I	1/250	4	5000	300	300	n	
"	13:27	054	"	I	1/500	5	5000	300	300	n	
"	13:31	055	"	I	1/1000	6	5000	300	300	n	
"	13:36	056	"	V	1/1000	5	5000	300	300	n	
"	13:41	057	"	V	1/500	4	5000	300	300	n	
"	13:45	058	"	V	1/250	3	5000	300	300	n	
"	13:49	059	"	V	1/120	1	5000	300	300	n	
"	13:57	060	"	V	off	0	5000	300	300	n	
ANU 1m, camera 2											
11/11/05	17:24	094	30cm	I	off	0	5000	200	200	n	
"	17:29	095	"	R	1/120	0	5000	200	200	n	
"	17:34	096	"	V	1/250	0	5000	200	200	n	
"	17:39	097	"	B	1/120	0	5000	200	200	n	

λ Velorum
ANU 1m, camera 1

20/3/05	12:40	036	30cm	I	off	0	5000	200	200	n	
"	12:45	037	"	I	1/120	1	5000	200	200	n	
"	12:50	038	"	I	1/250	2	5000	200	200	n	
"	12:55	039	"	I	1/500	4	5000	200	200	n	
"	13:00	040	"	I	1/1000	5	5000	200	200	n	
"	13:05	041	"	V	1/1000	7	5000	200	200	n	
"	13:13	042	"	V	1/500	6	5000	200	200	n	
"	13:18	043	"	V	1/250	4	5000	200	200	n	
"	13:23	044	"	V	1/120	3	5000	200	200	n	
"	13:28	045	"	V	off	2	5000	200	200	n	

Date	UT	Run no.	Aperture	Filter	Exposure	Gain	Total Frames	Frame Size X pixels Y pixels	Power- mate	Notes
21/3/05	13:43	046	20cm	V	off	2	5000	200 200	n	
	13:45	047	"	V	1/120	3	5000	200 200	n	
	13:50	048	"	V	1/250	4	5000	200 200	n	
	13:54	049	"	V	1/500	6	5000	200 200	n	
	14:00	050	"	V	1/1000	9	5000	200 200	n	
	15:23	051	"	I	1/1000	8	5000	200 200	n	
	15:28	052	"	I	1/500	6	5000	200 200	n	
	15:37	053	"	I	1/250	5	5000	200 200	n	
	15:42	054	"	I	1/120	4	5000	200 200	n	
	15:54	055	"	I	off	3	5000	200 200	n	
	16:00	056	"	I	off	1	5000	200 200	n	
	12:27	031	30cm	I	1/250	0	5000	200 200	n	
	12:31	032	"	I	1/500	1	5000	200 200	n	
	12:36	033	"	I	1/1000	3	5000	200 200	n	
	12:42	034	"	V	1/1000	4	5000	200 200	n	
	12:46	035	"	V	1/500	3	5000	200 200	n	
12:52	036	"	V	1/250	2	5000	200 200	n		
12:56	037	"	V	1/120	1	5000	200 200	n		
ψ Velorum										
ANU 1m, camera 2										
12/11/05	17:32	077	75cm	I	off	5	5000	300 300	y	
"	17:39	078	"	R	off	3	5000	300 300	y	
"	17:44	079	"	V	off	3	5000	300 300	y	
SRS 1167 (Vela)										
AAT, camera 2										
25/6/05										seeing 1.3"
γ Virginis										
ANU 1m, camera 2										
18/3/05	16:37	031	30cm	I	1/120	4	5000	200 200	n	
"	16:42	032	"	I	1/250	6	5000	200 200	n	
"	16:46	033	"	I	1/500	7	5000	200 200	n	
"	16:52	034	"	I	1/1000	8	5000	200 200	n	
"	16:56	035	"	I	off	3	5000	200 200	n	
"	17:01	036	"	V	off	4	5000	200 200	n	Saturated
"	17:10	037	"	V	off	3	5000	200 200	n	
"	17:15	038	"	V	1/120	4	5000	200 200	n	
"	17:20	039	"	V	1/250	5	5000	200 200	n	
"	17:25	040	"	V	1/500	6	5000	200 200	n	
"	17:30	041	"	V	1/1000	7	5000	200 200	n	
19/3/05	14:48	032	20cm	V	off	2	5000	200 200	n	

Date	UT	Run no.	Aperture	Filter	Exposure	Gain	Total Frames	Frame Size X pixels Y pixels		Power- mate	Notes
”	14:54	033	”	V	1/120	4	5000	200	200	n	Cloud
”	14:59	034	”	V	1/250	5	5000	200	200	n	
”	15:05	035	”	V	1/500	6	5000	200	200	n	
”	15:11	036	”	V	1/1000	7	5000	200	200	n	
”	15:19	037	”	I	1/1000	10	5000	200	200	n	
”	15:24	038	”	I	1/500	8	5000	200	200	n	
”	15:35	039	”	I	1/250	7	5000	200	200	n	
”	15:39	040	”	I	1/120	6	5000	200	200	n	
”	15:45	041	”	I	off	4	5000	200	200	n	
”	15:57	042	30cm	I	off	2	5000	200	200	n	
”	16:02	043	”	I	1/120	3	5000	200	200	n	
”	16:07	044	”	I	1/250	4	5000	200	200	n	
”	16:11	045	”	I	1/500	5	5000	200	200	n	
”	16:16	046	”	I	1/1000	7	5000	200	200	n	
”	16:22	047	”	V	1/1000	6	5000	200	200	n	
”	16:26	048	”	V	1/500	5	5000	200	200	n	
”	16:32	049	”	V	1/250	4	5000	200	200	n	
”	16:36	050	”	V	1/120	3	5000	200	200	n	
”	16:41	051	”	V	off	1	5000	200	200	n	
ADS 9392 (Virgo)											
AAT, camera 2											
25/6/05		062	0.8m	R	off	9	10000	200	200	n	Cloudy, poor seeing.
MOON											
Agrippa & Godin											
ANU 1m, camera 2											
9/11/05	8:58	031	30cm	R	off	0	3000	768	576	n	
Appenines											
ANU 1m, camera 1											
16/3/05	11:24	011	75cm	I	1/250	6	3000	768	576	n	
Aristotle & Eudoxus											
ANU 1m, camera 1											
16/3/05	11:45	012	75cm	I	1/250	6	3000	768	576	n	
Cassini											
ANU 1m, camera 1											
20/3/05	8:50	014	75cm	I	off	4	3000	768	576	n	
ANU 1m, camera 2											
9/11/05	9:12	032	30cm	R	off	2	3000	768	576	n	

Date	UT	Run no.	Aperture	Filter	Exposure	Gain	Total Frames	Frame Size X pixels Y pixels	Power- mate	Notes
”	9:14	033	”	V	off	2	3000	768 576	n	
”	9:18	034	”	B	off	5	3000	768 576	n	
Clavius										
ANU 1m, camera 2										
10/11/05	13:37	001	30cm	R	off	2	3000	768 576	n	Very poor seeing
11/11/05	9:32	028	”	R	off	0	3000	768 576	n	
”	9:34	029	”	V	off	0	3000	768 576	n	
”	9:38	030	”	B	off	4	3000	768 576	n	
12/11/05	9:37	013	”	B	off	3	4000	768 576	n	
”	9:43	014	”	V	off	0	4000	768 576	n	
”	9:48	015	”	R	1/120	1	4000	768 576	n	
Copernicus										
ANU 1m, camera 1										
21/3/05	11:39	035	30cm	I	1/250	5	3000	768 576	n	
23/3/05	11:33	022	75cm	V	1/120	3	3000	768 576	n	
”	11:37	023	”	V	1/120	3	3000	768 576	n	
ANU 1m, camera 2										
11/11/05	9:12	024	30cm	R	1/120	2	3000	768 568	n	not full frame!
”	9:19	025	”	V	off	2	3000	768 568	n	
”	9:22	026	”	B	off	5	3000	768 568	n	
”	9:26	027	”	R	off	2	3000	768 568	n	
Eratosthenes										
ANU 1m, camera 2										
10/11/05	13:41	002	30cm	R	off	2	3000	768 576	n	Very poor seeing
Gassendi										
ANU 1m, camera 2										
13/11/05	9:19	016	30cm	V	1/120	2	3000	768 576	n	
”	9:24	017	”	B	off	3	3000	768 576	n	
”	9:29	018	”	R	1/120	0	3000	768 576	n	
Gruenberger										
ANU 1m, camera 2										
9/11/05	9:32	035	30cm	B	off	5	3000	768 576	n	
”	9:35	036	”	V	off	2	3000	768 576	n	
”	9:37	037	”	R	off	2	3000	768 576	n	
Hainzel										
ANU 1m, camera 1										
21/3/05	9:10	005	30cm	I	off	3	3000	768 576	n	Cloud

Date	UT	Run no.	Aperture	Filter	Exposure	Gain	Total Frames	Frame Size X pixels Y pixels	Power- mate	Notes
ANU 1m, camera 2										
12/11/05	9:11	010	”	R	off	0	4000	768 576	n	
12/11/05	9:22	011	”	V	off	1	4000	768 576	n	
12/11/05	9:26	012	”	B	off	4	4000	768 576	n	
Kepler										
ANU 1m, camera 1										
21/3/05	11:46	037	30cm	I	1/250	5	3000	768 576	n	
Macrobius										
ANU 1m, camera 1										
20/3/05	9:07	016	75cm	I	off	3	3000	768 576	n	
Montes Caucasus										
ANU 1m, camera 1										
16/3/05	11:08	009	75cm	I	1/120	3	3000	768 576	n	
”	11:14	010	”	I	1/250	6	3000	768 576	n	
Plato										
ANU 1m, camera 1										
21/3/05	11:43	036	30cm	I	1/250	5	3000	768 576	n	
ANU 1m, camera 2										
10/11/05	12:44	003	30cm	R	off	2	3000	768 576	n	Very poor seeing
12/11/05	10:01	016	30cm	R	1/120	2	4000	768 576	n	
”	10:05	017	”	V	1/120	3	4000	768 576	n	
”	10:10	018	”	B	off	3	4000	768 576	n	
Plinius										
ANU 1m, camera 1										
20/3/05	9:01	015	75cm	I	off	4	3000	768 576	n	Cloud
Posidonius										
ANU 1m, camera 1										
16/3/05	8:22	007	75cm	I	off	5	3000	768 576	y	High thin cloud, V high drift, manual guiding
”	8:25	008	”	I	off	5	3000	768 576	y	
Tycho										
ANU 1m, camera 1										
20/3/05	8:44	013	75cm	I	off	4	3000	768 576	n	
ANU 1m, camera 2										
11/11/05	9:41	031	30cm	B	off	4	3000	768 576	n	
”	9:45	032	”	V	off	0	3000	768 576	n	
”	9:48	033	”	R	off	0	3000	768 576	n	

Date	UT	Run no.	Aperture	Filter	Exposure	Gain	Total Frames	Frame Size X pixels Y pixels	Power- mate	Notes
Unidentified Lunar region 1										
ANU 1m, camera 1										
23/3/05	11:24	021	75cm	V	1/120	3	3000	768 576	n	
Unidentified Lunar region 2										
AAT, camera 2										
25/6/05	11:24	068	1m	R	1/120	AGC	2000	768 576	n	
MERCURY										
ANU 1m, camera 2										
9/11/05	8:07	021	30cm	I	1/120	0	3000	200 200	n	
"	8:11	022	"	R	1/250	0	3000	200 200	n	
"	8:16	023	"	V	1/120	0	3000	200 200	n	
"	8:19	024	"	B	off	0	3000	200 200	n	
11/11/05	8:20	015	30cm	I	1/120	0	5000	200 200	n	
"	8:24	016	"	R	1/120	0	5000	200 200	n	
"	8:29	017	"	V	1/120	2	5000	200 200	n	
"	8:35	018	"	B	off	3	5000	200 200	n	
12/11/05	8:21	001	30cm	R	1/120	0	5000	200 200	n	
"	8:25	002	"	V	1/120	0	5000	200 200	n	
"	8:31	003	"	B	off	2	5000	200 200	n	
"	8:36	004	"	I	1/121	1	5000	200 200	n	
13/11/05	8:23	006	30cm	I	1/120	0	5000	200 200	n	
"	8:27	007	"	R	1/120	0	5000	200 200	n	
"	8:31	008	"	V	1/120	0	5000	200 200	n	
"	8:35	009	"	B	off	2	5000	200 200	n	
VENUS										
ANU 1m, camera 2										
9/11/05	8:29	025	30cm	U	off	4	3000	300 300	n	Cloud structure visible
"	8:32	026	"	B	1/250	0	3000	300 300	n	no " " "
"	8:36	027	"	V	1/1000	0	3000	300 300	n	
"	8:38	028	"	R	1/1001	0	3000	300 300	n	
"	8:41	029	"	I	1/500	0	3000	300 300	n	
"	8:48	030	"	U	off	4	3000	300 300	n	Cloud structure visible
11/11/05	8:44	019	"	U	OFF	5	5000	300 300	n	
"	8:49	020	"	B	1/250	0	5000	300 300	n	
"	8:54	021	"	V	1/1000	0	5000	300 300	n	
"	8:59	022	"	R	1/1000	0	5000	300 300	n	
"	9:03	023	"	I	1/500	0	5000	300 300	n	
12/11/05	8:42	005	"	U	off	5	5000	300 300	n	
"	8:46	006	"	B	1/250	0	5000	300 300	n	
"	8:51	007	"	V	1/1000	0	5000	300 300	n	

Date	UT	Run no.	Aperture	Filter	Exposure	Gain	Total Frames	Frame Size		Power- mate	Notes
								X pixels	Y pixels		
	8:55	008	"	R	1/1000	0	5000	300	300	n	
	9:00	009	"	I	1/500	0	5000	200	200	n	
13/11/05	8:42	010	"	U	off	5	5000	300	300	n	
	8:46	011	"	B	1/250	0	5000	300	300	n	
	8:50	012	"	V	1/1000	0	5000	300	300	n	
	8:55	013	"	R	1/1000	0	5000	300	300	n	
	9:01	014	"	I	1/500	0	5000	300	300	n	
	9:07	015	"	U	off	5	5000	300	300	n	

MARS

ANU 1m, camera 1

14/3/05	18:15	69	30cm	I	1/120	3	5000	200	200	n	
"	19:12	78	"	V	1/120	3	1000	400	400	n	
"	19:18	79	"	I	1/120	3	1000	400	400	n	
19/3/05	18:05	62	30cm	I	1/120	3	5000	400	400	n	
"	18:11	63	"	R	1/120	2	5001	401	401	n	
"	18:15	64	"	V	1/120	4	5000	400	400	n	
"	18:21	65	"	B	1/120	7	5000	400	400	n	
21/3/05	18:30	90	30cm	V	1/120	4	5000	200	200	n	
"	18:37	91	"	B	off	5	5000	200	200	n	
"	18:42	92	"	R	off	1	5000	200	200		
"	18:47	93	"	I	off	1	5000	200	200	n	
22/3/05	18:38	106	30cm	I	off	7	5000	400	400	n	
"	18:43	107	"	R	off	5	5000	400	400	n	
"	18:48	108	"	V	off	6	5000	400	400	n	
"	18:53	109	"	B	off	8	5000	400	400	n	

ANU 1m, camera 2

9/11/05	11:42	046	75cm	I	off	0	3000	400	400	y	
"	11:48	047	"	R	off	0	3000	400	400	y	
"	11:52	048	"	V	off	2	3000	400	400	y	
"	11:56	049	"	B	off	6	3000	400	400	y	
"	12:00	050	"	U	off	14	3000	400	400	y	
"	12:13	051	30cm	I	off	0	3000	200	200	n	
"	12:17	052	"	I	off	0	5000	200	200	n	
"	12:22	053	"	R	1/120	0	5000	200	200	n	
"	12:27	054	"	V	off	5	5000	200	200	n	
"	12:33	055	"	B	off	14	5000	200	200	n	
"	13:06	058	"	B	off	5	3000	200	200	n	
"	13:11	059	"	V	off	0	5000	200	200	n	
"	13:16	060	"	R	1/120	0	5000	200	200	n	
"	13:21	061	"	I	off	0	5000	200	200	n	
"	13:26	062	"	I	1/120	2	5000	200	200	n	
"	13:31	063	"	R	1/120	2	5000	200	200	n	

changed focus

Date	UT	Run no.	Aperture	Filter	Exposure	Gain	Total Frames	Frame Size		Power- mate	Notes
								X pixels	Y pixels		
"	13:36	064	"	V	1/120	3	5000	200	200	n	
"	13:41	065	"	B	1/120	7	5000	200	200	n	
"	13:46	066	"	B	1/250	9	5000	200	200	n	
"	13:52	067	"	V	1/250	5	5000	200	200	n	
"	13:59	068	"	R	1/250	3	5000	200	200	n	
"	14:01	069	"	I	1/250	3	5000	200	200	n	
"	15:28	078	75cm	I	off	2	5000	400	400	y	
"	15:33	079	"	R	off	0	5000	400	400	y	
"	15:37	080	"	V	off	2	5000	400	400	y	
"	15:42	081	"	B	off	6	5000	400	400	y	
"	15:49	082	"	B	1/120	8	5000	400	400	y	
"	15:53	083	"	V	1/120	4	5000	400	400	y	
"	15:58	084	"	R	1/120	3	5000	400	400	y	
"	16:03	085	"	I	1/120	4	5000	400	400	y	
"	12:52	004	30cm	I	off	0	3000	200	200	n	V V poor seeing
"	12:56	005	"	R	off	0	3000	200	200	n	
"	12:58	006	"	V	1/120	0	3000	200	200	n	
"	13:02	007	"	B	off	5	3000	200	200	n	"
"	12:12	008	20cm	B	off	6	3000	250	250	n	VVV poor seeing
"	13:16	009	"	V	off	3	3000	250	250	n	
"	13:21	010	"	R	off	1	3000	250	250	n	
"	13:26	011	"	I	off	2	3000	250	250	n	
"	13:41	012	10cm	I	off	5	3000	250	250	n	see more structure!
"	13:45	013	"	R	off	5	3000	250	250	n	
"	13:50	014	"	V	off	6	3000	250	250	n	
"	13:56	015	"	B	off	11	3000	250	250	n	
11/11/2005	11:28	044	30cm	I	off	0	5000	200	200	n	
"	11:34	045	"	R	1/120	1	5000	200	200	n	
"	11:39	046	"	V	off	0	5000	200	200	n	
"	11:49	047	"	B	off	5	5000	200	200	n	
"	13:18	056	"	B	off	5	5000	200	200	n	
"	13:25	057	"	V	off	0	5000	200	200	n	
"	13:30	058	"	R	1/120	0	5000	200	200	n	
"	13:36	059	"	I	off	0	5000	200	200	n	
"	15:08	072	"	B	off	5	5000	200	200	n	
"	15:13	073	"	V	off	0	5000	200	200	n	
"	15:17	074	"	R	1/120	0	5000	200	200	n	
"	15:22	075	"	I	off	0	5000	200	200	n	
"	15:27	076	"	B	off	5	5000	200	200	n	
"	15:31	077	"	V	off	0	5000	200	200	n	
"	15:36	078	"	R	1/120	0	5000	200	200	n	
"	15:41	079	"	I	off	0	5000	200	200	n	
12/11/05	12:12	031	75cm	I	1/120	4	5000	400	400	y	

Date	UT	Run no.	Aperture	Filter	Exposure	Gain	Total Frames	Frame Size X pixels Y pixels		Power- mate	Notes
"	12:17	032	"	R	1/120	3	5000	400	400	y	
"	12:23	033	"	V	1/120	4	5000	400	400	y	
"	12:27	034	"	B	1/120	8	5000	400	400	y	
"	12:31	035	"	B	1/120	8	5000	400	400	y	
"	12:36	036	"	V	1/120	4	5000	400	400	y	
"	12:40	037	"	R	1/120	3	5000	400	400	y	
"	12:45	038	"	I	1/120	4	5000	400	400	y	
"	14:04	045	"	I	1/120	4	5000	400	400	y	
"	14:09	046	"	R	1/120	3	5000	400	400	y	
"	14:14	047	"	V	1/120	4	5000	400	400	y	
"	14:18	048	"	B	1/120	8	5000	400	400	y	
"	14:54	053	"	I	1/120	4	5000	400	400	y	
"	14:59	054	"	R	1/120	3	5000	400	400	y	
"	15:03	055	"	V	1/120	4	5000	400	400	y	
"	15:07	056	"	B	1/120	8	5000	400	400	y	
"	15:11	057	"	B	1/120	8	5000	400	400	y	
"	15:15	058	"	V	1/120	4	5000	400	400	y	
"	15:20	059	"	R	1/120	3	5000	400	400	y	
"	15:24	060	"	I	1/120	4	5000	400	400	y	
"	15:28	061	"	I	1/120	4	5000	400	400	y	
"	15:32	062	"	R	1/120	3	5000	400	400	y	
"	15:36	063	"	V	1/120	4	5000	400	400	y	
"	15:40	064	"	B	1/120	8	5000	400	400	y	
13/11/05	11:54	037	1m	I	1/120	1	5000	400	400	y	
"	11:58	038	"	R	1/120	1	5000	400	400	y	
"	12:03	039	"	V	1/120	2	5000	400	400	y	
"	12:07	040	"	B	1/120	5	5000	400	400	y	
"	12:17	041	75cm	B	1/120	7	5000	400	400	y	
"	12:22	042	"	V	1/120	4	5000	400	400	y	
"	12:26	043	"	R	1/120	3	5000	400	400	y	
"	12:31	044	"	I	1/120	3	5000	400	400	y	
"	12:45	045	30cm	I	1/120	3	5000	200	200	n	
"	12:49	046	"	R	1/120	2	5000	200	200	n	
"	12:53	047	"	V	1/120	3	5000	200	200	n	
"	12:58	048	"	B	1/120	6	5000	200	200	n	
"	13:05	049	"	B	1/120	6	5000	200	200	n	
"	13:10	050	"	V	1/120	3	5000	200	200	n	
"	13:14	051	"	R	1/120	2	5000	200	200	n	
"	13:19	052	"	I	1/120	3	5000	200	200	n	
"	14:37	063	30cm	I	1/120	3	5000	200	200	n	
"	14:41	064	"	R	1/120	2	5000	200	200	n	
"	14:46	065	"	V	1/120	3	5000	200	200	n	
"	14:50	066	"	B	1/120	6	5000	200	200	n	

Date	UT	Run no.	Aperture	Filter	Exposure	Gain	Total Frames	Frame Size		Power- mate	Notes
								X pixels	Y pixels		
JUPITER											
ANU 1m, camera 1											
14/3/05	12:48	026	30cm	V	1/120	5	5000	400	400	n	
"	12:51	027	"	R	1/120	5	5000	400	400	n	
"	12:57	028	"	B	1/120	8	5000	400	400	n	
"	13:02	029	"	I	1/120	6	5000	400	400	n	
"	13:18	030	75cm	I	1/120	4	5000	400	400	n	
"	13:23	031	"	R	1/120	3	5000	400	400	n	
"	13:27	032	"	V	1/120	3	5000	400	400	n	
"	13:34	033	"	V	1/120	3	5000	400	400	n	
"	13:39	034	"	R	1/120	3	5000	400	400	n	Changed focus.
"	13:45	035	"	I	1/120	4	5000	400	400	n	
"	13:48	036	"	B	1/120	5	5000	400	400	n	
"	13:52	037	"	B	1/120	5	1000	400	400	n	
"	13:53	038	"	V	1/120	2	1000	400	400	n	
"	13:54	039	"	R	1/120	2	1000	400	400	n	
"	13:56	040	"	I	1/120	3	1000	400	400	n	
"	15:59	057	30cm	V	1/120	5	5000	400	400	n	
"	16:02	058	"	R	1/120	5	5000	400	400	n	
"	16:07	059	"	I	1/120	6	5000	400	400	n	
"	16:12	060	"	B	1/120	8	5000	400	400	n	
"	17:09	063	"	I	1/120	6	5000	400	400	n	
"	17:27	064	"	I	1/120	6	10000	400	400	n	
15/3/05	12:13	011	30cm	I	1/120	6	5000	400	400	n	
"	12:18	012	"	R	1/120	5	5000	400	400	n	
"	12:29	013	"	V	1/120	5	5000	400	400	n	
"	12:43	014	"	B	1/120	8	5000	400	400	n	
"	12:51	015	"	I	1/120	6	10000	400	400	n	
"	12:58	016	"	I	1/120	6	10000	400	400	n	
"	13:05	017	"	I	1/120	6	10000	400	400	n	
"	13:11	018	"	I	1/120	6	10000	400	400	n	
"	13:18	019	"	I	1/120	6	10000	400	400	n	
"	13:25	020	"	I	1/120	6	10000	400	400	n	
"	13:32	021	"	I	1/120	6	10000	400	400	n	
"	13:38	022	"	I	1/120	6	10000	400	400	n	
"	13:45	023	"	I	1/120	6	10000	400	400	n	
"	13:52	024	"	I	1/120	6	10000	400	400	n	
"	13:59	025	"	I	1/120	6	10000	400	400	n	
"	14:06	026	"	I	1/120	6	10000	400	400	n	
"	14:12	027	"	I	1/120	6	10000	400	400	n	
"	14:19	028	"	I	1/120	6	10000	400	400	n	
"	14:26	029	"	I	1/120	6	10000	400	400	n	
"	14:33	030	"	I	1/120	6	10000	400	400	n	

Date	UT	Run no.	Aperture	Filter	Exposure	Gain	Total Frames	Frame Size		Power- mate	Notes
								X pixels	Y pixels		
"	14:39	031	"	I	1/120	6	10000	400	400	n	
"	14:46	032	"	I	1/120	6	10000	400	400	n	
"	15:04	033	75cm	I	1/120	4	5000	400	400	n	Changed focus
"	15:07	034	"	R	1/120	3	5000	400	400	n	
"	15:08	035	"	V	1/120	3	5000	400	400	n	
"	15:09	036	"	B	1/120	5	5000	400	400	n	
"	15:25	037	"	I	off	5	3000	768	576	y	5000 too big.
"	15:33	038	"	R	off	4	3000	768	576	y	
"	15:36	039	"	V	off	4	3000	768	576	y	
"	15:39	040	"	B	off	6	3000	768	576	y	
18/3/05	16:00	027	30cm	I	1/120	6	5000	400	400	n	
"	16:05	028	"	R	1/120	5	5000	400	400	n	
"	16:11	029	"	V	1/120	5	5000	400	400	n	
"	16:21	030	"	B	1/120	7	5000	400	400	n	
19/3/05	13:46	024	75cm	V	off	2	5000	400	400	n	
"	13:53	025	"	B	off	5	5000	400	400	n	
"	14:02	026	"	R	1/120	3	5000	400	400	n	
"	14:08	027	"	I	1/120	5	5000	400	400	n	
"	14:22	028	20cm	I	1/120	7	5000	400	400	n	
"	14:26	029	"	R	1/120	6	5000	400	400	n	
"	14:30	030	"	V	1/120	6	5000	400	400	n	
"	14:35	031	"	B	1/120	8	5000	400	400	n	
20/3/05	11:59	034	30cm	I	1/120	5	5000	400	400	n	
"	12:05	035	"	R	1/120	5	5000	400	400	n	Very cloudy.
"	16:55	057	20cm	I	off	6	5000	400	400	n	
"	16:22	058	"	R	off	4	5000	400	400	n	
"	16:31	059	"	V	off	4	5000	400	400	n	
"	16:37	060	"	B	off	6	5000	400	400	n	
"	16:46	061	30cm	B	off	6	5000	400	400	n	
"	16:52	062	"	V	off	4	5000	400	400	n	
"	16:56	063	"	R	1/120	4	5000	400	400	n	
"	7:02	064	"	I	off	4	5000	400	400	n	
21/3/05	13:14	038	30cm	I	1/120	6	5000	400	400	n	
"	13:19	039	"	R	1/120	5	5000	400	400	n	
"	13:28	040	"	V	1/120	5	5000	400	400	n	
"	13:33	041	"	B	off	6	5000	400	400	n	
"	14:57	052	30cm	I	off	4	5000	400	400	n	
"	15:05	053	"	R	off	3	5000	400	400	n	
"	15:10	054	"	V	off	3	5000	400	400	n	
"	15:06	055	"	B	off	5	5000	400	400	n	
"	15:26	056	20cm	B	off	7	5000	400	400	n	
"	15:32	057	"	V	off	5	5000	400	400	n	
"	15:37	058	"	R	off	5	5000	400	400	n	

Date	UT	Run no.	Aperture	Filter	Exposure	Gain	Total Frames	Frame Size		Power- mate	Notes
								X pixels	Y pixels		
22/3/05	15:44	059	"	I	off	6	5000	400	400	n	
	12:46	047	30cm	I	1/120	6	5000	400	400	n	
	12:50	048	"	R	1/120	5	5000	400	400	n	
	12:55	049	"	V	1/120	5	5000	400	400	n	
22/3/05	13:01	050	"	B	off	6	5000	400	400	n	
	14:05	061	30cm	I	off	5	10000	400	400	n	
	14:11	062	"	I	off	5	10000	400	400	n	
	14:16	063	"	I	off	5	10000	400	400	n	
	14:21	064	"	I	off	5	10000	400	400	n	
	14:25	065	"	I	off	5	10000	400	400	n	
	14:28	066	"	I	off	5	10000	400	400	n	
	14:35	067	"	I	off	5	10000	400	400	n	
	14:42	068	"	I	off	5	10000	400	400	n	
	14:49	069	"	I	off	5	10000	400	400	n	
	14:56	070	"	I	off	5	10000	400	400	n	scattered cloud
	15:03	071	"	I	off	5	10000	400	400	n	
	15:11	072	"	I	off	5	10000	400	400	n	
	15:18	073	"	I	off	5	10000	400	400	n	Cloud worsening
	15:27	074	"	I	off	5	10000	400	400	n	
	15:35	075	"	I	off	5	10000	400	400	n	
	15:40	076	"	I	off	5	10000	400	400	n	
	15:47	077	"	I	off	5	10000	400	400	n	
	15:54	078	"	I	off	5	10000	400	400	n	
23/3/05	16:01	079	"	I	off	5	10000	400	400	n	
	16:09	080	"	I	off	5	10000	400	400	n	
	16:15	081	"	I	off	5	10000	400	400	n	
	16:22	082	"	I	off	5	10000	400	400	n	
	16:29	083	"	I	off	5	10000	400	400	n	
	16:35	084	"	I	off	5	10000	400	400	n	
	16:42	085	"	I	off	5	10000	400	400	n	
	12:30	032	75cm	I	off	6	3000	768	576	y	
	12:34	033	"	R	off	4	3000	768	576	y	slight cloud
	12:42	034	"	V	off	6	3000	768	576	y	"
	12:46	035	"	B	off	6	3000	768	576	y	
	12:50	036	"	B	off	6	1000	768	576	y	
	12:53	037	"	V	off	4	1000	768	576	y	
25/6/05	12:57	038	"	R	off	4	1000	768	576	y	
	13:02	039	"	I	off	6	1000	768	576	y	
						AAT, camera 2					
		034	1m	R	1/250	8	3000	768	576	n	bottom edge
		035	"	R	1/250	8	3000	768	576	n	top edge
	8:44	036	"	R	1/120	6	3000	768	576	n	top edge
		037	"	R	1/120	6	3000	768	576	n	bottom edge

Date	UT	Run no.	Aperture	Filter	Exposure	Gain	Total Frames	Frame Size X pixels Y pixels		Power- mate	Notes
"		038	"	R	1/120	6	3000	768	576	n	trailed up & down
"		039	"	R	1/120	6	3000	768	576	n	trailed
"		040	0.6m	R	1/120	8	3000	768	576	n	bottom edge
"		041	"	R	1/120	8	3000	768	576	n	top edge
"		042	"	R	1/120	8	3000	768	576	n	trailed
"		043	"	R	off	6	3000	768	576	n	trailed
"		044	"	R	off	6	3000	768	576	n	top edge
"	9:24	045	"	R	off	6	3000	768	576	n	bottom edge
"		046	0.8m	R	off	5	3000	768	576	n	bottom edge
"	9:41	047	"	R	off	5	3000	768	576	n	top edge
"		048	"	R	off	5	3000	768	576	n	trailed
"	9:56	049	"	R	1/120	7	3000	768	576	n	trailed
"		050	"	R	1/120	7	3000	768	576	n	top edge
"		051	"	R	1/120	7	3000	768	576	n	top edge
"		052	"	R	1/120	7	3000	768	576	n	bottom edge
"		053	3.9m	R	1/120	0	3000	768	576	n	top edge
"		054	"	R	1/120	0	3000	768	576	n	bottom edge
"		055	"	R	1/120	0	3000	768	576	n	trailed
"		056	2.5m	R	1/120	4	3000	768	576	n	trailed
"		057	"	R	1/120	4	3000	768	576	n	bottom edge
"		058	"	R	1/120	4	3000	768	576	n	top edge
EUROPA & GANYMEDE											
AAT, camera 2											
25/6/05		059	3.9m1m	R	1/120	4	10000	300	200	n	
"		060	0.8m	R	off	9	10000	300	200	n	
"		061	"	R	off	9	10000	300	200	n	
SATURN											
Macquarie 40cm, camera 1											
8/3/05		001	40cm	G	1/250	6	5000	600	500	n	
"		002	"	G	off	6	1000	500	400	n	
ANU 1m, camera 1											
14/3/05	9:20	002	75cm	I	1/250	8	5000	400	300	n	
"	"	003	"	R	1/250	8	5000	400	300	n	Cloud
"	"	004	"	R	1/250	8	5000	400	300	n	
"	9:37	005	"	V	1/250	8	5000	400	300	n	
"	9:41	006	"	B	1/250	11	5000	400	300	n	
"	9:47	007	"	B	1/250	11	5000	400	300	n	
15/3/05	10:05	006	100cm	I	off	8	5000	400	400	n	Cloud
20/3/05	9:14	017	30cm	I	off	6	5000	400	400	n	
"	9:20	018	"	R	off	5	5000	400	400	n	
"	9:28	019	"	V	off	6	5000	400	400	n	V. bad seeing

Date	UT	Run no.	Aperture	Filter	Exposure	Gain	Total Frames	Frame Size		Power- mate	Notes
								X pixels	Y pixels		
"	9:36	020	"	V	off	6	5000	400	400	n	
"	9:45	021	"	B	off	12	5000	400	400	n	V bad seeing & noise.
21/3/05	8:47	001	30cm	I	off	7	5000	400	400	n	
"	8:50	002	"	R	off	5	5000	400	400	n	slight cloud
"	8:54	003	"	V	off	6	5000	400	400	n	
"	9:00	004	"	B	off	10	5000	400	400	n	
22/3/05	8:45	015	30cm	I	off	7	5000	400	400	n	
"	8:49	016	"	R	off	5	5000	400	400	n	
"	8:54	017	"	V	off	7	5000	400	400	n	Cloud increasing, stop runs.
"	9:58	018	"	B	off	10	5000	400	400	n	Clear sky, resume. Wavy.
23/3/05	9:48	005	30cm	I	off	7	5000	400	400	n	Clear & stable
"	9:52	006	"	R	off	5	5000	400	400	n	
"	9:57	007	"	V	off	6	5000	400	400	n	
"	10:01	008	"	B	off	8	5000	400	400	n	
"	10:18	009	75cm	R	1/120	7	3000	768	576	y	
"	10:25	010	"	V	1/120	8	3000	768	576	y	
"	10:29	011	"	B	off	11	3000	768	576	y	
"	10:32	012	"	I	off	10	3000	768	576	y	
ANU 1m, camera 2											
9/11/05	17:52	102	30cm	I	off	7	5000	400	300	n	Very bad moments
"	17:57	103	"	R	off	6	5000	400	300	n	
"	18:02	104	"	V	off	6	5000	400	300	n	
"	18:08	105	"	B	off	12	5000	400	300	n	Xtremely bad moments
11/11/05	17:47	098	30cm	R	off	6	5000	400	300	n	
"	17:51	099	"	V	off	6	5000	400	300	n	
"	17:55	100	"	B	off	12	5000	400	300	n	
"	18:00	101	"	I	off	7	5000	400	300	n	
"	18:04	102	"	I	off	7	5000	400	300	n	
"	18:09	103	"	R	off	6	5000	400	300	n	
"	18:13	104	"	V	off	6	5000	400	300	n	
"	18:17	105	"	B	off	12	5000	400	300	n	
12/11/05	17:52	080	75cm	V	off	7	5000	600	300	y	
"	17:57	081	"	R	off	6	5000	600	300	y	
"	18:01	082	"	I	off	8	5000	600	300	y	
"	18:06	083	"	B	off	14	5000	600	300	y	
"	18:10	084	"	B	off	14	5000	600	300	y	
"	18:14	085	"	V	off	7	5000	600	300	y	
"	18:18	086	"	R	off	6	5000	600	300	y	
"	18:22	087	"	I	off	8	5000	600	300	y	

URANUS

ANU 1m, camera 2

9/11/05	12:52	056	30cm	V	off	14	5000	200	200	n
---------	-------	-----	------	---	-----	----	------	-----	-----	---

Date	UT	Run no.	Aperture	Filter	Exposure	Gain	Total Frames	Frame Size		Power- mate	Notes
								X pixels	Y pixels		
11/11/05	12:57	057	”	R	off	14	5000	200	200	n	
	10:40	038	”	R	off	14	5000	200	200	n	
	10:42	039	”	V	off	14	5000	200	200	n	

References

- ANISIMOV, V. F., BERDINA, R. N., NECHAEVA, N. N., NIKOLAEV, P. V. AND ROZHNOVA, I. P. (1970) *The Probability of Obtaining Good Star Images with Short-Exposure Photography*, N. B. Divari, ed., *Proceedings of Conferences on atmospheric optics, held in Pulkovo, November/December, 1965 and December, 1966, New York: Consultants Bureau, 1970, edited by Nikolai B. Divari., p.31*, pp. 31–37.
- AVILA, R., VERNIN, J. AND SÁNCHEZ, L. J. (2001) *Atmospheric turbulence and wind profiles monitoring with generalized scidar*, *Astron. Astrophys.* **369** pp. 364–372.
- AYERS, G. R. AND DAINTY, J. C. (1988) *Iterative blind deconvolution method and its applications*, *Optics Letters* **13** pp. 547–549.
- BABCOCK, H. W. (1953) *The Possibility of Compensating Astronomical Seeing*, *Publ. Astron. Soc. Pac.* **65** pp. 229–236.
- BAILEY, J. AND CHAMBERLAIN, S., *Image Gallery - ACA Planetary Astronomy*, www.phys.unsw.edu.au/~jbailey/planets/images.html.
- BALDWIN, J. E., TUBBS, G. C., R. N. COX, MACKAY, C. D., WILSON, R. W. AND ANDERSEN, M. I. (2001) *Diffraction-limited 800nm imaging with the 2.56m Nordic Optical Telescope*, *Astron. Astrophys.* **368** pp. L1–L4.
- BALDWIN, J. E., WARNER, P. J. AND MACKAY, C. D. (2008) *The point spread function in Lucky Imaging and variations in seeing on short timescales*, *Astron. Astrophys.* **480** pp. 589–597.

- BAUMGARDNER, J., MENDILLO, M. AND WILSON, J. K. (2000) *A Digital High-Definition Imaging System for Spectral Studies of Extended Planetary Atmospheres. I. Initial Results in White Light Showing Features on the Hemisphere of Mercury Unimaged by Mariner 10*, *Astron. J.* **119** pp. 2458–2464.
- BECKERS, J. M. AND RIMMELE, T. R. (1996) *Limitations Placed on the Time Coverage, Isoplanatic Patch Size and Exposure Time for Solar Observations Using Image Selection Procedures in the Presence of Telescope Aberrations*, *Bulletin of the American Astronomical Society*, vol. 28, pp. 1325–+.
- BERREVOETS, C. (2008) *RegiStax - Free Image Processing Software*, website <http://www.astronomie.be/registax/>.
- BORRA, E. F., SEDDIKI, O., ANGEL, R., EISENSTEIN, D., HICKSON, P., SEDDON, K. R. AND WORDEN, S. P. (2007) *Deposition of metal films on an ionic liquid as a basis for a lunar telescope*, *Nature* **447** pp. 979–981.
- BUSCHER, D. (1988) *Optimizing a ground-based optical interferometer for sensitivity at low light levels*, *Mon. Not. R. Astron. Soc.* **235** pp. 1203–1226.
- BUSCHER, D. F. (1994) *A thousand and one nights of seeing on Mt Wilson.*, J. B. Breckinridge, ed., *2. Conference on Amplitude and Intensity Spatial Interferometry.*, pp. 260–271.
- CADY, F. M. AND BATES, R. H. T. (1980) *Speckle processing gives diffraction-limited true images from severely aberrated instruments.*, *Optics Letters* **5** pp. 438–440.
- CARHART, G. W. AND VORONTSOV, M. A. (1998) *Synthetic imaging: nonadaptive anisoplanatic image correction in atmospheric turbulence*, *Optics Letters* **23** pp. 745–747.
- CECIL, G. AND RASHKEEV, D. (2007) *A Side of Mercury Not Seen by Mariner 10*, *Astron. J.* **134** pp. 1468–1474.

- CLARE, R. M., VAN DAM, M. A. AND BOUCHEZ, A. H. (2007) *Modeling low order aberrations in laser guide star adaptive optics systems*, Optics Express **15** pp. 4711–4725.
- CORRSIN, S. (1951) *On the Spectrum of Isotropic Temperature Fluctuations in an Isotropic Turbulence*, Journal of Applied Physics **22** pp. 469–473.
- DANTOWITZ, R. (1998) *Sharper Images Through Video*, Sky & Telescope **aug** pp. 48–54.
- DANTOWITZ, R. F., TEARE, S. F. AND KOZUBAL, M. J. (2000) *Ground-Based High-Resolution Imaging of Mercury*, Astron. J. **119** pp. 2455–2457.
- DAVIES, R., RABIEN, S., LIDMAN, C., LE LOUARN, M., KASPER, M., FÖRSTER SCHREIBER, N. M., ROCCATAGLIATA, V., AGEORGES, N., AMICO, P., DUMAS, C. AND MANNUCCI, F. (2008) *Laser Guide Star Adaptive Optics without Tip-tilt*, The Messenger **131** pp. 7–10, 0801.3738.
- DAVIS, J. AND NORTH, J. R. (2001) *Binary Star Observations in Selected Instants of Good Seeing*, Publications of the Astronomical Society of Australia **18** pp. 281–286.
- DAVIS, J. AND TANGO, W. (1996) *Measurement of the Atmospheric Coherence Time*, Publ. Astron. Soc. Pac. **108** pp. 456–458.
- DENKER, C., MASCARINAS, D., XU, Y., CAO, W., YANG, G., WANG, H., GOODE, P. R. AND RIMMELE, T. (2005) *High-Spatial-Resolution Imaging Combining High-Order Adaptive Optics, Frame Selection, and Speckle Masking Reconstruction*, Solar Physics **227** pp. 217–230.
- DEVILLARD, N. (2001) *ESO C Library for an Image Processing Software Environment (eclipse)*, F. R. Harnden, Jr., F. A. Primini and H. E. Payne, eds., *Astronomical Data Analysis Software and Systems X*, Astronomical Society of the Pacific Conference Series, vol. 238, Astronomical Society of the Pacific Conference Series, vol. 238, pp. 525–528.

- DEWITT, J. H., HARDIE, R. H. AND SEYFERT, C. K. (1957) *A seeing compensator employing television techniques.*, Astron. J. **62** pp. 139–140.
- FISHBAIN, B., YAROSLAVSKY, L. P. AND IDESES, I. A. (2007) *Real Time Turbulent Video Perfecting by Image Stabilization and Super-Resolution*, ArXiv e-prints **704**, 0704.3447.
- FRIED, D. L. (1965) *Statistics of a Geometric Representation of Wavefront Distortion*, Journal of the Optical Society of America (1917-1983) **56** pp. 1427–1435.
- FRIED, D. L. (1966) *Optical Resolution Through a Randomly Inhomogeneous Medium for Very Long and Very Short Exposures*, Journal of the Optical Society of America (1917-1983) **56** pp. 1372–1379.
- FRIED, D. L. (1978) *Probability of getting a lucky short-exposure image through turbulence*, Optical Society of America Journal A **68** pp. 1651–1658.
- FRIED, D. L. AND MEVERS, G. E. (1974) *Evaluation of r_0 for Propagation Down Through the Atmosphere*, App. Opt. **13** pp. 2620–2622.
- FRIGO, M. AND JOHNSON, S. G. (2005) *The Design and Implementation of FFTW3*, Proceedings of the IEEE **93**(2) pp. 216–231, special issue on “Program Generation, Optimization, and Platform Adaptation”.
- GHEZ, A. M., HORNSTEIN, S. D., LU, J. R., BOUCHEZ, A., LE MIGNANT, D., VAN DAM, M. A., WIZINOWICH, P., MATTHEWS, K., MORRIS, M., BECKLIN, E. E., CAMPBELL, R. D., CHIN, J. C. Y., HARTMAN, S. K., JOHANSSON, E. M., LAFON, R. E., STOMSKI, P. J. AND SUMMERS, D. M. (2005) *The First Laser Guide Star Adaptive Optics Observations of the Galactic Center: Sgr A*’s Infrared Color and the Extended Red Emission in its Vicinity*, Astrophys. J. **635** pp. 1087–1094.
- GIORGINI, J. D., YEOMANS, D. K., CHAMBERLIN, A. B., CHODAS, P. W., JACOBSON, R. A., KEESEY, M. S., LIESKE, J. H., OSTRO, S. J., STANDISH, E. M.

- AND WIMBERLY, R. N. (1996) *JPL's On-Line Solar System Data Service*, *Bulletin of the American Astronomical Society*, *Bulletin of the American Astronomical Society*, vol. 28, *Bulletin of the American Astronomical Society*, vol. 28, pp. 1158–+.
- GLICK, Y., BARAM, A., LOEBENSTEIN, H. M. AND AZAR, Z. (1991) *Restoration of turbulence-degraded images by the most-common method.*, *App. Opt.* **30** pp. 3924–3929.
- GRAHAM, J. R., *Strehl Ratio & the Marechal Criterion*
, <http://etoile.berkeley.edu/~jrg/SEEING/node5.html>.
- GREEN, J. J. AND HUNT, B. R. (1999) *Improved restoration of space object imagery*, *Journal of the Optical Society of America A* **16** pp. 2859–2865.
- GREENWOOD, D. P. (1977) *Bandwidth specification for adaptive optics systems.*, *Journal of the Optical Society of America* (1917-1983) **67** pp. 390–393.
- HERLIN, T., BRIGHTON, A. AND BIEREICHEL, P. (1996) *The VLT Real Time Display*, G. H. Jacoby and J. Barnes, eds., *Astronomical Data Analysis Software and Systems V*, *Astronomical Society of the Pacific Conference Series*, vol. 101, *Astronomical Society of the Pacific Conference Series*, vol. 101, pp. 396–+.
- ISHIMARU, A. (1978) *Wave Propagation and Scattering in Random Media, volume 2*, Academic Press, New York.
- JEFFERIES, S. M. AND CHRISTOU, J. C. (1993) *Restoration of Astronomical Images by Iterative Blind Deconvolution*, *Astrophys. J.* **415** pp. 862–874.
- KERN, B., LAURENCE, T. A., MARTIN, C. AND DIMOTAKIS, P. E. (2000) *Temporal coherence of individual turbulent patterns in atmospheric seeing*, *App. Opt.* **39** pp. 4879–4885.
- KOLMOGOROV, A. N. (1941a) *Local structure of turbulence in an incompressible viscous fluid at very high Reynolds numbers*, *Doklady Academy Nauk. SSSR* **30(4)** pp. 299–301.

- KOLMOGOROV, A. N. (1941b) *On the degeneration of isotropic turbulence in an incompressible viscous fluid*, Doklady Academy Nauk. SSSR **31**(6) pp. 538–541.
- KSANFOMALITY, L. V. (2003) *Mercury: The Image of the Planet in the 210°-285° W Longitude Range Obtained by the Short-Exposure Method*, Solar System Research **37** pp. 469–479.
- LABEYRIE, A. (1970) *Attainment of Diffraction Limited Resolution in Large Telescopes by Fourier Analysing Speckle Patterns in Star Images*, Astron. Astrophys. **6** pp. 85–87.
- LANE, R. G. (1992) *Blind deconvolution of speckle images.*, Journal of the Optical Society of America (1917-1983) **9** pp. 1508–1514.
- LAW, N. M., HODGKIN, S. T., MACKAY, C. D. AND BALDWIN, J. E. (2005) *Ten new very low-mass close binaries resolved in the visible*, Astronomische Nachrichten **326** pp. 1024–1025, arXiv:astro-ph/0512191.
- LAW, N. M., MACKAY, C. D., IRELAND, M., MOORE, A. AND DEKANY, R. G. (2007) *Getting Lucky With Adaptive Optics: Diffraction-limited-resolution In The Visible On a 5m-class Telescope*, American Astronomical Society Meeting Abstracts, American Astronomical Society Meeting Abstracts, vol. 211, American Astronomical Society Meeting Abstracts, vol. 211, p. 83.
- LEIGHTON, R. B. (1956) *Concerning the Problem of Making Sharper Photographs of the Planets*, Scientific American **194** p. 157.
- LELIEVRE, G., NIETO, J.-L., THOUVENOT, E., SALMON, D. AND LLEBARIA, A. (1988) *Very high resolution imaging using sub-pupil apertures, recentering and selection of short exposures*, Astron. Astrophys. **200** pp. 301–311.
- LYNDS, C. R., WORDEN, S. P. AND HARVEY, J. W. (1976) *Digital image reconstruction applied to alpha Orionis*, Astrophys. J. **207** pp. 174–180.

- MACKAY, C. D. (2005) *Near Diffraction-Limited Visible Imaging on 10-30 m Class Telescopes with EMCCDs*, Ringberg, ed., *Proceedings of Conference on Instrumentation for ELTs*.
- MACKAY, C. D. (2006) *Near Diffraction Limited Visible Imaging on 10 m class Telescopes with EMCCDs*, J. E. Beletic, J. W. Beletic and P. Amico, eds., *Scientific Detectors for Astronomy 2005*, p. 93.
- MACKAY, C. D., *Lucky Imaging Results*, website
http://www.ast.cam.ac.uk/~optics/Lucky_Web_Site/LI_Results.htm.
- MASCIADRI, E. AND GARFIAS, T. (2001) *Wavefront coherence time seasonal variability and forecasting at the San Pedro Mártir site*, *Astron. Astrophys.* **366** pp. 708–716.
- MASON, B. D., WYCOFF, G. L., HARTKOPF, W. I., DOUGLASS, G. G. AND WORLEY, C. E. (2001) *The 2001 US Naval Observatory Double Star CD-ROM. I. The Washington Double Star Catalog*, *Astron. J.* **122** pp. 3466–3471.
- MEINEL, A. B. (1963) *Final Report on the Site Selection Survey for the National Astronomical Observatory, Contributions from the Kitt Peak National Observatory*, Kitt Peak National Observatory, Tuscon, Ariz, 45, p. 118.
- MENDILLO, M., WARELL, J., LIMAYE, S. S., BAUMGARDNER, J., SPRAGUE, A. AND WILSON, J. K. (2001) *Imaging the surface of Mercury using ground-based telescopes*, *Planetary & Space Sci.* **49** pp. 1501–1505.
- MICHELSON, A. A. AND PEASE, F. G. (1921) *No. 203. Measurement of the diameter of alpha Orionis with the interferometer.*, *Contributions from the Mount Wilson Observatory / Carnegie Institution of Washington* **203** pp. 1–11.
- MOHAAMMED, A. T. AND BURGE, R. E. (1988) *Short-exposure turbulent image reconstructions.*, *Journal of Physics D Applied Physics* **21** pp. 1067–1077.

- MULLER, R. A. AND BUFFINGTON, A. (1974) *Real-time correction of atmospherically degraded telescope images through image sharpening*, Journal of the Optical Society of America (1917-1983) **64** pp. 1200–1210.
- PENCE, W. (1999) *CFITSIO, v2.0: A New Full-Featured Data Interface*, D. M. Mehringer, R. L. Plante, & D. A. Roberts, ed., *Astronomical Data Analysis Software and Systems VIII, Astronomical Society of the Pacific Conference Series*, vol. 172, *Astronomical Society of the Pacific Conference Series*, vol. 172, pp. 487–+.
- PERRYMAN, M. A. C., LINDEGREN, L., KOVALEVSKY, J., HOEG, E., BASTIAN, U., BERNACCA, P. L., CRÉZÉ, M., DONATI, F., GRENON, M., VAN LEEUWEN, F., VAN DER MAREL, H., MIGNARD, F., MURRAY, C. A., LE POOLE, R. S., SCHRIJVER, H., TURON, C., ARENOU, F., FROESCHLÉ, M. AND PETERSEN, C. S. (1997) *The HIPPARCOS Catalogue*, Astron. Astrophys. **323** pp. L49–L52.
- PETERS, M. A., CLOSE, L. M., RADEMACHER, M., STALCUP, T., SWARTZLANDER, G. A., FORD, E. AND ABDUL-MALIK, R. S. (2008) *A high-Strehl low-resolution optical imager (BESSEL): Detection of a $0.7\lambda/D$ separation binary from the ground*, New Astronomy **13** pp. 359–369.
- PIQUE, J., MOLDOVAN, I. C. AND FESQUET, V. (2006) *Concept for polychromatic laser guide stars: one-photon excitation of the $4P_{3/2}$ level of a sodium atom*, Journal of the Optical Society of America A **23** pp. 2817–2828.
- PLATT, J. R. (1957) *Increase of Telescope Resolution with Time-Selection with an Image-Forming Stellar Interferometer.*, Astrophys. J. **125** pp. 601–610.
- RICHARDSON, L. F. (1920) *The Supply of Energy from and to Atmospheric Eddies*, Royal Society of London Proceedings Series A **97** pp. 354–373.
- ROBERTS, L. C. J., PERRIN, M. D., MARCHIS, F., SIVARAMAKRISHNAN, A., MAKIDON, R. B., CHRISTOU, J. C., MACINTOSH, B. A., POYNER, L. A., VAN DAM, M. A. AND TROY, M. (2004) *Is That Really your Strehl Ratio?*, *Advancements in Optics*, vol. 5490, vol. 5490, pp. 504–515.

- RODDIER, F., GILLI, J. M. AND VERNIN, J. (1982) *On the isoplanatic patch size in stellar speckle interferometry.*, Journal d'Optique **13** pp. 63–70.
- ROGGEMANN, M. C., STOUT, C. A. AND WELSH, B. M. (1994) *Image-spectrum signal-to-noise-ratio improvements by statistical frame selection for adaptive-optics imaging through atmospheric turbulence*, Optical Engineering **33** pp. 3254–3264.
- ROGGEMANN, M. C. AND WELSH, B. M. (1996) *Imaging Through Turbulence*, CRC Press.
- SHORTTRIDGE, K., FARRELL, T. J., BAILEY, J. A. AND WALLER, L. G. (2004) *The data flow system for the AAO2 controllers*, H. Lewis and G. Raffi, eds., *Society of Photo-Optical Instrumentation Engineers (SPIE) Conference Series*, Society of Photo-Optical Instrumentation Engineers (SPIE) Conference Series, vol. 5496, Society of Photo-Optical Instrumentation Engineers (SPIE) Conference Series, vol. 5496, pp. 463–468.
- SMITH, A., BAILEY, J., HOUGH, J. H. AND LEE, S. (2009) *An investigation of lucky imaging techniques*, Mon. Not. R. Astron. Soc. **398** pp. 2069–2073.
- SMITH, R. C. (1995) *Observational Astrophysics*, Cambridge University Press.
- STREHL, K. (1895) *Aplanatische und fehlerhafte Abbildung im Fernrohr*, Zeitschrift für Instrumentenkunde **15** pp. 362–370.
- STREHL, K. (1902) *ber Luftschlieren und Zonenfehler*, Zeitschrift für Instrumentenkunde **22** pp. 213–217.
- TATARSKI, V. I. (1961) *Wave Propagation in a Turbulent Medium*, Dover Publications Inc., New York.
- TIKHOMIROV, V. M., ed. (1985) *Selected Works of A. N. Kolmogorov, Volume 1: Mathematics and Mechanics.*, Kluwer Academic Publishers.
- TOKOVININ, A. AND KORNILOV, V. (2007) *Accurate seeing measurements with MASS and DIMM*, Mon. Not. R. Astron. Soc. **381** pp. 1179–1189.

- TUBBS, R. N. (2004) *Lucky exposures: diffraction-limited astronomical imaging through the atmosphere*, The Observatory **124** pp. 159–160.
- TURNER, J., MCGRAW, J., ZIMMER, P., WILLIAMS, T., CLAVER, C., KRABBENDAM, V., WIECHA, O., ANDREW, J. AND WARNER, M. (2010) *A Microthermal Device for Measuring the Spatial Power Spectrum of Atmospheric Optical Turbulence*, *Bulletin of the American Astronomical Society*, *Bulletin of the American Astronomical Society*, vol. 41, *Bulletin of the American Astronomical Society*, vol. 41, pp. 402–+.
- TYSON, R. K. (1998) *Principles of Adaptive Optics*, Academic Press, 2 edn.
- VERNIN, J. AND MUNOZ-TUNON, C. (1995) *Measuring astronomical seeing: The DA/IAC DIMM*, *Publ. Astron. Soc. Pac.* **107** pp. 265–272.
- VON DER LÜHE, O. (1984) *Estimating Fried’s parameter from a time series of an arbitrary resolved object imaged through atmospheric turbulence*, *Journal of the Optical Society of America A* **1** pp. 510–519.
- VORONTSOV, M. A. AND CARHART, G. W. (2001) *Anisoplanatic imaging through turbulent media: image recovery by local information fusion from a set of short-exposure images*, *Journal of the Optical Society of America A* **18** pp. 1312–1324.
- WARELL, J. AND LIMAYE, S. S. (2001) *Properties of the Hermean regolith: I. Global regolith albedo variation at 200km scale from multicolor CCD imaging*, *Planetary & Space Sci.* **49** pp. 1531–1552.
- WILSON, J., BAUMGARDNER, J. AND MENDILLO, M. (2004) *Methods for Imaging Mercury’s Sodium Exosphere.*, *35th COSPAR Scientific Assembly*, vol. 35, vol. 35, p. 2393.
- WILSON, J., BAUMGARDNER, J. AND MENDILLO, M. (2006) *High Resolution Imaging of Sodium at Mercury*, *Bulletin of the American Astronomical Society*, vol. 38, vol. 38, p. 588.

YOUNG, A. T. (1974) *Seeing: its Cause and Cure*, Astrophys. J. **189** pp. 587–604.